

DIRECTIONAL NANOEPITAXY OF NANOWIRE  
ASYMMETRIC SHELL HETEROSTRUCTURES  
AND IMPLICATION FOR SENSORS

DIRECTIONAL NANOEPITAXY OF NANOWIRE  
ASYMMETRIC SHELL HETEROSTRUCTURES AND  
IMPLICATION FOR SENSORS

BY

SPENCER McDERMOTT, B.Eng.

A Thesis

Submitted to McMaster University's

Department of Engineering Physics

and School of Graduate Studies

in Partial Fulfilment of the Requirements for the Degree of

Doctor of Philosophy

© Copyright by Spencer McDermott, October 21, 2024  
All Rights Reserved

Doctor of Philosophy (2024)

McMaster University

(Engineering Physics)

Hamilton, Ontario

TITLE: Directional Nanoepitaxy of Nanowire Asymmetric Shell  
Heterostructures and Implication for Sensors

AUTHOR: Spencer McDermott B.Eng. (McMaster University)

SUPERVISOR: Ryan B. Lewis

NUMBER OF PAGES: XXV, 174

# Abstract

Nanoscale wires, nanowires, have shown great promise for the next generation of ultra-sensitive sensors. This thesis presents a path for using directional nanoepitaxy to enable the mass-production of nanowire sensor devices. Core-shell nanowires with asymmetric shells, created using directional nanoepitaxy, exploit lattice mismatch between the core and asymmetric shell to generate strain gradients, resulting in nanowire bending. This research investigates the mechanisms behind this bending process, specifically examining the directional nanoepitaxy of GaAs-InP and GaAs-(Al,In)As core-shell nanowires by molecular beam epitaxy. Through X-ray diffraction and electron microscopy, variations in curvature and strain along these nanowires, linked to local differences in shell thickness, have been observed. Modeling using linear elastic theory indicates that these variations are due to differences in the flux contact angle along the nanowire as it bends.

Nanowire growth conditions are found to lead to variations in the shell distribution around a nanowire's cross-section. Controlling temperature during the directional growth of III-V nanowires, we influence the diffusivity of group III adatoms, resulting in two possible growth modes: In diffusion-limited growth and group V-controlled growth. We employ phosphorus-controlled nanoepitaxy to grow asymmetric InP shells on GaAs cores, examining the shell distribution and twisting of the nanowires. Transmission electron microscopy analysis of the nanowire cross-sections reveals that the shell distribution is relative to the phosphorus flux. Using analytical electron tomography

reconstruction techniques to determine the core-shell geometry along a nanowire, we find that twisting occurs to minimize strains energy when the bending direction is not aligned with the  $\langle 1\bar{1}0 \rangle$  or  $\langle 11\bar{2} \rangle$  crystallographic directions.

By synthesizing connected nanowire pairs and forming nanowire arches, we demonstrate their potential for a template to fabricate sensor-based transistor devices. The research highlights the potential of bent nanowire heterostructures for next-generation nanotechnology applications, particularly in creating innovative device geometries for bottom-up fabrication.

# Acknowledgements

*“In that instant they felt an overwhelming sense of pride and accomplishment. Though they had failed dismally even to come close to the expedition's original objective, they knew now that somehow they had done much, much more than ever they set out to do.”*

—Lansing, A. (2007). *Endurance: Shackleton's incredible voyage*. I don't think I would have read the book without you mentioning it. However, I'm glad I have as endurance is something needed in our lives as not all things worth doing are easy and many things are possible. My deepest thanks to Ryan B. Lewis for being my mentor, providing me with the necessary opportunities and lessons to complete my studies. I am also grateful to my committee members, Ray R. LaPierre and Andrew Knights, for their invaluable support throughout my PhD and for encouraging me towards excellence. A special thank you to Trevor R. Smith for being a companion and sparking many piquant outlooks, debates, and conversations, as well as for your teamwork in assisting with my research. The Epitaxial Nanostructures and Materials Group has been incredibly welcoming, providing friendly faces, great humor, and better atmosphere.

I would like to thank my loving Family for supporting me throughout my studies. for providing me with a place to rent, help when needed, and great advice for my whole life. My partner, Ale whose support and love can bring out the best in me. My cats, Spanky and Mouse, for only pushing the minimal items off my desk while I was writing my thesis. Lastly, I would like to thank the Big Pauls Fan Club trivia team for giving me

many a discounted meal. I hope to return and see us secure victory for the year—as it seems assured at this point!



## List of Publications

- (1) Davtyan, A.; Kriegner, D.; Holý, V.; AlHassan, A.; Lewis, R. B.; **McDermott, S.**; Geelhaar, L.; Bahrami, D.; Anjum, T.; Ren, Z.; Richter, C.; Novikov, D.; Müller, J.; Butz, B.; Pietsch, U. **X-Ray Diffraction Reveals the Amount of Strain and Homogeneity of Extremely Bent Single Nanowires.** *J Appl Crystallography* 2020, 53 (111), 1310–1320. <https://doi.org/10.1107/S1600576720011516>.

\* I developed the analytical bending model for this paper to demonstrate that variations in shell thickness along the nanowire are correlated with bending variations. Additionally, I wrote an initial draft of the section discussing this model. Growths performed with MBE at Paul Drude Institute.

- (2) **McDermott, S.**; Lewis, R. B. **Bending of GaAs–InP Core–Shell Nanowires by Asymmetric Shell Deposition: Implications for Sensors.** *ACS Appl Nano Mater* 2021. <https://doi.org/10.1021/acsanm.1c01636>.

\* I modeled the impact of core diameter and lattice mismatch on bending. My evolution modeling showed how shell thickness distribution changes over time along a nanowire and the impact of self-shadowing and pair shadowing on bending. This model aligned well with GaAs–Al<sub>0.5</sub>In<sub>0.5</sub>As core–shell nanowires. The majority of the writing in this publication was my undertaking as first author. Growths performed with MBE at McMaster by Shahram Ghanad-Tavakoli.

- (3) **McDermott, S.;** Smith, T. R.; LaPierre, R. R.; Lewis, R. B. **Phosphorus-Controlled Nanoepitaxy of Asymmetric GaAs-InP Core-Shell Bent Nanowires: Implications for Bottom-Up Nanowire Transistors and Sensors.** *ACS Appl Nano Mater* 2024, 7 (1), 1257–1264.

<https://doi.org/10.1021/acsanm.3c05235>.

- \* I conducted an analysis of TEM data collected by Trevor R. Smith and Carmen Andrei, focusing on microtome cross-sections of asymmetric GaAs–InP core–shell nanowires and pairs of such nanowires. Through this analysis, I identified two growth modes: diffusion-limited and phosphorus-controlled. In the phosphorus-controlled mode, I provided a mathematical model showing that the InP shell is distributed linearly in proportion to the phosphorus received on the side facets. The shadowing analysis revealed that the scattered/re-emitted phosphorus flux from the substrate is isotropic, and effective pair shadowing of nanowires can occur when separations are sufficiently small, based on beam divergence. Nanowire pairs connected by shadowing were also examined and analyzed by me. The majority of the writing in this publication was my undertaking as first author. Growths performed with MBE at McMaster by Shahram Ghanad-Tavakoli.

- (4) Trevor R. Smith, Spencer McDermott, Vatsalkumar Patel, Ross Anthony, Manu Hedge, Sophie E. Bierer, Sunzhuoran Wang, Andrew P. Knights, Ryan B. Lewis  
*Ultra-Thin Strain-Relieving  $Si_{1-x}Ge_x$  Layers Enabling III-V Epitaxy on Si.*  
*Adv. Mater. Interfaces* 2024, 2196-7350

<https://onlinelibrary.wiley.com/doi/10.1002/admi.202400580>

- \* I wrote and edited sections of the paper, created figures, and conducted the HR-XRD measurements. Growths performed with MOCVD at McMaster by Manu Hedge.
- (5) **McDermott, S.; Smith, T. R.; Lewis, R. B. Exploring Crystallographic Orientation's Impact on Nanowire Bending and Twisting with Practical Analytical Electron Tomography. *Publication pending***
- \* I was responsible for the writing, figures, and analysis. All SEM images were captured by me, while Trevor R. Smith took the TEM images. I demonstrated twisting in nanowires and used modeling to show that it happens due to a reduction in strain energy. Using TEM data, I developed a reconstruction method to image the nanowire cross-section along its length. Growths performed with MBE at McMaster by me.

# Table of Contents

<b>Abstract.....</b>	<b>iii</b>
<b>Acknowledgements .....</b>	<b>v</b>
<b>List of Publications .....</b>	<b>viii</b>
<b>List of Figures.....</b>	<b>xiv</b>
<b>Abbreviations .....</b>	<b>xxiii</b>
<b>Symbols .....</b>	<b>xxv</b>
<b>Chapter 1 Introduction.....</b>	<b>1</b>
1.1 Background and Motivation .....	1
1.2 Overview of Thesis .....	4
<b>Chapter 2 Micro- and Nano-focused X-ray Diffraction Analysis of Bent GaAs–</b>	
<b>Al<sub>x</sub>Ga<sub>x-1</sub>As Core–shell Nanowires.....</b>	<b>14</b>
2.1 Published: X-ray diffraction reveals the amount of strain and homogeneity of extremely bent single nanowires.....	14
2.2 Introduction.....	15
2.3 Experimental .....	18
2.4 Micro-focus X-ray diffraction data.....	25
2.5 Transmission electron microscopy .....	32
2.6 Diffraction theory of bent NWs .....	35

2.7	Results and discussion .....	44
2.8	Conclusion .....	51
<b>Chapter 3 Analytical Modeling of Nanowire Directional Growth of Asymmetric Shells and Bending.....</b>		<b>59</b>
3.1	Published: Bending of GaAs–InP Core–Shell Nanowires by Asymmetric Shell Deposition: Implications for Sensors.....	59
3.2	Introduction.....	59
3.3	Methods.....	62
3.4	Results and Discussion .....	69
<b>Chapter 4 Indium-diffusion-limited and Phosphorus-Controlled Nanoepitaxy of InP Shell on GaAs Nanowires .....</b>		<b>90</b>
4.1	Published: Phosphorus-Controlled Nanoepitaxy of Asymmetric GaAs–InP Core–Shell Bent Nanowires: Implications for Bottom-Up Nanowire Transistors and Sensors Declaration .....	90
4.2	Introduction.....	91
4.3	Methods.....	94
4.4	Results and Discussion .....	96
4.5	Conclusion .....	108
<b>Chapter 5 Electron Microscopy Study of the Effect of Cross-section Orientation on Directional Growth .....</b>		<b>117</b>

5.1	To Be Submitted: Electron Microscopy Study of Core–Shell Nanowire Bending and Twisting .....	117
5.2	Introduction.....	118
5.3	Methods.....	118
5.4	Results and Discussion .....	121
5.5	Conclusion .....	135
<b>Chapter 6 Conclusions and Future Work .....</b>		<b>141</b>
6.1	Conclusions.....	141
6.2	Road Ahead.....	143
<b>Chapter 7 Appendix.....</b>		<b>147</b>
	Supporting Information: X-ray diffraction reveals the amount of strain and homogeneity of extremely bent single nanowires .....	147
	Supporting Information: Phosphorus-Controlled Nanoepitaxy of Asymmetric GaAs–InP Core–Shell Bent Nanowires: Implications for Bottom-Up Nanowire Transistors and Sensors .....	149
	Supporting Information: Electron Microscopy Study of Core–Shell Nanowire Bending and Twisting.....	162

# List of Figures

Figure 1.1. The first reported case of bending in nanowires from asymmetric shell growth by Hilse et al.<sup>17</sup> ..... 2

Figure 1.2. Illustration of a nanowire sensor based on the actual device by Janissen et al.<sup>29</sup> ..... 3

Figure 2.1. Schematic representation of the radial NW structure and scanning electron microscope images of NWs studied in this work. (a) Sketch and side view SEM images for sample 1 with large bending radius. (b) Sketch and side view (left) and top view (right) SEM images for sample 2 with smaller bending radius. Side view SEM images in (a) and (b) are recorded under a tilt angle of 30° with respect to the surface normal. .... 19

Figure 2.2. (a) Sketch of the experimental setup. The focused X-ray beam illuminates part of the NW and produces a diffraction signal, as illustrated by the examples of detector images shown as insets. Typical detector images include diffraction signal of the illuminated NW and the substrate's crystal truncation rod (CTR). (b) Diffraction geometry with respect to the NW cross section at the sample azimuth  $\phi = 0^\circ$  in comparison with a top view SEM image. .... 22

Figure 2.3. (a) SEM image of NW1 with the central X-ray beam position of measurements 1, 2 and 3 marked. (b)  $q(x,y)$  plane extracted from the 3D RSM at the GaAs 111 Bragg reflection recorded at position 1. The signal between the black lines is shown in the line plot on the right and exhibits thickness oscillations corresponding to a size of  $120 \pm 8$  nm. (c) 2D projections of 3D RSMs measured at the three different

positions along the growth axis of NW1. For each position the  $q(z,y)$ ,  $q(z,x)$  and  $q(x,y)$  projections are shown by filled contour plots with a logarithmic intensity scale. .... 26

Figure 2.4. The projections of the combined RSMs for (a) NW1 and (b) NW2 of sample 1 and (c) NW3 of sample 2. The signal from the bent NWs spreads out along a segment of the Debye ring. An inset in panel (c) shows a magnification of the signal near  $q_y = 0$   $\text{\AA}^{-1}$  ..... 30

Figure 2.5. Transmission electron micrographs of NWs from sample 1 (a) and sample 2 (b). From nanowires that have their bending plane parallel to the imaging plane, the bending difference between the samples [cf. (a) and (b)] is evident. A high-resolution image of the region marked by the red rectangle in (b) is shown in (c). By further zooming in to the region marked by the blue rectangle, planar defects can be seen. In (c), the yellow lines highlight a twinned region. The inset in (c) shows an electron diffraction pattern recorded along the  $[110]$  cubic or equivalent  $[1120]$  hexagonal zone axis, respectively. .... 33

Figure 2.6. The reciprocal-space maps calculated for symmetrical diffraction  $\mathbf{h} = (111)$  using the exact kinematical formula (2.2) [panels (a) and (c)] and the stationary-phase method in equation (2.7) [(b) and (d)] for various positions  $z_0$  of the primary beam (parameters of the graphs). The filled and empty circles denote the end points of the non-rotated reciprocal-lattice vector  $\mathbf{h}$  and the rotated vector  $\mathbf{hB}$ , respectively. The intensity is displayed logarithmically. Color bar ticks are labeled with the decadic exponents of the intensity relative to the intensity maximum. .... 40

Figure 2.7. The reciprocal-space maps calculated using equation (2.2) for  $\mathbf{h} =$  **(111)** [panels (a), (b), (d) and (f)],  $\mathbf{h} =$  **(333)** (c) and  $\mathbf{h} =$  **(115)** (e). In (b) the simulation was carried out for two times larger bending radius, panel (d) shows the map calculated for two times larger NW radius, and in (f) the map shows the data for two times larger FWHM of the primary beam. The intensity is displayed logarithmically. Color bar ticks are labeled with the decadic exponents of the intensity relative to the intensity maximum..... 41

Figure 2.8. The **(111)** reciprocal-space maps calculated for small and large NW radii and strong bending ( $R = 1 \mu\text{m}$ ) in (a) and (b), and for the same NW radii and slight bending ( $R = 100 \mu\text{m}$ ) in (c) and (d). The intensity is displayed logarithmically. Color bar ticks are labeled with the decadic exponents of the intensity relative to the intensity maximum. .... 42

Figure 2.9. The linear dependence of the reciprocal bending radius on the width of the 111 diffraction maximum in the  $q_z$  direction calculated for various NW radii (parameters of the curves). The circles represent the data obtained by calculation using equation (2.2); the lines are their linear fits..... 43

Figure 2.10. Radial integration of the combined RSMs of (a) NW1 and (b) NW2 of sample 1 and (c) NW3 of sample 2. Data are plotted versus the angle  $\chi$  which specifies the tilt with respect to the substrate surface. .... 45

Figure 2.11. Comparison of experimentally measured intensity profiles (color lines) along the  $q_r$  direction with respect to calculation based on bent circular NWs (full and dotted black lines). Panels (a), (b) and (c) show data for NW1 and NW2 of sample 1 and NW3

of sample 2, respectively. Various tilt integration ranges indicated in the figure legend were used to obtain these curves from data shown in Figure 2.10. .... 47

Figure 3.1. Illustration of nanowire core and asymmetric shell growth. GaAs nanowire core growth (a,b) is carried out with sample rotation, while shell growth (c,d) is not. (a) Depiction of the Ga predeposition and Ga droplet formation in the patterned oxide holes. (b) GaAs core growth under Ga and As<sub>2</sub> fluxes. (c) Asymmetric InP shell deposition under In and P<sub>2</sub> fluxes. (d) Bent nanowire resulting from the growth process. .... 64

Figure 3.2. (a) Schematic representation of the nanowire core–shell cross-sectional geometry with a dashed bisection line. (b) Nanowire segment curvature as a function of shell thickness for three GaAs–InP core–shell nanowires (lattice mismatch of 3.8%) with core diameters of 50, 75, and 100 nm. Maximum curvature occurs for a shell thickness of 0.42× the nanowire diameter, as indicated with vertical dashed lines in (b). (c) Nanowire curvature as a function of shell thickness for different core–shell lattice mismatches for a 50 nm diameter core. .... 66

Figure 3.3. (a) Schematic representation of a nanowire’s bending evolution as the nanowire progresses from being straight to optimally bent. The deposition flux is indicated by black arrows, and the shading on the nanowires indicates the local shell thickness relative to the core diameter. (b–e) Modeling GaAs–InP core–shell nanowires with a 50 nm core diameter and an aspect ratio of 85 for four planar shell depositions: 5.9, 11.7, 23.4, and 46.9 nm at a deposition angle of 30°. (b) Wire geometries projected on a 2D plane. (c) Bending angle of the nanowire tips plotted as a function of planar

deposition. (d) Shell thickness along the wire length from the base to the tip. (e) Curvature along the wires. The legend in (b) corresponds to all panels..... 72

Figure 3.4. Effect of varying the angle of the incident flux with respect to the substrate normal for GaAs–InP wires. A deposition of 33.3 nm in the direction parallel to the incident flux was considered for flux angles of 10, 30, 50, 70, and 90 (corresponding to 32.8, 28.9, 21.4, 11.4, and 0 nm planar depositions, respectively), as indicated in the legend in (a), which corresponds to all panels. The wires are 4  $\mu\text{m}$  long with a 50 nm core diameter. (a) Wire geometry projected on a 2D plane. (b) Tip bending angle plotted as a function of the incident flux angle. (c) Local shell thickness along the wire length. The decreasing thickness toward the nanowire tip with increasing deposition angle results from self-shadowing. (d) Local curvature along the wire length..... 76

Figure 3.5. (a) Scanning electron micrograph of GaAs–InP core–shell nanowire pairs, separated by 600 nm and bent to the point of contact as a result of pair shadowing; the sample is tilted 30°, and the scale bar is 1  $\mu\text{m}$ . (b) Schematic illustration of one nanowire shadowing the incident flux from another; the scale bar represents shell thickness relative to the core diameter. (c) 3D plot of modeled wire geometry of three GaAs–InP nanowire pairs with different separation distances, bent by deposition incident from the left until the point of contact. The pair separations are (blue) 1.5, (green) 2, and (red) 2.5  $\mu\text{m}$ , and the corresponding planar depositions are 4.0, 6.0, and 9.7 nm, respectively. The deposition angle is 30°, and the core aspect ratio is 80 with a diameter of 50 nm. (d) Deposition and (e) curvature along the wire length for the pairs shown in (c). The solid and dashed lines correspond to the unshadowed and shadowed nanowires, respectively. 79

Figure 3.6. SEM image of an asymmetric GaAs–Al<sub>0.5</sub>In<sub>0.5</sub>As core–shell nanowire from ref 13 and fit with various shell deposition models. The deposition angle is 33.5° for the GaAs–Al<sub>0.5</sub>In<sub>0.5</sub>As core–shell nanowire. Three model fits are shown: (black line) uniform, unshadowed deposition with the nominal parameters from ref (13) (uniform 20 nm shell and 45 nm core diameter); (red dots) core diameter of 45 nm with a 3.9 nm planar deposition according to our model; (green dot–dashes) linear variation in the core diameter from 61 nm at the base to 30 nm at the tip and a planar deposition of 6.9 nm. The plots have been rescaled to account for the imaging angle of 45° from the substrate plane. The scale bar is 2 μm for the SEM image. (b) Curvature along the wire length from the three models. Reproduced from ref 13. Copyright 2018 American Chemical Society. ... 81

Figure 4.1. Illustration of the asymmetric core–shell nanowire MBE growth process. (a) Vapor–liquid–solid GaAs core growth showing the gallium droplet (red and translucent) on the top of the nanowire (red) under incident Ga and As<sub>2</sub> fluxes. (b) Consumption of the gallium droplet after core growth under As<sub>2</sub>. The arrows at the base of the nanowire in (a) and (b) indicate substrate rotation. (c) InP shell grown around the core with P<sub>2</sub> incident from the left and indium from the right. Both fluxes are unidirectional and have an azimuthal separation angle of 108° and an inclination angle of 33.5° measured from the substrate normal. (d) Top view of an asymmetric core–shell nanowire with a bending direction in line with the P<sub>2</sub> flux. This bending direction is observed for temperatures ≥380 °C. .... 95

Figure 4.2. SEM images of GaAs–InP core–shell nanowires grown at InP shell growth temperatures of 210 (a), 295 (b), 380 (c), and 440 °C (d). The top row shows plan view

micrographs, indicating the bending direction with respect to the incident  $I_n$  and  $P_2$  fluxes. The bottom row presents inclined side-view images aligned azimuthally perpendicular to either the incident  $I_n$  (a, b) or  $P_2$  (c, d) flux. The  $I_n$  and  $P_2$  source fluxes projected on the substrate are indicated by green and yellow arrows, respectively. Scale bars correspond to 1  $\mu\text{m}$ . ..... 97

Figure 4.3. TEM investigation of microtome cross sections for nanowires with shells grown at 210 °C (a, c) and 380 °C (d, f) presenting HAADF micrographs (a, d) and EDS maps (b, e). The EDS maps show that while shell growth occurred on all facets, it occurred predominantly on  $I_n$ -facing facets at 210 °C and  $P_2$ -facing facets at 380 °C. This is confirmed by plotting the shell thickness—extracted from the EDS maps—around the nanowire core, as illustrated in (c) and (f) for 210 and 380 °C, respectively. The incident flux directions are indicated in (a) and (d), corresponding to  $I_n$  impingement on facet 2 and  $P_2$  impingement on facet 4, respectively. The color and numbering of the EDS line scans correspond to the labels on the EDS maps, indicating the path around the nanowire shell. Scale bars are 50 nm. Both EDS maps are of net intensity. .... 99

Figure 4.4. Nanowire pairs. (a) SEM images of nanowire pairs with shells grown at 440 °C imaged at a tilt of 30°. The pairs are aligned in the  $P_2$  beam direction (incident from the right). Pairs are spaced base-to-base by 0.2, 0.6, and 1.2  $\mu\text{m}$ . Scale bars for (a) are 1  $\mu\text{m}$ , and yellow arrows indicate the  $P_2$  flux direction. (b, d) Net intensity EDS maps of a microtome cross section of a shadowed nanowire (b) and shadowing nanowire (d) of a pair separated by 0.6  $\mu\text{m}$  at the base of the nanowire with shells grown at 380 °C. (c, e) Shell thickness plots corresponding to (b) and (d). The direction of the direct  $P_2$  and  $I_n$

fluxes is indicated on the EDS maps. The yellow “x” in (b) indicates that the direct P<sub>2</sub> flux is blocked from reaching the nanowire. The color and numbering of the EDS line scans correspond to the labels on the EDS maps, indicating the path around the nanowire shell. Scale bars are 20 nm for the EDS maps. .... 105

Figure 4.5. TEM characterization of fused nanowire pairs. (a) Phase-contrast TEM micrograph of a fused nanowire pair. (b) High-magnification image of the interface region indicated by the red box in (a). (c) Bright-field micrograph of a second connected pair. (d, e) HAADF image (d) and corresponding EDS map (e) of Ga (red) and In (green) for a third connected nanowire pair. Scale bars are 50 nm in parts (a, c, d, and e) and 10 nm in (b). .... 108

Figure 5.1. SEM images of core–shell nanowires with InP shells grown under various incident flux azimuthal angles. (a) Projected P<sub>2</sub> beam along the < **110** > direction, (b–d) P<sub>2</sub> beam offset from < **110** > by 10°, 20° and 30°, respectively. Images are taken at a tilt of 30° from the substrate normal and the insets show the angle of the incident P<sub>2</sub> beam with respect to the nanowire shape. All scale bars are 1 μm. (e) shows the average curvatures measured in (a-d) plotted with respect to P<sub>2</sub> beam alignment relative to the < **110** > direction. .... 125

Figure 5.2. Top-view SEM Images of the bending series of Figure 5.1. Each sub-figure shows the nanowire in its entirety, along with three (5x) higher magnification images of the nanowire’s base (green), mid-section (red), and tip (cyan). The P<sub>2</sub> beam alignment in (a) is along the < **110** > direction and (b), (c), (d) are offset by 10°, 20°, and 30°, respectively. Black and white dashed lines denote the intersection of side facets. .... 127

Figure 5.3. (a) Overview STEM image of a dispersed nanowire grown with incident P2 flux  $10^\circ$  offset to the  $\langle 110 \rangle$  direction. This nanowire was imaged with 10 EDS line scans, as indicated on the image by the blue arrow boxes. For each location, a pair of scans rotated by  $23 \pm 4^\circ$  about the nanowire axis were collected as illustrated in the top left corner of (a). The scale bar is  $2 \mu\text{m}$ . (b–c) Exemplary thickness profiles extracted from a pair of EDS line scans. The blue and magenta dashed lines are the projection of the simulated core and shell, respectively. The EDS-measured core and shell data—scaled for appropriate thickness—are plotted in red (core) and green (shell). (d) Summary of measured diameter and shell area along the nanowire..... 129

Figure 5.4. Modeled nanowire cross-section from EDS measurements. The 10 cross-sections correspond to the 10 sections measured from the nanowire presented in Figure 5.3a from base to tip (a–j). The red area is the GaAs core and the green area is the shell. The radial lines in all panels are spaced by  $25 \text{ nm}$ . (k) Curvature ( $\kappa$ ) of the 10 cross-sections modeled with linear elastic theory. .... 131

Figure 5.5. Linear elastic modeling of nanowire cross-sections with  $100 \text{ nm}$  diameter cores. (a) Curvature ( $\kappa$ ) plotted as a function of shell area for four P2 beam alignments offset from the  $\langle 110 \rangle$  direction by  $0^\circ$  (black),  $10^\circ$  (red),  $20^\circ$  (blue), and  $30^\circ$  (green). Points A ( $3000 \text{ nm}^2$ ), B ( $6000 \text{ nm}^2$ ), and C ( $12000 \text{ nm}^2$ ) shows under-deposited, near-critically-deposited, and over-deposited shell areas, respectively. The strain energies for Point A (blue), Point B (red), and Point C (black) are plotted in (b) over different P2 beam alignments from  $0^\circ$  to  $60^\circ$ . .... 134

# Abbreviations

<b>ALD</b>	Atomic Layer Deposition
<b>As<sub>2</sub></b>	Arsenic Dimer
<b>COMS</b>	Complementary Metal-Oxide Semiconductor
<b>CTR</b>	Crystal Truncation Rod
<b>Chem-FET</b>	Chemical Field-Effect Transistor
<b>EELS</b>	Electron Energy Loss Spectroscopy
<b>EDS</b>	Energy Dispersive X-ray Spectroscopy
<b>EBL</b>	Electron Beam Lithography
<b>FET</b>	Field-Effect Transistor
<b>FIB</b>	Focused Ion Beam
<b>FWHM</b>	Full Width at Half Maximum
<b>GaAs</b>	Gallium Arsenide
<b>HAADF</b>	High-Angle Annular Dark-Field
<b>HF</b>	Hydrofluoric Acid
<b>InAsSb</b>	Indium Arsenide Antimonide
<b>InGaAs</b>	Indium Gallium Arsenide

<b>InP</b>	Indium Phosphide
<b>MBE</b>	Molecular Beam Epitaxy
<b>MOMBE</b>	Metal-organic Molecular Beam Epitaxy
<b>NH<sub>4</sub>F</b>	Ammonium Fluoride
<b>NW</b>	Nanowire
<b>P<sub>2</sub></b>	Phosphorus Dimer
<b>QD</b>	Quantum Dot
<b>RSM</b>	Reciprocal Space Mapping
<b>SDD</b>	Silicon Drift Detector
<b>SEM</b>	Scanning Electron Microscope
<b>Si</b>	Silicon
<b>STEM</b>	Scanning Transmission Electron Microscope
<b>TEM</b>	Transmission Electron Microscope

## Symbols

$\alpha$	Alpha
$\epsilon$	Epsilon
$\delta$	Delta
$\theta$	Theta
$\kappa$	Kappa
$\lambda$	Lambda
$\mu$	Mew
$\pi$	Pi
$\rho$	Rho
$\sigma$	Sigma
$\phi$	Phi
$\chi$	Chi
$\Psi$	Psi (uppercase)
$\Omega$	Omega (uppercase)

# Chapter 1

## Introduction

### 1.1 Background and Motivation

Nanowires are tiny wire-like structures with diameters in the hundreds of nanometres to a few nanometers and lengths normally ranging from micrometres to tens of micrometres. Semiconductor and metal nanowires are used in various applications such as photovoltaics,<sup>1,2</sup> betavoltaics,<sup>3</sup> thermoelectrics,<sup>4</sup> lasers,<sup>5,6</sup> single-photon sources,<sup>7,8</sup> transistors,<sup>9,10</sup> sensors,<sup>11</sup> and Josephson junctions.<sup>12</sup> Due to their size, nanowires have unique properties compared to bulk and thin films. Semiconductor nanowires with diameters in the tens of nanometres can experience radial confinement—confinement in 2-dimensions. Additionally, their small size allows them to be highly strained without plastic deformation, enabling growth on lattice-mismatched substrates without dislocations.<sup>13–15</sup> This capability to be strained also applies to nanowire core–shell heterostructures,<sup>16</sup> allowing their electronic and optical properties to be well controlled through strain engineering as well as unique combinations of lattice mismatched materials which would be highly defective in planar form.

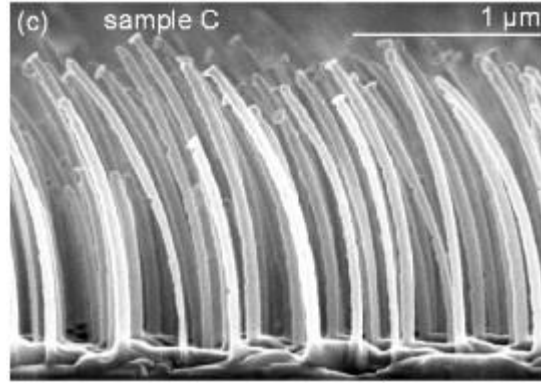


**Figure 1.1.** The first reported case of bending in nanowires from asymmetric shell growth by Hilse et al.<sup>17</sup>

Hilse et al.<sup>17</sup> presented the first report of nanowire bending resulting from heteroepitaxial growth of nanowire shells in 2009. The bending observed in the nanowire depicted in Figure 1.1 occurred during the growth of a GaAs–MnAs core-shell ferromagnet-semiconductor nanowire. This bending was a result of substrate rotation being fixed, which led to a directional flux resulting in the growth of an asymmetric shell. Further instances of nanowire bending were documented after: Kasanaboina et al.,<sup>18</sup> Keplinger et al.,<sup>19</sup> and Krogstrup et al.,<sup>20</sup> but it wasn't until nearly a decade later, in Lewis et al.,<sup>21</sup> that a directional flux was intentionally used to achieve asymmetric shell growth and nanowire bending. Both Hilse et al.<sup>17</sup> and Lewis et al.<sup>21</sup> employed molecular beam epitaxy (MBE) to create an asymmetric shell, though other techniques such as metal-organic MBE<sup>22</sup> and electron beam evaporation<sup>20,23,24</sup> have also been used. These growth methods share the characteristic that their deposition is directional or can be made directional, resulting in uneven growth around the nanowire.

Despite the vast potential applications and benefits of nanowires, they have not been widely incorporated into commercial devices. A key challenge is their high defect density because of their large surface area to volume ratio, stemming from dangling bonds (a defect) on the surfaces of the nanowires which act as recombination sites.<sup>25</sup> The high recombination in nanowires produces a high leakage current negatively effecting electronic nanowire devices and reduces the internal quantum efficiency of optical and optoelectronic devices.<sup>26-28</sup> Conversely, the high surface area is highly advantageous for sensors, enabling them to achieve ultra-sensitivity.

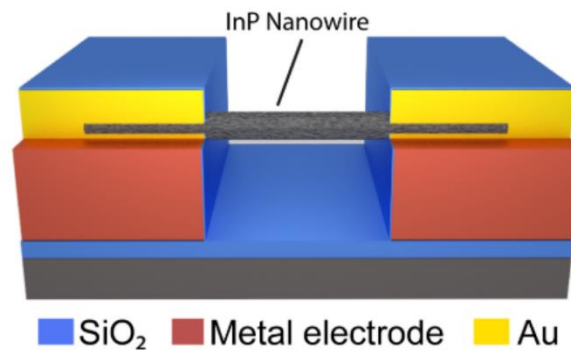


**Figure 1.2.** Illustration of a nanowire sensor based on the actual device by Janissen et al.<sup>29</sup>

The first semiconductor nanowire biosensor ion-selective field effect transistor (FET) device was made by Cui et al.<sup>30</sup> in 2001 to detect streptavidin (a protein), monoclonal antibiotin (an antibody), and  $\text{Ca}^{2+}$  (a metabolic indicator). This device uses a silicon nanowire as a transducer, where the binding of charged species targeted for detection to

the nanowire alters the nanowires' resistance. More recently, InP-based nanowires have been used in transducers for FET-based sensors in Janissen et al.<sup>29</sup> (illustrated in Figure 1.2) and Bai et al.<sup>31</sup> As well, bent, U-shaped, silicon nanowire probes have been fabricated with focused ion beam<sup>32,33</sup> and proposed for intracellular recording.<sup>34</sup> These nanowire sensors can share common characteristics, high sensitivity resulting from their high surface area to volume ratio, real-time detection, and the ability for the transducer (the nanowire) to be located off the substrate enhancing detection by improving mass-transport of target species.<sup>35-39</sup> Although such sensors have proven effective, the main hurdle for commercializing nanowire sensors is their fabrication. Presently, there isn't a reliable high-yield method to mass-produce nanowire sensors where materials and device configurations are optimized for sensor applications.

## 1.2 Overview of Thesis

This thesis presents a series of published and forthcoming journal articles that explore the fabrication of core–asymmetric shell nanowire heterostructures with directional nanoepitaxy (growth) and their bending behavior resulting from elastic relaxation. The articles will illustrate my work during my graduate studies on asymmetric shell growth and how the bending of nanowires offers a practical method for advancing future nanowire devices. Chapters 2–5 are of included articles, and notably share some methodological approaches, well also discussing analogous concepts and repeating cited works in their introductions because of their focus on directional growth, bending, and the potential applications of these phenomena in the creation of sensor devices.

Chapter 2 presents a study of bent GaAs-(Al,In)As core-shell nanowires produced through directional shell nanoepitaxy. X-ray diffraction along the bent nanowire from base to tip demonstrates that bent nanowires exhibit variations in bending linked to measured strain. My model correlates these variations with differences in shell thickness. This chapter highlights the inherent complexity of bending nanowires via directional nanoepitaxy, as evidenced by the non-uniform final morphology of the nanowire.

Chapter 3 delves into the complexity of directional nanowire shell deposition by modeling the bending evolution of nanowires during directional nanoepitaxy. Various parameters such as core diameter, lattice mismatch, incident flux angle, and shell thickness are explored to comprehend their individual impacts on bending. Additionally, nanowire shadowing is modeled, revealing that it facilitates the connection of nanowires by reducing the bending required for wire-to-wire connection. This study lays the groundwork for understanding directional nanoepitaxy in the context of fabrication processes.

Chapter 4 focuses on the local variations found around GaAs-InP core-shell nanowire cross-sections with asymmetric shells produced through directional nanoepitaxy. We show that the InP shell can grow via two distinct modes: In diffusion-limited and phosphorus-controlled. In the diffusion-limited mode, the shell distribution is related to the indium flux on a nanowires' side facets, whereas in the phosphorus-controlled mode, the shell thickness on a side facet is linearly proportional to the phosphorus flux received relative to other facets, which makes this method highly controllable. When nanowires are shadowed in this growth mode, they exhibit uniform shell growth, indicating an

isotropic scattered or re-emitted flux of phosphorus. Additionally, when a shadowed nanowire contacts an unshadowed one—bent together—the nanowires fuse, highlighting potential application of this method for device fabrication.

Chapter 5 examines the impact of deposition flux orientation relative to the nanowire crystallographic orientation on the bending and shell distribution of GaAs-InP core-shell nanowires. We show that the phosphorus beam orientation with respect to crystallographic orientation affect nanowire shape, bending, and twisting. An electron tomography technique is developed and used to characterize shell distribution, reducing the number of scans and angle range needed from traditional electron tomography. The chapter reveals a large difference in bending for different orientations and that twisting is due to strain energy minimization during shell growth, leading to energetically favorable shell distributions which cause bending in the  $\langle 1\bar{1}0 \rangle$  or  $\langle 11\bar{2} \rangle$  crystallographic directions. Overall, the chapter shows crystallographic orientation is a critical fabrication parameter for bent nanowire devices.

In conclusion, in chapter 6, I will discuss the overall impact of my research during my graduate studies, its potential applications in strain engineering, and how these techniques can be employed to create nanowire arches as templates for mass-producible sensors. I will also outline the steps required to develop a fabrication method for these nanowire sensor devices. Connecting and fabricating nanowire arches is feasible; however, a device will depend on initial substrate preparation, forming electrical contacts at the base of the nanowires or substrate, and electrically isolating the bases of connected nanowires before a device can be fully realized.

## References

- (1) Tian, B.; Kempa, T. J.; Lieber, C. M. Single Nanowire Photovoltaics. *Chem Soc Rev* 2009, 38 (1), 16–24. <https://doi.org/10.1039/b718703n>.
- (2) Czaban, J. A.; Thompson, D. A.; LaPierre, R. R. GaAs Core-Shell Nanowires for Photovoltaic Applications. *Nano Lett* 2009, 9 (1), 148–154. <https://doi.org/10.1021/nl802700u>.
- (3) McNamee, S.; Wagner, D.; Fiordaliso, E. M.; Novog, D.; Lapierre, R. R. GaP Nanowire Betavoltaic Device. *Nanotechnology* 2019, 30 (7). <https://doi.org/10.1088/1361-6528/aaf30a>.
- (4) Boukai, A. I.; Bunimovich, Y.; Tahir-Kheli, J.; Yu, J. K.; Goddard, W. A.; Heath, J. R. Silicon Nanowires as Efficient Thermoelectric Materials. *Nature* 2008, 451 (7175), 168–171. <https://doi.org/10.1038/nature06458>.
- (5) Johnson, J. C.; Yan, H.; Schaller, R. D.; Haber, L. H.; Saykally, R. J.; Yang, P. Single Nanowire Lasers. *Journal of Physical Chemistry B* 2001, 105 (46), 11387–11390. <https://doi.org/10.1021/jp012304t>.
- (6) Grosshans, F.; Van Asschet, G.; Wenger, J.; Brouri, R.; Cerf, N. J.; Grangier, P. Quantum Key Distribution Using Gaussian-Modulated Coherent States. *Nature* 2003, 421 (6920), 238–241. <https://doi.org/10.1038/nature01289>.

- (7) Tribu, A.; Sallen, G.; Aichele, T.; André, R.; Poizat, J. P.; Bougerol, C.; Tatarenko, S.; Kheng, K. A High-Temperature Single-Photon Source from Nanowire Quantum Dots. *Nano Lett* 2008, 8 (12), 4326–4329. <https://doi.org/10.1021/nl802160z>.
- (8) Babinec, T. M.; Hausmann, B. J. M.; Khan, M.; Zhang, Y.; Maze, J. R.; Hemmer, P. R.; Lončar, M. A Diamond Nanowire Single-Photon Source. *Nat Nanotechnol* 2010, 5 (3), 195–199. <https://doi.org/10.1038/nnano.2010.6>.
- (9) Quitariano, N. J.; Kamins, T. I. Integratable Nanowire Transistors. *Nano Lett* 2008, 8 (12), 4410–4414. <https://doi.org/10.1021/nl802292h>.
- (10) Colinge, J. P.; Lee, C. W.; Afzalilian, A.; Akhavan, N. D.; Yan, R.; Ferain, I.; Razavi, P.; O'Neill, B.; Blake, A.; White, M.; Kelleher, A. M.; McCarthy, B.; Murphy, R. Nanowire Transistors without Junctions. *Nat Nanotechnol* 2010, 5 (3), 225–229. <https://doi.org/10.1038/nnano.2010.15>.
- (11) Ramgir, N. S.; Yang, Y.; Zacharias, M. Nanowire-Based Sensors. *Small*. August 16, 2010, pp 1705–1722. <https://doi.org/10.1002/sml.201000972>.
- (12) Nilsson, H. A.; Samuelsson, P.; Caroff, P.; Xu, H. Q. Supercurrent and Multiple Andreev Reflections in an InSb Nanowire Josephson Junction. *Nano Lett* 2012, 12 (1), 228–233. <https://doi.org/10.1021/nl203380w>.
- (13) Raychaudhuri, S.; Yu, E. T. Critical Dimensions in Coherently Strained Coaxial Nanowire Heterostructures. *J Appl Phys* 2006, 99 (11). <https://doi.org/10.1063/1.2202697>.

- (14) Glas, F. Critical Dimensions for the Plastic Relaxation of Strained Axial Heterostructures in Free-Standing Nanowires. *Phys Rev B Condens Matter Mater Phys* 2006, 74 (12). <https://doi.org/10.1103/PhysRevB.74.121302>.
- (15) Ye, H.; Lu, P.; Yu, Z.; Song, Y.; Wang, D.; Wang, S. Critical Thickness and Radius for Axial Heterostructure Nanowires Using Finite-Element Method. *Nano Lett* 2009, 9 (5), 1921–1925. <https://doi.org/10.1021/nl900055x>.
- (16) Balaghi, L.; Bussone, G.; Grifone, R.; Hübner, R.; Grenzer, J.; Ghorbani-Asl, M.; Krasheninnikov, A. V.; Schneider, H.; Helm, M.; Dimakis, E. Widely Tunable GaAs Bandgap via Strain Engineering in Core/Shell Nanowires with Large Lattice Mismatch. *Nat Commun* 2019, 10 (1), 1–10. <https://doi.org/10.1038/s41467-019-10654-7>.
- (17) Hilse, M.; Takagaki, Y.; Herfort, J.; Ramsteiner, M.; Herrmann, C.; Breuer, S.; Geelhaar, L.; Riechert, H. Ferromagnet-Semiconductor Nanowire Coaxial Heterostructures Grown by Molecular-Beam Epitaxy. *Appl Phys Lett* 2009, 95 (13). <https://doi.org/10.1063/1.3240405>.
- (18) Kasanaboina, P. K.; Ojha, S. K.; Sami, S. U.; Reynolds, C. L.; Liu, Y.; Iyer, S. Bandgap Tuning of GaAs/GaAsSb Core-Shell Nanowires Grown by Molecular Beam Epitaxy. *Semicond Sci Technol* 2015, 30 (10). <https://doi.org/10.1088/0268-1242/30/10/105036>.
- (19) Keplinger, M.; Kriegner, D.; Stangl, J.; Mårtensson, T.; Mandl, B.; Wintersberger, E.; Bauer, G. Core-Shell Nanowires: From the Ensemble to Single-Wire

- Characterization. Nucl Instrum Methods Phys Res B 2010, 268 (3–4), 316–319.  
<https://doi.org/10.1016/j.nimb.2009.09.043>.
- (20) Krogstrup, P.; Ziino, N. L. B.; Chang, W.; Albrecht, S. M.; Madsen, M. H.; Johnson, E.; Nygård, J.; Marcus, C. M.; Jespersen, T. S. Epitaxy of Semiconductor-Superconductor Nanowires. Nat Mater 2015, 14 (4), 400–406.  
<https://doi.org/10.1038/nmat4176>.
- (21) Lewis, R. B.; Corfdir, P.; Küpers, H.; Flissikowski, T.; Brandt, O.; Geelhaar, L. Nanowires Bending over Backward from Strain Partitioning in Asymmetric Core-Shell Heterostructures. Nano Lett 2018, 18 (4), 2343–2350.  
<https://doi.org/10.1021/acs.nanolett.7b05221>.
- (22) Greenberg, Y.; Kelrich, A.; Cohen, S.; Kar-Narayan, S.; Ritter, D.; Calahorra, Y. Strain-Mediated Bending of InP Nanowires through the Growth of an Asymmetric InAs Shell. Nanomaterials 2019, 9 (9), 1–11. <https://doi.org/10.3390/nano9091327>.
- (23) Bjergfelt, M.; Carrad, D. J.; Kanne, T.; Aagesen, M.; Fiordaliso, E. M.; Johnson, E. Superconducting Vanadium / Indium-Arsenide Hybrid Nanowires. Nanotechnology 2019, 30 (29), 294005. <https://doi.org/10.1088/1361-6528/ab15fc>.
- (24) Xu, Y.; Li, L.; Zang, Y.; Hu, J.; Li, Z.; Chen, H.; Zhang, G.; Xia, C.; Cho, J. Forward Bending of Silicon Nanowires Induced by Strain Distribution in Asymmetric Growth. Mater Lett 2021, 297, 129929.  
<https://doi.org/10.1016/j.matlet.2021.129929>.

- (25) Gatos, H. C. Dangling Bonds in III-V Compounds. *J Appl Phys* 1961, 32 (7), 1232–1234. <https://doi.org/10.1063/1.1736209>.
- (26) Simpkins, B. S.; Mastro, M. A.; Eddy, C. R.; Pehrsson, P. E. Surface Depletion Effects in Semiconducting Nanowires. *J Appl Phys* 2008, 103 (10). <https://doi.org/10.1063/1.2932072>.
- (27) Chia, A. C. E.; Lapierre, R. R. Electrostatic Model of Radial Pn Junction Nanowires. *J Appl Phys* 2013, 114 (7). <https://doi.org/10.1063/1.4818958>.
- (28) Borblik, V. Electrostatics of Nanowire Radial p–n Heterojunctions. *J Electron Mater* 2018, 47 (7), 4022–4027. <https://doi.org/10.1007/s11664-018-6288-4>.
- (29) Janissen, R.; Sahoo, P. K.; Santos, C. A.; Da Silva, A. M.; Von Zuben, A. A. G.; Souto, D. E. P.; Costa, A. D. T.; Celedon, P.; Zanchin, N. I. T.; Almeida, D. B.; Oliveira, D. S.; Kubota, L. T.; Cesar, C. L.; Souza, A. P. D.; Cotta, M. A. InP Nanowire Biosensor with Tailored Biofunctionalization: Ultrasensitive and Highly Selective Disease Biomarker Detection. *Nano Lett* 2017, 17 (10), 5938–5949. <https://doi.org/10.1021/acs.nanolett.7b01803>.
- (30) Cui Yi; Wei Qingqiao; Park Hongkun; Lieber Charles M. Nanowire Nanosensors for Highly Sensitive and Selective of Biological and Chemical Species. *Science* (1979) 2001, 293 (5533), 1289–1292. <https://doi.org/10.1126/science.1062711>.
- (31) Bai, M.; Huang, H.; Liu, Z.; Zhan, T.; Xia, S.; Li, X.; Sibirev, N.; Bouravleuv, A.; Dubrovskii, V. G.; Cirilin, G. InAs/InP Core/Shell Nanowire Gas Sensor: Effects of

- InP Shell on Sensitivity and Long-Term Stability. *Appl Surf Sci* 2019, 498 (February), 143756. <https://doi.org/10.1016/j.apsusc.2019.143756>.
- (32) Zhao, Y.; Yao, J.; Xu, L.; Mankin, M. N.; Zhu, Y.; Wu, H.; Mai, L.; Zhang, Q.; Lieber, C. M. Shape-Controlled Deterministic Assembly of Nanowires. *Nano Lett* 2016, 16 (4), 2644–2650. <https://doi.org/10.1021/acs.nanolett.6b00292>.
- (33) Zhao, Y.; You, S. S.; Zhang, A.; Lee, J. H.; Huang, J.; Lieber, C. M. Scalable Ultrasmall Three-Dimensional Nanowire Transistor Probes for Intracellular Recording. *Nat Nanotechnol* 2019, 14 (8), 783–790. <https://doi.org/10.1038/s41565-019-0478-y>.
- (34) Prominski, A.; Tian, B. Bridging the Gap — Biomimetic Design of Bioelectronic Interfaces. *Current Opinion in Biotechnology*. Elsevier Ltd December 1, 2021, pp 69–75. <https://doi.org/10.1016/j.copbio.2021.10.005>.
- (35) Choi, J.; Kim, J. Highly Sensitive Hydrogen Sensor Based on Suspended, Functionalized Single Tungsten Nanowire Bridge. *Sens Actuators B Chem* 2009, 136 (1), 92–98. <https://doi.org/10.1016/j.snb.2008.10.046>.
- (36) Lim, Y.; Lee, Y.; Lee, J.; Shin, H. Circumferentially Grown ZnO Nanowire Forest on a Suspended Carbon Nanowire for a Highly Sensitive Gas Sensor; 2015; Vol. MEMS 2015 28th.
- (37) Lim, Y.; Lee, Y.; Heo, J. Il; Shin, H. Highly Sensitive Hydrogen Gas Sensor Based on a Suspended Palladium/Carbon Nanowire Fabricated via Batch Microfabrication

Processes. *Sens Actuators B Chem* 2015, 210, 218–224.

<https://doi.org/10.1016/j.snb.2014.12.109>.

- (38) Lim, Y.; Kim, S.; Kwon, Y. M.; Baik, J. M.; Shin, H. A Highly Sensitive Gas-Sensing Platform Based on a Metal-Oxide Nanowire Forest Grown on a Suspended Carbon Nanowire Fabricated at a Wafer Level. *Sens Actuators B Chem* 2018, 260, 55–62. <https://doi.org/10.1016/j.snb.2017.12.167>.

- (39) Baek, D. H.; Choi, J.; Kim, J. Fabrication of Suspended Nanowires for Highly Sensitive Gas Sensing. *Sens Actuators B Chem* 2019, 284, 362–368. <https://doi.org/10.1016/j.snb.2018.12.159>.

## Chapter 2

### Micro- and Nano-focused X-ray Diffraction

### Analysis of Bent GaAs–Al<sub>x</sub>Ga<sub>x-1</sub>As Core–shell

### Nanowires

#### 2.1 Published: X-ray diffraction reveals the amount of strain and homogeneity of extremely bent single nanowires

##### Declaration

**X-ray diffraction reveals the amount of strain and homogeneity of extremely bent single nanowires** [ *Journal of Applied Crystallography*, 53(5), 1310–1320.]

Authors: Arman Davtyan, Dominik Kriegner, Václav Holý, Ali AlHassan, Ryan B.

Lewis, Spencer McDermott, Lutz Geelhaar, Danial Bahrami, Taseer Anjum, Zhe Ren,

Carsten Richter, Dmitri Novikov, Julian Müller, Benjamin Butz and Ullrich Pietsch

Published in **October 2020** in the **Journal of Applied Crystallography**, manuscript is cited above and linked here, <https://doi.org/10.1107/S1600576720011516>.

## 2.2 Introduction

Using semiconductor nanowires (NWs) one is able to design epitaxial heterostructures composed of materials with large lattice mismatch. Heterostructures can be realized along or perpendicular to the growth direction, forming axial or radial heterostructures, respectively.<sup>1-3</sup> For axial NW heterostructures, lattice mismatches of up to 7% – unachievable in planar growth – have been realized in the InAs/InSb system.<sup>4</sup> For GaAs NWs, good control of growth developed over recent years includes control of their crystallographic structure<sup>5</sup> and nucleation sites by using patterned substrates.<sup>6</sup> Control of the nucleation site is especially appealing for device applications and improves size and structure homogeneity. It also allows the investigation of properties of the same NW by various experimental techniques, as shown for example for GaAs-based core–multishell NWs by AlHassan *et al.*<sup>7</sup>

The next generation of epitaxial NW heterostructures promises greater control of strain engineering. This concept was demonstrated first by growing a highly mismatched shell asymmetrically around the NW core, leading to the bending of the NW.<sup>8</sup> In particular, GaAs core NWs were grown by molecular beam epitaxy (MBE) onto an Si(111) substrate and  $\text{In}_x\text{Al}_{(1-x)}\text{As}$  shells were preferentially grown onto one side of the core only, for example onto the  $(1\bar{1}0)$  plane. This can be imagined as being similar to a bimetallic strip, which bends because of the different thermal expansion coefficients of two adjacent metals. In the case of NWs, in addition to different thermal properties, the lattice mismatch between core and shell material leads to bending in a predetermined direction.

For the particular case described above, this means the  $(1\bar{1}0)$  plane of the GaAs core is tensilely strained at the core/shell interface but compressively strained in the opposite side plane with no adjacent shell.

Using NWs, sizable strains – otherwise only obtainable by a method named strain redistribution in micro-bridges produced by complicated lithographic processing<sup>9</sup> – can be achieved. Strain in micro-bridges, typically measured by either Raman spectroscopy<sup>10</sup> or scanning X-ray diffraction,<sup>11</sup> has been pursued to manipulate the electronic properties of materials, *e.g.* making Ge a direct band gap material.<sup>12</sup> Band gap engineering was also performed in straight GaAs/ $\text{In}_x\text{Ga}_{(1-x)}\text{As}$  core–shell NWs, and hydrostatic strains of up to 7% could be achieved.<sup>13</sup> Owing to the large aspect ratio of NWs, not only the absolute values of strain but also the strain gradient can be sizable in bent NWs. The change of strain across the NW diameter produces a significant impact on the electronic properties. First, the varying strain leads to a gradient of the electronic band gap and therefore a redistribution of charge carriers.<sup>8</sup> Furthermore, it creates an additional electric field via the flexoelectric effect.<sup>14</sup> The latter has not been observed for GaAs so far, but might be accessible in NWs with sufficiently low bending radius. Moreover, under excitation of charge carriers by a laser, this flexoelectric field becomes screened and provides a macroscopic elastic response via the converse flexoelectric effect. It is expected that the flexoelectric response may change the bending radius of the NW. Observation of the predicted effect, however, requires homogeneously bent, monophasic [*i.e.* without zinc-blende/wurtzite (ZB/WZ) polytypism] NWs without plastic deformation. Here the homogeneity of the bending is related to homogeneity of shell composition as well as

core and shell thickness along the entire NW length. However, during deposition of the shell material by MBE, the NW bending radius is continuously changing, and as a result the projected flux on the NW sidewall varies with time and along the axis of the NW.

In this work, we report on the use of X-ray micro-diffraction to study the bending of core-shell NWs and its homogeneity. X-ray diffraction using micro- and nano-focused X-ray beams has already been used for more than a decade to study shape and strain of nanowires either via phase retrieval<sup>15-17</sup> or by analysis methods supported by finite element modeling.<sup>18, 19</sup> Bending in NWs has been studied in InAs/InAsP and GaAs/GaInP core-shell<sup>20, 21</sup> NWs, but with bending radii far larger than found in our work. Owing to the significantly stronger bending as compared to previous studies, our experiment required a modification of the diffraction setup along with a new scheme of data presentation. Moreover, current approaches of X-ray theory are limited to bending radii of the order of above 10  $\mu\text{m}$ <sup>22, 23</sup> and no theory exists so far that is applicable to systems with such small bending radius. Using micro-focused X-ray beams, we study the bending of individual NWs and develop a suitable X-ray diffraction theory based on the kinematical approximation. The X-ray diffraction results are supported by electron microscopy investigations which image the bending. Moreover, in the diffraction analysis we directly assess not only the bending but also the strain imprinted in the NW core, which determines the electronic properties of the material.

The manuscript is organized as follows: In Section 2 we give details about the sample characteristics and experimental setup used for the X-ray diffraction measurements. In Section 3 we present our X-ray diffraction data, which are complemented by the

transmission electron microscope investigations described in Section 4. Section 5 describes the X-ray diffraction theory for highly bent crystals. Finally, we discuss the results and compare the experimental data with simulations.

## 2.3 Experimental

The NWs studied in this work were grown by MBE onto patterned Si(111) substrates. They consist of a GaAs core grown along the Si [111] direction, and are bent along the  $(1\bar{1}0)$  direction as a result of an asymmetric shell grown onto one side of the core only. The source fluxes were incident at an angle of  $33.5^\circ$  from the substrate normal. We report on two samples with bending radii, estimated from scanning and transmission electron microscopy (SEM and TEM) investigations, of approximately 8–13  $\mu\text{m}$  (sample 1) and 2–3.5  $\mu\text{m}$  (sample 2). Figure 2.1 shows a schematic representation of the radial NW structure together with scanning electron microscopy images of the particular NWs investigated by X-ray diffraction. The NWs of sample 1 have considerably larger bending radius in comparison with NWs from sample 2, as can be seen in the SEM images in Figure 2. 1. Sample 1 [whose growth was reported earlier by Lewis *et al.*<sup>8</sup>] is composed of GaAs/InAs/GaAs/Al<sub>0.3</sub>Ga<sub>0.7</sub>As/Al<sub>0.5</sub>In<sub>0.5</sub>As core–multishell NWs with a 75 nm GaAs core, a 2–3 nm InAs shell including quantum dots (QDs), a 5 nm GaAs shell, a 10 nm Al<sub>0.3</sub>Ga<sub>0.7</sub>As shell and an outermost partially grown shell of Al<sub>0.5</sub>In<sub>0.5</sub>As with a nominal thickness of 40 nm. Note that the thickness of the core denotes the separation between opposing facets, while the shell thicknesses correspond to the thickness of the shell layer on a given facet. The complicated radial structure is beneficial for the optical properties

of the NWs that were studied by Lewis *et al.*<sup>8</sup> Owing to the small thickness of the InAs shell and QDs, we expect that they can be neglected for the present study. Sample 2 consists of a nominally 40 nm thick  $\text{Al}_{0.5}\text{In}_{0.5}\text{As}$  partial shell grown onto a GaAs core with 7 nm diameter. Because of the different ratio of effective core versus asymmetric shell thickness, the NWs of sample 2 are more strongly bent, i.e. have a smaller bending radius.

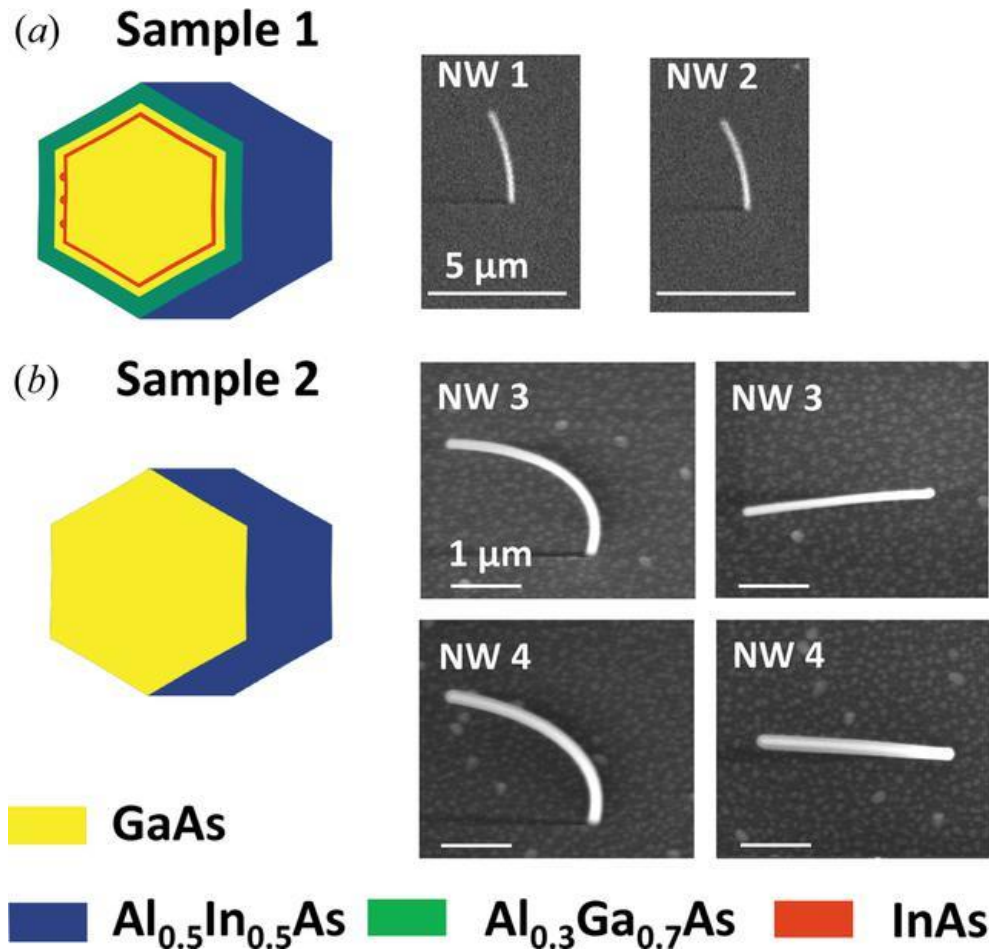


**Figure 2.1.** Schematic representation of the radial NW structure and scanning electron microscope images of NWs studied in this work. (a) Sketch and side view SEM images

for sample 1 with large bending radius. (b) Sketch and side view (left) and top view (right) SEM images for sample 2 with smaller bending radius. Side view SEM images in (a) and (b) are recorded under a tilt angle of  $30^\circ$  with respect to the surface normal.

The bending radius of the NWs can be extracted from SEM images by overlaying the NW axis with ellipses and adjusting the radius to fit the observations. Because the tilt angle with respect to the surface normal is  $30^\circ$ , ellipses with an aspect ratio of 2:1 have to be used. For NW1 and NW2 of sample 1 we obtain bending radii of 10–13  $\mu\text{m}$ . In contrast, NW3 and NW4 have considerably greater bending and correspondingly smaller radii of 2.5–3.5  $\mu\text{m}$ . The process of overlaying ellipses on the SEM images, in particular for the NWs of sample 2, does not allow us to obtain a perfect match for the full wire using only one bending radius. The values determined using this method therefore represent the average bending of the full wire. To obtain a more local bending radius from the SEM images we determined the position of the NW's center line along the NW and numerically calculated the local bending radius using finite difference differentiation. Using this method we obtain radii consistent with those mentioned above for the central parts of the NWs. However, especially for the bottom parts, the bending radii exceed the given ranges, indicating that the bending closer to the substrate interface is significantly lower.

While from SEM images one can determine only the bending of the NW shape, X-ray diffraction allows one to study the effect on the atomic distances within the NW. Our diffraction studies were performed using micro-focused X-ray beams in order to obtain the signal of (parts of) individual NWs. In particular, NW1 and NW2 were measured with

a coherent X-ray beam at beamline ID01 of ESRF (Grenoble, France), focused down to an FWHM of  $0.23 \times 0.3 \mu\text{m}$  [vertical (V)  $\times$  horizontal (H)] and with a photon energy of 9 keV. NW3 and NW4 were measured at beamline P23 of PETRA III, DESY (Hamburg, Germany), with an X-ray beam focused down to an FWHM of  $0.8 \times 3 \mu\text{m}$  (V  $\times$  H) and photon energy of 10 keV. As the two experimental setups are qualitatively similar, we present the general experimental setup in Figure 2.2. A convergent X-ray beam is positioned at various points along the NW and the corresponding diffraction data are collected. Examples of detector images are shown in Figure 2.2*a*. The images typically include broad signals originating from the NW and a sharp crystal truncation rod from the substrate. In order to present the data of the bent NWs over the entire length, we choose a reciprocal-space coordinate system aligned with the single-crystalline substrate. The  $q$  space is defined such that the  $q_z$  vector is along the substrate's [111] direction (surface normal). The  $q_x$  direction coincides with the X-ray beam direction at zero goniometer angles and corresponds to the  $[11\bar{2}]$  direction of the substrate. Therefore,  $q_y$  is along the  $[\bar{1}10]$  direction of the substrate and is also roughly within the plane in which the NWs bend.

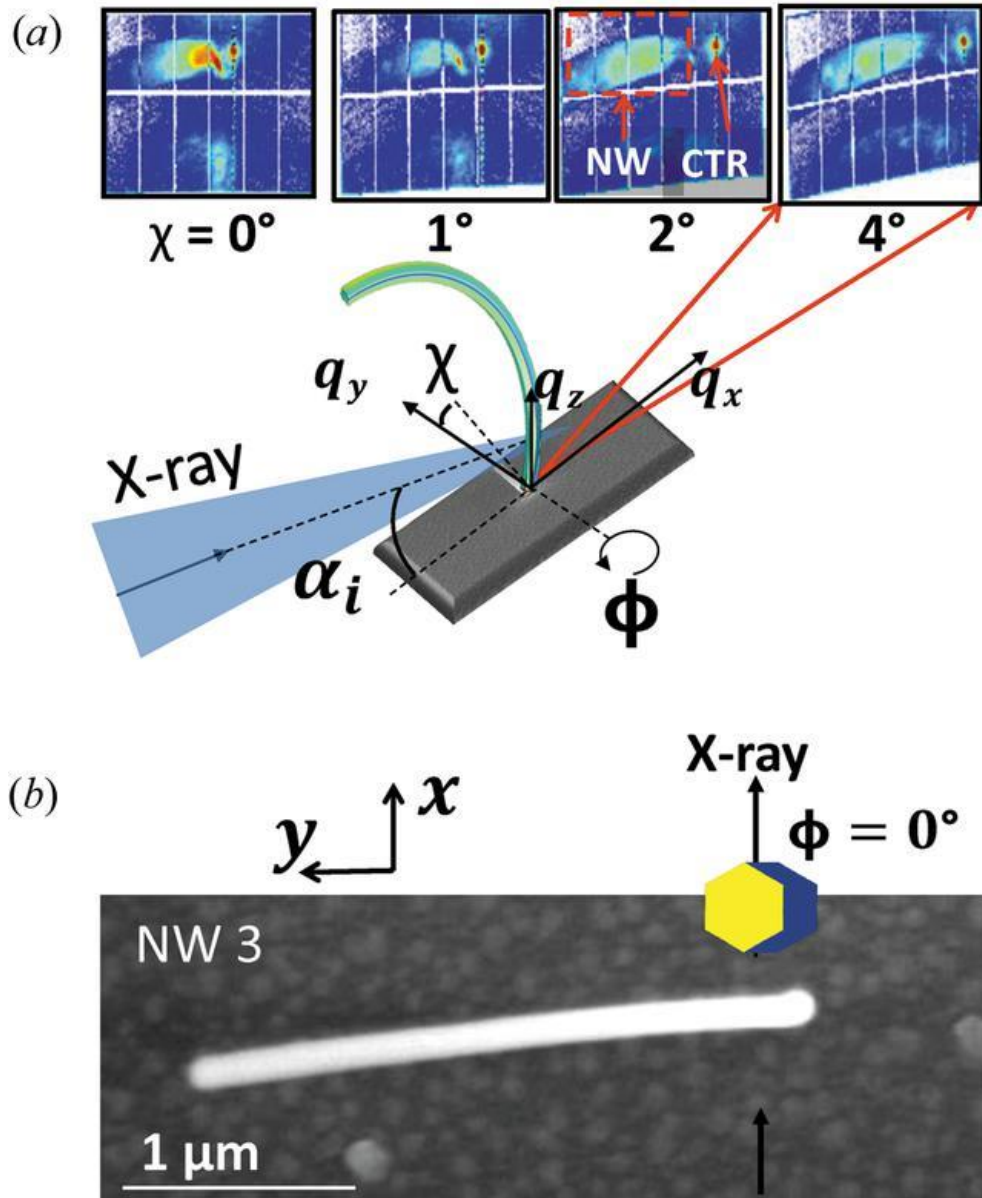


**Figure 2.2.** (a) Sketch of the experimental setup. The focused X-ray beam illuminates part of the NW and produces a diffraction signal, as illustrated by the examples of detector images shown as insets. Typical detector images include diffraction signal of the illuminated NW and the substrate's crystal truncation rod (CTR). (b) Diffraction geometry with respect to the NW cross section at the sample azimuth  $\phi = 0^\circ$  in comparison with a top view SEM image.

Our studies focus on diffraction from the GaAs {111} lattice planes, or the equivalent {0002} WZ phase lattice planes, which for the bottom part of the NWs are parallel to the {111} planes in the substrate. The diffraction signal therefore is located along the  $q_z$  direction with vanishing  $x, y$  components. Given the photon energies of 9 keV (NW1 and NW2) and 10 keV (NW3 and NW4) the Bragg condition for the GaAs volume near the substrate is therefore fulfilled at angles  $\alpha_i = 12.18$  and  $10.95^\circ$ , respectively. Using these incidence angles and corresponding detector angles, we located the bottom parts of the NWs by scanning the sample surface through the beam at the Bragg condition via the  $x, y$  translation stages.

The bending of the upper parts of the NWs causes the diffraction signal of the corresponding parts to tilt. Within our chosen reciprocal-space coordinate system, this tilt is predominantly along the  $q_y$  direction. A small  $q_x$  component exists only because of a slight offset of the plane in which the NWs bend [see for example Figure 2.2*b*]. So in order to collect diffraction signal from these bent parts, in addition to the beam location on the sample, the goniometer angles need to be adjusted. Several possibilities exist to adjust the goniometer angles. Given the experimental possibilities at beamlines ID01 and P23 we had to choose two different strategies: At ID01 (NW1 and NW2) we used the sample azimuth  $\phi$  [see Figure 2.2*a*] and the corresponding detector rotation to follow the diffraction signal along the NWs. On the other hand at beamline P23 (NW3 and NW4) we used the sample tilt  $\chi$  to maintain the Bragg condition for the investigated segment without any change of the detector position. For NW3 the diffraction signal was recorded for tilt angles from  $0$  up to  $50^\circ$  with a step size of  $0.5\text{--}3^\circ$ , always ensuring that some

overlap of subsequent reciprocal-space maps (RSMs) existed. Insets in Figure 2.2a show average detector images of rocking curve measurements for various tilt angles. Because NW3 was grown slightly tilted with respect to the  $y$  axis in addition to  $\chi$ , a small correction of the sample azimuth ( $\phi$ ) had to be used to align NW3 into the diffraction condition. The SEM image in Figure 2.2b corresponds to the case of  $\phi = 0^\circ$ , which shows that for different parts of the NW different  $\phi$  angles have to be used. In both experiments the X-ray beam illuminates the NW roughly from the direction perpendicular to the small facets of the NWs having irregular octagonal shape resulting from the asymmetrically grown shell [see inset in Figure 2. 2b]. While this condition is fulfilled for the full NW using the geometry at P23, it is only true when studying the bottom parts at beamline ID01. Two-dimensional detectors at distances of 569 mm (4 chip MaxiPix detector) and 1020 mm (2D Lambda detector) were used at ID01 and P23, respectively. Three-dimensional RSMs were recorded either by scanning the incidence angle (P23) or at fixed incidence angle but varying the X-ray energy between 8.5 and 9.5 keV with a step size of 0.04 keV (ID01). At ID01, preliminary data processing was performed using the *XSOCS* package.<sup>24</sup>

Prior to NW measurements at beamline ID01 of the ESRF, the X-ray wavefront was characterized by means of 2D ptychography in the forward direction using a Siemens star test sample. The X-ray wavefront was reconstructed using the *PyNX* software<sup>25</sup> and is presented in supplementary Figure S1. It can be seen that, besides the central main peak, the X-ray intensity displays tails expanding in real space to around  $4 \mu\text{m}$  along the vertical directions: the main maximum in the center of the beam and four to five side

maxima. Interaction of these maxima with the highly bent crystal structures will be discussed later during the explanation of the RSMs presented in Figure 2.3.

## 2.4 Micro-focus X-ray diffraction data

In this section the recorded RSMs from NW1 and NW2 are presented and discussed; the individual RSMs from NW3 and NW4 are presented in the supplementary material.

Figure 2.3 shows the strategy of mapping the NW's GaAs 111 Bragg reflection at beamline ID01 for sample 1. The NW is scanned by the X-ray beam at different positions along the growth axis [see Figure 2.3a]. At each position a 3D RSM is recorded. In the case of position 1, the  $q_{(x,y)}$  slice taken from the 3D RSM at the main maximum shows thickness fringes along the  $q_x$  direction corresponding to a size of around 112–127 nm [see Figure 2.3b) and Figure 2.1a]. This is in good agreement with the NW dimensions given in Section 2, from which a nominal distance between the upper and lower blue facets [see Figure 2.1a] of  $\sim 126$  nm is expected.

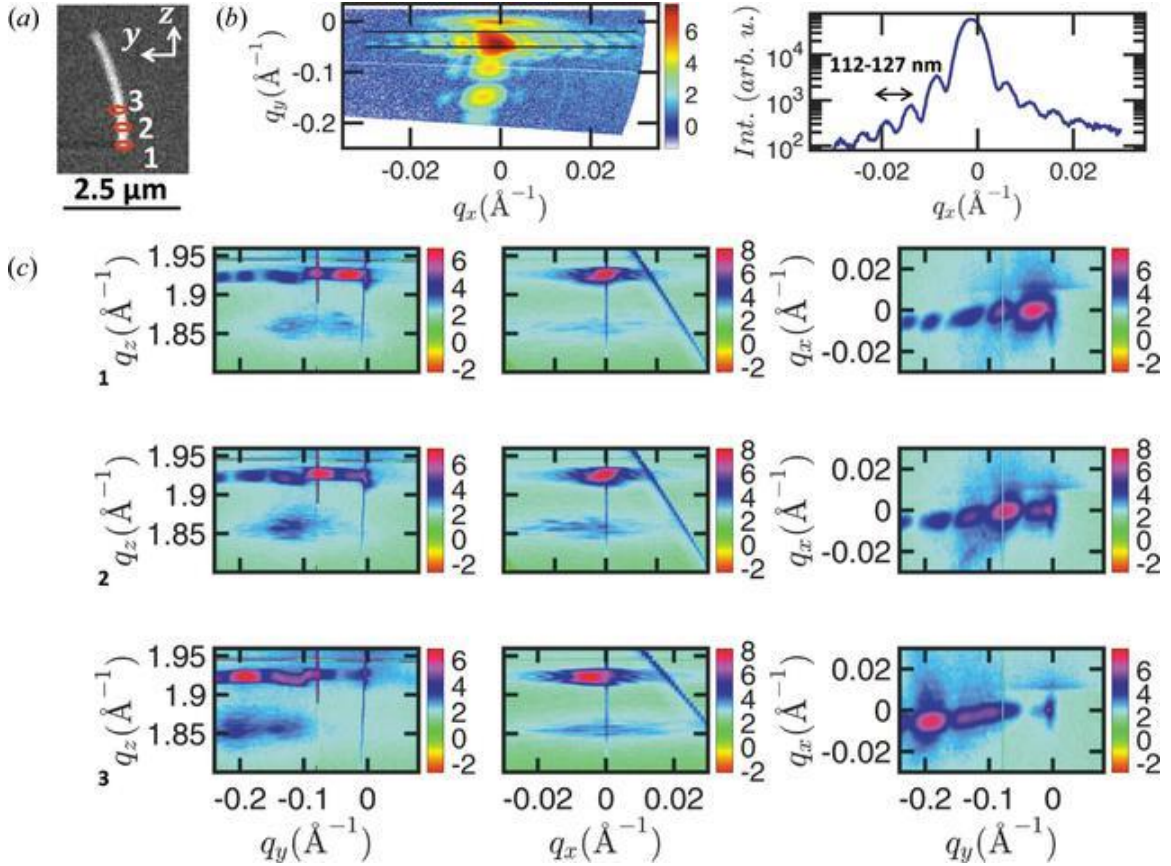


**Figure 2.3.** (a) SEM image of NW1 with the central X-ray beam position of measurements 1, 2 and 3 marked. (b)  $q(x,y)$  plane extracted from the 3D RSM at the GaAs 111 Bragg reflection recorded at position 1. The signal between the black lines is shown in the line plot on the right and exhibits thickness oscillations corresponding to a size of  $120 \pm 8$  nm. (c) 2D projections of 3D RSMs measured at the three different positions along the growth axis of NW1. For each position the  $q(z,y)$ ,  $q(z,x)$  and  $q(x,y)$  projections are shown by filled contour plots with a logarithmic intensity scale.

Examples of the projections of the 3D RSM onto the  $q(z,y)$ ,  $q(z,x)$  and  $q(x,y)$  planes are shown in Figure 2.3c for the different positions along the NW. As seen at the bottom part of the NW (position 1), the projection of the RSM onto the  $q(z,y)$  plane has a maximum at  $q_y = 0 \text{ \AA}^{-1}$ . Here we observe an envelope function with clear maxima and minima due

to the wavefront of the X-ray beam illuminating the NW along the vertical direction. The interaction of the (111) planes, with varying tilt in the NW, with the coherent focused X-ray beam leads to complex scattering and interference patterns originating from different locations on the NW. The resulting scattering pattern in Figure 2.3c1 for  $q_{(z,y)}$  and  $q_{(x,y)}$  projections can be explained in the following way: (1) The main maximum of the X-ray beam's wavefront is aligned with the bottom part of the NW, where the 111 planes are parallel to the substrate surface. From this the peak near  $q_y = 0 \text{ \AA}^{-1}$  results. (2) Parts of the NW further away from the substrate surface are illuminated by the side maxima (tails) of the X-ray beam, which are shown in Figure S1. Since the segments of the wire illuminated by the tails are tilted, side fringes of the illumination function cause minima at  $q_y \simeq -0.08 \text{ \AA}^{-1}$  and  $q_y \simeq -0.17 \text{ \AA}^{-1}$  as well as maxima at around  $q_y \simeq -0.1 \text{ \AA}^{-1}$  and  $q_y \simeq -0.2 \text{ \AA}^{-1}$ . These maxima originate roughly from positions 2 and 3 on the NW. This interpretation is corroborated by the patterns shown in Figure 2.3c2 and 2.3c3, which are recorded at positions 2 and 3 and have their corresponding main maximum near the side maxima observed in Figure 2.3c1. On the basis of the arguments above, the reconstructed wavefront of the X-ray beam can be used to retrieve the illumination position of the X-ray beam on the NW. For this purpose we use the known distance between the maxima of the wavefront in real space. Considering the experimental geometry, we recalculate this spacing as a distance along the NW growth axis. Accordingly, two neighboring maxima in the diffraction pattern originate from segments located around 250 nm apart from each other along the NW growth axis. Note that the distance determined in this way is significantly less affected by time drifts

as compared to RSMs recorded for different motor positions since both the different  $q$ -space position and the real-space position are obtained from the same measurement.

The bending radius of the NW crystal was calculated from the distance between two NW segments and their tilt angle, determined from the center of mass of maxima in the envelope function. In this way we obtain a bending radius of  $\sim 8\text{--}12\ \mu\text{m}$ . The large spread in values originates from the fact that the spacing of the fringes is not equal in Figure 2.3c. Note that an anomaly near  $q_y = -0.1\ \text{\AA}^{-1}$  consistently appears in the particular data shown in Figure 2.3c. This is probably the result of some major defect, which will locally also change the bending radius. While the radius determined by X-ray diffraction determines the local bending of the crystal, where the measurement was performed, the radius determined by SEM corresponds to an average bending radius of the NW shape. Nevertheless, a good agreement between these two values is found.

In the  $q_{(z,y)}$  plane shown Figure 2.3c, the diffraction signal seen around  $q_z \simeq 1.85\ \text{\AA}^{-1}$  corresponds to non-pseudomorphic defective shell material grown on the wire. This can be concluded from the evolution of the signal for different illumination positions seen in Figure 2.3c in the  $q_{(z,y)}$  and  $q_{(z,x)}$  projections. The width of the NW peak along the radial  $q$  direction is large and lies between the known peak positions of wurtzite and zinc-blende crystalline structures, which can be present in the NW at the same time.<sup>26</sup> This hinders our study of the NW in terms of crystalline phase distribution along the NW growth axis from these data.

Owing to the small beam size and strong bending, only part of the NW contributes in a single measurement. An RSM for the entire NW is obtained only by combination of several measurements like those shown in Figure 2.3. For this purpose, RSMs from many different real-space positions as well as for different angular positions have to be combined. In the case of NW1 and NW2, more than 36 000 individual 3D RSMs were analyzed and combined together. Projections of the resulting RSMs for NW1 and NW2 are shown in Figure 2.4*a* and 2.4*b*. Combining data recorded at different locations washes out the coherent diffraction patterns observed in Figure 2.3 because all the segments of the NW fulfill the Bragg condition individually during the RSM scanning. The result is the observation of diffraction signal distributed along a segment of a Debye ring, which will be discussed in more detail in Section 6. An anomaly in the signal near its termination in Figure 2.4*a* and 2.4*b* originates from diffraction of the very top part of the NW.

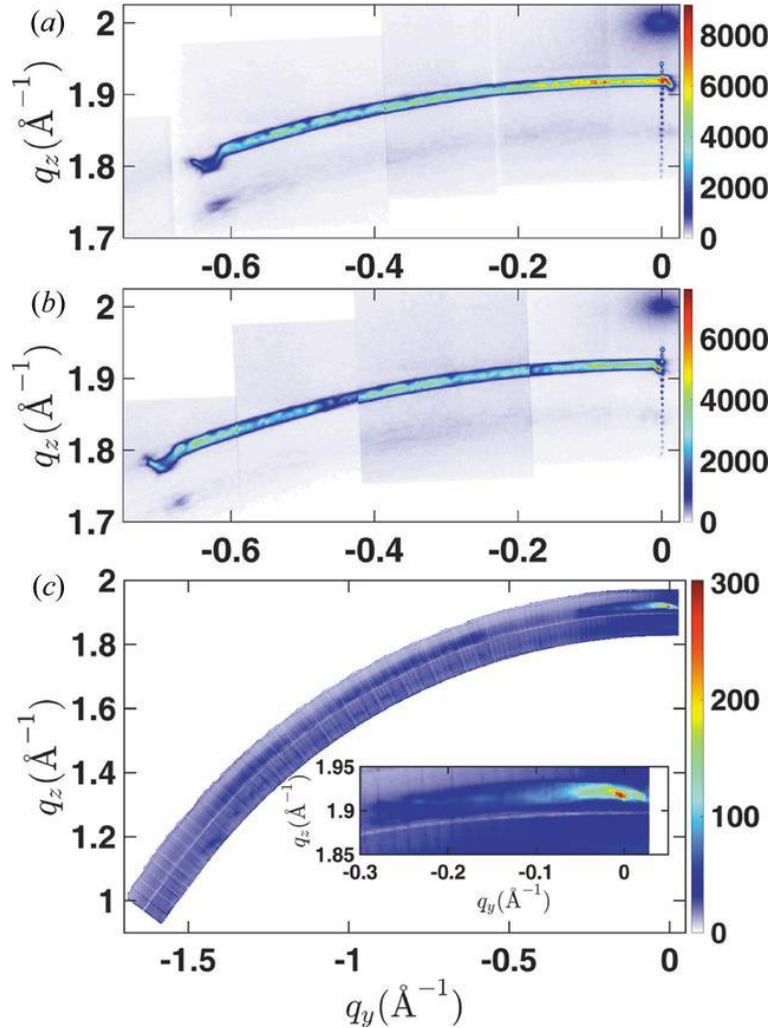


**Figure 2.4.** The projections of the combined RSMs for (a) NW1 and (b) NW2 of sample 1 and (c) NW3 of sample 2. The signal from the bent NWs spreads out along a segment of the Debye ring. An inset in panel (c) shows a magnification of the signal near  $q_y = 0$   $\text{\AA}^{-1}$ .

For NW3 and NW4 of sample 2, projections of individual RSM measurements are presented in FigureS2 in the supplementary material. In contrast to the data shown in Figure 2.3, the patterns show no diffraction speckles. This difference is likely to be

caused by a combination of multiple effects: First, the focal spot at beamline P23 used for these measurements was significantly larger and therefore the central maximum of the focal spot illuminates a considerable fraction of the NW. Second, NW3 and NW4 have much lower bending radii, which suggests that only a short segment of the NW can fulfill the Bragg condition within one reciprocal-space map. Third, while the beam at ID01 is highly coherent this is not the case for the beam used at P23. Forty-two RSMs of NW3 recorded for different sample tilts  $\chi$  were collected and combined to create the RSM shown in Figure 2.4c. At  $q_y = 0 \text{ \AA}^{-1}$  the Bragg peak of the GaAs 111 reflection is relatively sharp and intense. However, its intensity decreases while its FWHM along the radial  $q$  coordinate increases up to  $q_y = -0.09 \text{ \AA}^{-1}$ . The strong intensity near  $q_y = 0 \text{ \AA}^{-1}$  originates from the bottom part of the NW, which is less bent compared with parts further up. This lower bending results in a higher material volume which simultaneously satisfies the Bragg condition and therefore causes the strong signal.

In the range of  $-1.5 < q_y < -0.09 \text{ \AA}^{-1}$  the intensity variations are probably the result of slight misalignment of the beam position away from the NW. Owing to time limitations it was not possible to collect diffraction data from the full NW. Although hardly visible in Figure 2.4c, the signal extends beyond the measurement range. From the bending observed in the SEM images one would expect the signal to continue along the Debye circle until  $q_z \simeq 0 \text{ \AA}^{-1}$ .

In the measurements shown in Figure 2.4, the FWHM of the Bragg peak along the radial  $q$  coordinate is related to the different lattice plane spacings inside the GaAs NW core, *i.e.* the strain variation in the NW. As we show later, it is therefore inversely

proportional to the bending radius. The widening of the diffraction signal at lower  $q_y$  values in Figure 2.4c could be related to a variation of the local bending radius. This will be discussed in more detail after we introduce a theoretical approach which allows us to quantify the strain gradient/bending.

## 2.5 Transmission electron microscopy

In order to support the X-ray diffraction results, we performed high-resolution TEM investigations in cross-section geometry. For this purpose, a few NWs of samples 1 and 2 were scratched carefully from the silicon substrate and were deposited onto a lacy carbon support grid. The TEM analysis was performed by using an FEI Talos F200X operated with an acceleration voltage of 200 kV on selected NWs lying nearly flat on the support film, *i.e.* the bending plane was oriented perpendicular to the viewing direction.

Figure 2.5 shows examples of low- and high-resolution images of samples 1 and 2. In Figure 2.5a, stitched images of two complete NWs of sample 1 are shown. The upper NW has its bending plane parallel to the viewing direction and was therefore disregarded in the analysis. In contrast, the lower NW is lying flat on the support grid such that a bending radius of 8–9  $\mu\text{m}$  can be measured. For the NW of sample 2 shown in Figure 2.5b, we identify a change of the bending radius from  $\sim 3 \mu\text{m}$  on the left to  $\sim 2.3 \mu\text{m}$  on the right of the image. Note that the right-hand side corresponds to the top of the NW. Despite the fact that the NWs have been randomly scratched from the Si substrate, the bending radius found here agrees reasonably well with the radii that were found in the X-ray analysis.

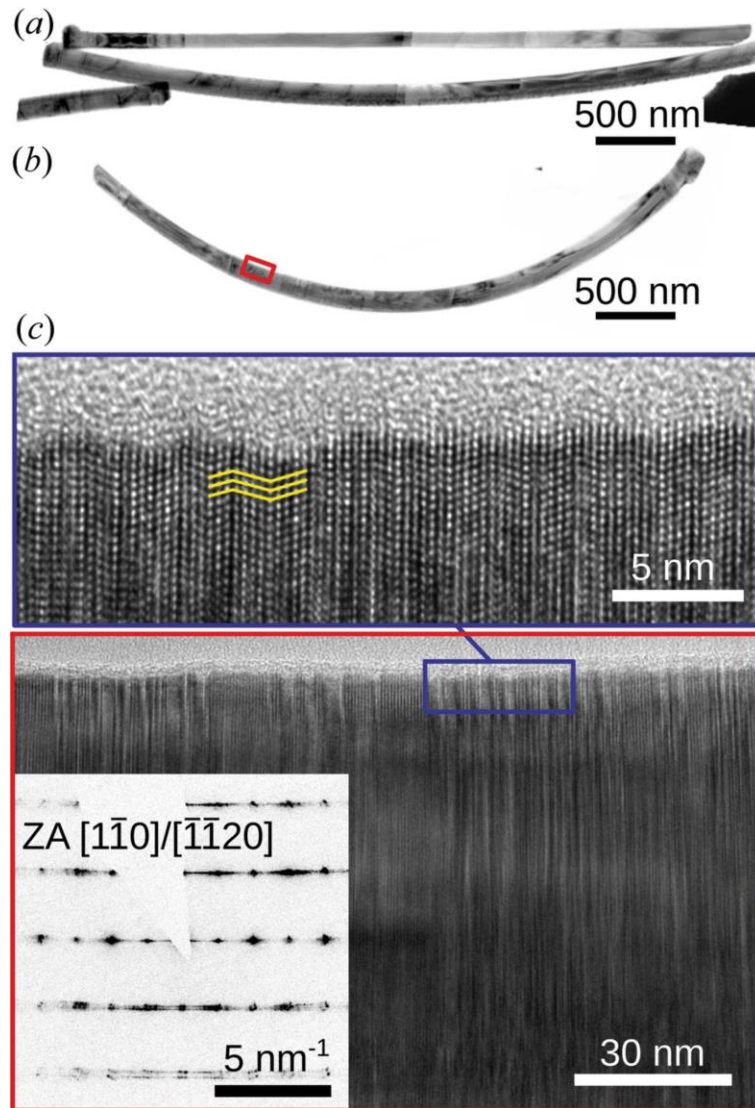


**Figure 2.5.** Transmission electron micrographs of NWs from sample 1 (a) and sample 2 (b). From nanowires that have their bending plane parallel to the imaging plane, the bending difference between the samples [cf. (a) and (b)] is evident. A high-resolution image of the region marked by the red rectangle in (b) is shown in (c). By further zooming in to the region marked by the blue rectangle, planar defects can be seen. In (c), the yellow lines highlight a twinned region. The inset in (c) shows an electron diffraction pattern recorded along the  $[1\bar{1}0]$  cubic or equivalent  $[\bar{1}\bar{1}20]$  hexagonal zone axis, respectively.

In addition to the bending, it is possible to identify local crystallographic and defect structure information on the NWs. For sample 1, all inspected NWs appear very homogeneous in the middle and bottom parts of the NW, with a very low density of planar defects. The region close to the top, just below the crystallized droplet, shows a sequence of fast changing ZB and WZ phase units. In contrast to this, NWs of sample 2 [Figure 2.5*b* and 2.5*c*] are highly defective in the lower half, while the upper part is almost defect free. This highly defective region has been found in nearly all inspected NWs but with different extent and position along the NW. The high number of defects in the defective part becomes obvious by the streaking of diffraction spots seen in the inset of Figure 2.5*c* and in Figure S3 in the supporting information. The images show that a large number of planar defects and phase changes are present in the sample. The NW shown in Figure 2.5*b* is mainly composed of the WZ phase. Other NWs of the same sample probed by TEM also show the ZB phase with a similar volume fraction of the defective region. About 20% of highly bent NWs did not show this defective region.

Figure S3 shows that, in agreement with the expectation from NW growth, the local [111] or [0001] crystal direction is always aligned with the NW axis. Since the determination of the bending radius from X-ray diffraction measurements presented above relies on the crystal orientation, it is important to obtain an independent proof of this aspect.

## 2.6 Diffraction theory of bent NWs

In this section we simulate diffraction RSMs of a bent NW. The aim of this simulation is to qualitatively demonstrate the influence of bending on the shape of the diffraction maximum. In addition to the kinematical approximation we make the following assumptions:

- (1) The far-field limit applies. The validity of this assumption is proven by the calculation of the phase factor of the Fresnel propagator  $P_{Fres} = \exp[iKr^2/(2L)]$ , where  $K = 2\pi/\lambda$  is the wavevector length and  $L$  is the sample–detector distance. In our experimental arrangement, the exponential term of this propagator is smaller than  $10^{-4}$ .
- (2) The NW is ideally circularly bent and its circular axis lies in the  $yz$  plane perpendicular to the sample surface. This assumption makes the simulation much easier: the differences between the actual and circular NW shapes could affect the tails of the diffraction maximum. The incident X-ray beam lies in the  $xz$  plane and we calculate the reciprocal-space distribution of the diffracted radiation (reciprocal-space map) in plane  $q_y q_z$  parallel to  $yz$ .
- (3) The NW cross section is circular. Possible facets on the NW sidewalls would create streaks, which, however, are not visible in the  $q_y q_z$  reciprocal plane.
- (4) The elementary unit cells of the NW structure are not deformed by bending, *i.e.* the structure factors of individual reflections are not affected by bending either. A modification of the structure factor by bending leads to a change in the diffracted

intensity; however, the shape of the diffraction maximum in reciprocal space is not affected by this simplification.

We denote by  $R$  the bending radius and  $\varrho$  the radius of the wire cross section. The position vector of an elementary unit cell is

$$r_b = [x, R - (R - y) \cos(\chi), (R - y) \sin(\chi)], \chi = z/R, \quad (2.1)$$

where  $r = (x, y, z) = n_1 a_1 + n_2 a_2 + n_3 a_3$  is the position vector of the same cell in a non-bent NW,  $a_{1,2,3}$  are the basis vectors and  $n_{1,2,3}$  are integers. Furthermore, we denote by  $\Omega(r)$  the shape function of the non-deformed NW (unity inside the NW volume and zero outside of it).

Under the assumption above, the wave scattered into the point  $q = K_f - K_i$  of reciprocal space is ( $K_{i,f}$  are the wavevectors of the primary and scattered beams)

$$E(q) = A \sum_g F_g \int d^3r \Omega(r) E_{inc}(z) \exp\{-i[q \cdot r_b(r) - g \cdot r]\} \equiv A \sum_g F_g \Psi_g(q). \quad (2.2)$$

Here  $A$  is an uninteresting factor very slightly dependent on  $q$ ,  $g$  are the vectors of the lattice reciprocal to the non-deformed NW lattice,  $F_g$  is the structure factor of reflection  $g$ , and  $E_{inc}(z)$  is the amplitude of the incident wave. We assume that this amplitude depends only on the vertical coordinate  $z$  and the cross-section profile of the incident beam is Gaussian:

$$E_{inc} = \exp\left[-\frac{(z-z_0)^2}{2\sigma^2}\right]. \quad (2.3)$$

The FWHM of the incoming beam along the  $z$  axis is proportional to the parameter  $\sigma$ :  $\text{FWHM} = 2\sigma(2 \log 2)^{1/2}$ .

The integrals in the amplitudes  $\Psi_g(q)$  can be partially evaluated and we obtain

$$\Psi_g(q) = \pi q^2 \int_{-\infty}^{\infty} dz E_{inc}(z) B \left\{ q \left[ (g_y - q_p)^2 + g_z^2 \right]^{1/2} \right\} \times \exp\{-i[(q_y - q_p)R - g_z]\}, \quad (2.4)$$

where

$$q_p = q_y \cos(\chi) - q_z \sin(\chi), \quad B = 2J_1(x)/x, \quad (2.5)$$

with  $J_1(x)$  the Bessel function of first order. The remaining integral over  $z$  has to be evaluated numerically. In order to avoid numerical complications at the NW ends we assume that the NW is much longer than the irradiated footprint determined by  $E_{inc}(z)$ . Therefore the integration limits can be expanded to  $\pm\infty$ .

For a rough estimation of the diffraction maximum position in the  $q_y q_z$  plane we can approximate the integral in equation (2.2) by the stationary phase method; in this approach we ignore the  $x$  integration and calculate the integral only in the  $yz$  plane. The stationary points of the phase

$$q_p = q_y \cos(\chi) - q_z \sin(\chi), \quad B = 2J_1(x)/x \quad (2.6)$$

are

$$y_{1,2}^{(0)} = R \frac{(q^2 - g_y^2)^{1/2} \mp g_z}{(q^2 - g_y^2)^{1/2}}, \quad z_{1,2}^{(0)} = R \left[ \frac{q_y (q^2 - g_y^2)^{1/2} \mp g_z q_z}{g_y q_y \pm q_z (q^2 - g_y^2)^{1/2}} \right]. \quad (2.7)$$

Furthermore, we define the Hessian of the phase function  $\phi(r)$  and calculate its determinant in the stationary points. Both points yield the same value:

$$H = (g_y^2 - q^2)/R^2 \quad (2.8)$$

The stationary phase approximation of the integral  $\Psi_g(q)$  is then

$$\begin{aligned} \Psi_g(q) \simeq \sum_{j=1,2} \Omega(y_j^{(0)}) E_{inc}(z_j^0) \exp[i\phi(y_j^{(0)} - z_j^{(0)})] \times \\ 2\pi R |g^2 - q^2|^{-1/2} \exp[i\pi \text{sign}(H)/4]. \end{aligned} \quad (2.9)$$

This formula allows us to estimate the position  $q_{max}$  of the diffraction maximum in the  $q_y q_z$  plane. The maximum occurs at the point at which  $y_{1,2}^{(0)} = 0$  and  $z_{1,2}^{(0)} = z_0$ . This condition yields an obvious result, namely the angle between the vectors  $g$  and  $q_{max}$  equals  $\chi$ .

The maxima of the integrals  $\Psi_g(q)$  for different  $g$  almost do not overlap, so that we can neglect the sum  $\sum_g$  in equation (2.2), writing

$$E(q) \simeq A F_h \Psi_h(q). \quad (2.10)$$

Here  $\mathbf{h}$  denotes the reciprocal-lattice vector lying closest to  $q$ .

In Figure 2.6, 2.7 and 2.8 we present examples of the results of numerical simulations. In Figure 2.6 and in panels (a), (c) and (e) of Figure 2.7 we consider an NW with a radius of  $\varrho = 40$  nm and a bending radius  $R = 1$   $\mu\text{m}$ . The width parameter of the incident beam was chosen to be  $\sigma = 60$  nm so that the FWHM of the beam was 100 nm. Panels (b), (d) and (f) of Figure 2.7 show the calculated maps for  $R = 2$   $\mu\text{m}$ ,  $\varrho = 60$  nm and FWHM = 200 nm. In Figure 2.6, the end points of  $h$  and  $h_B$  are displayed as filled and empty circles; the diffraction maximum indeed lies at  $q = h_B$ . The figure demonstrates that for a qualitative estimate of the maximum position and shape the simple stationary phase calculation is fully sufficient. The diffraction maxima are arc shaped, elongated in the direction perpendicular to the diffraction vector  $h_B$ , and rotate by an angle  $\chi$  with respect to  $h$  as a result of bending. The arc length and width are inversely proportional to the bending radius  $R_B$  [compare the panels (a) and (b) in Figure 2.7]; the arc length is proportional to the FWHM of the primary beam, *i.e.* to the length of the irradiated NW segment [panels (a) and (f)].

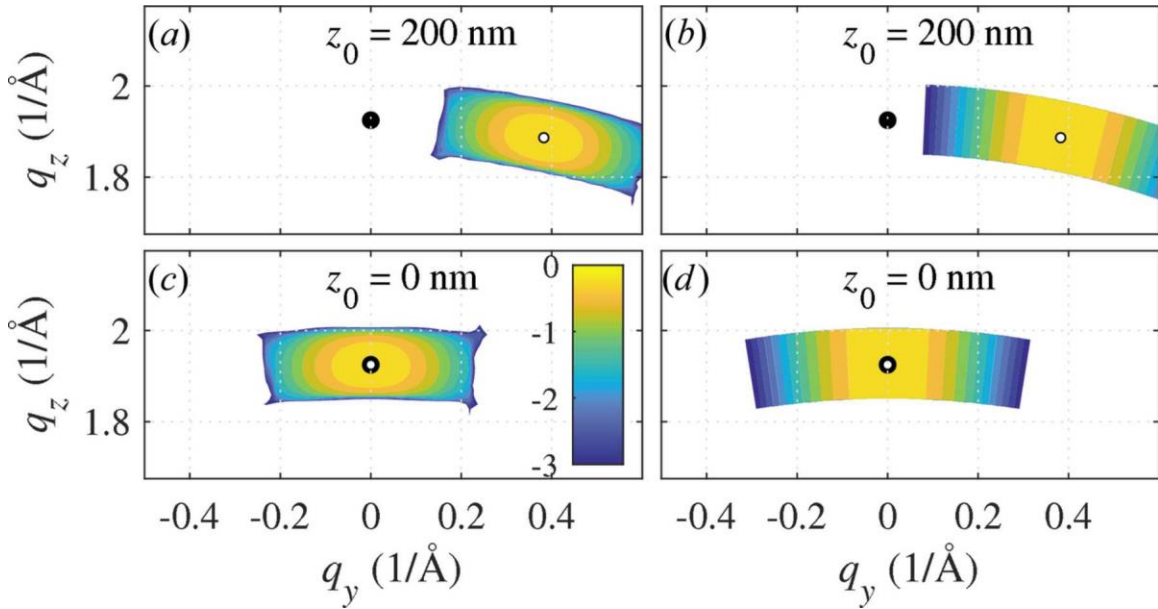


**Figure 2.6.** The reciprocal-space maps calculated for symmetrical diffraction  $\mathbf{h} = (111)$  using the exact kinematical formula (2.2) [panels (a) and (c)] and the stationary-phase method in equation (2.7) [(b) and (d)] for various positions  $z_0$  of the primary beam (parameters of the graphs). The filled and empty circles denote the end points of the non-rotated reciprocal-lattice vector  $\mathbf{h}$  and the rotated vector  $\mathbf{h}_B$ , respectively. The intensity is displayed logarithmically. Color bar ticks are labeled with the decadic exponents of the intensity relative to the intensity maximum.

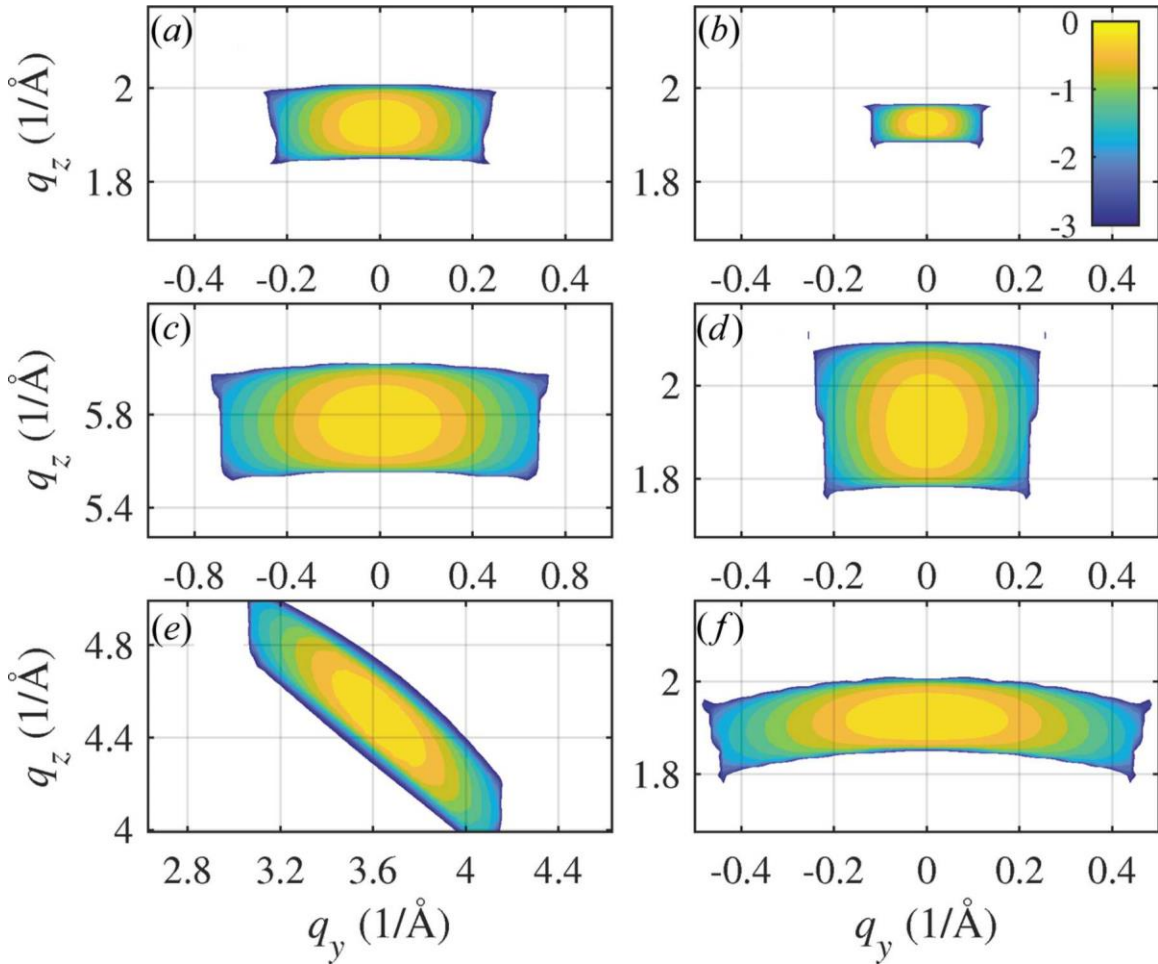


**Figure 2.7.** The reciprocal-space maps calculated using equation (2.2) for  $\mathbf{h} = (111)$  [panels (a), (b), (d) and (f)],  $\mathbf{h} = (333)$  (c) and  $\mathbf{h} = (115)$  (e). In (b) the simulation was carried out for two times larger bending radius, panel (d) shows the map calculated for two times larger NW radius, and in (f) the map shows the data for two times larger FWHM of the primary beam. The intensity is displayed logarithmically. Color bar ticks are labeled with the decadic exponents of the intensity relative to the intensity maximum.

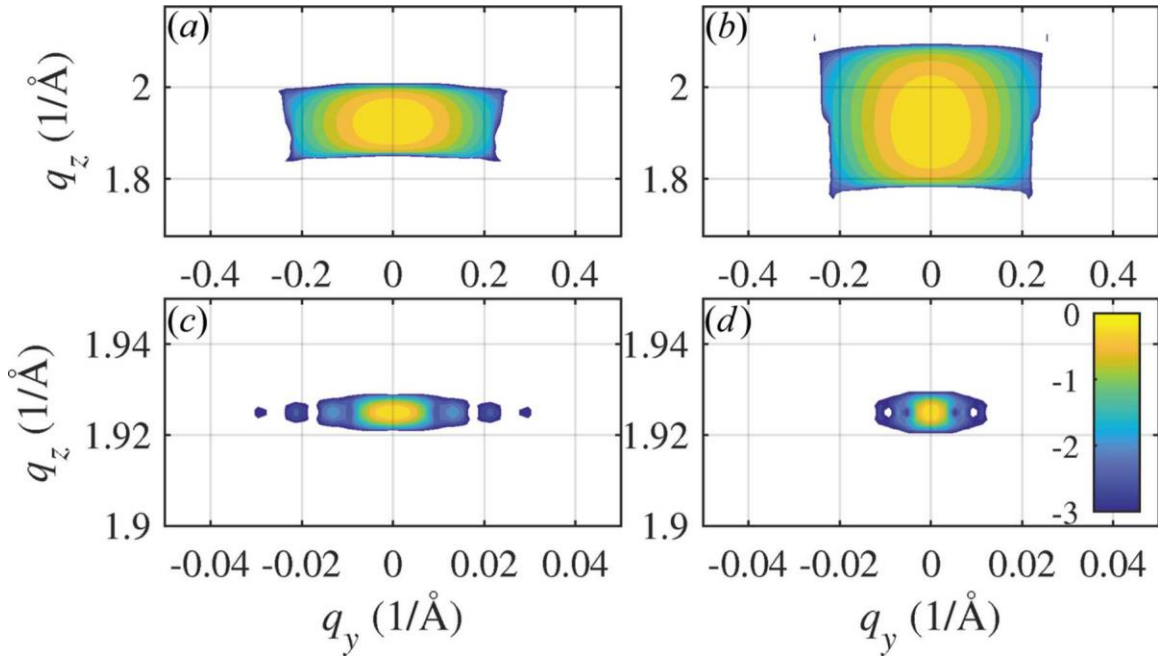


**Figure 2.8.** The  $(111)$  reciprocal-space maps calculated for small and large NW radii and strong bending ( $R = 1 \mu\text{m}$ ) in (a) and (b), and for the same NW radii and slight bending ( $R = 100 \mu\text{m}$ ) in (c) and (d). The intensity is displayed logarithmically. Color bar ticks are labeled with the decadic exponents of the intensity relative to the intensity maximum.

Interestingly, the width of the arc is proportional to the NW radius  $\rho$  [Figure 2.7a and 2.7d]. This counter-intuitive behavior demonstrates that the size of the diffraction maximum is determined mainly by strain and not by the size of the irradiated NW volume. This effect is demonstrated in Figure 2.8, where we compare reciprocal-space maps calculated for  $\mathbf{h} = (111)$  for two NW radii ( $\rho = 40$  and  $80$  nm) and strong bending  $R = 1 \mu\text{m}$  [panels (a) and (b)] and slight bending  $R = 100 \mu\text{m}$  [panels (c) and (d)]. While in the case of strong bending the arc width is proportional to  $\rho$ , in the case of

slight bending the arc length is inversely proportional to  $\rho$ , and the arc width is inversely proportional to the beam FWHM.

The arc width  $\delta q_z$  can be used for an easy determination of the bending radius  $R$ . This is demonstrated in Figure 2.9, where we have plotted the inverse bending radius  $1/R$  as a function of  $\delta q_z$  determined by numerical calculation of the 111 Bragg spot using equation (2.2) (points). The dependence is almost linear; the straight lines in the figure show the linear approximation of the  $1/R$  versus  $\delta q_z$  dependence. The slope of this dependence decreases with increasing NW radius  $\rho$ .

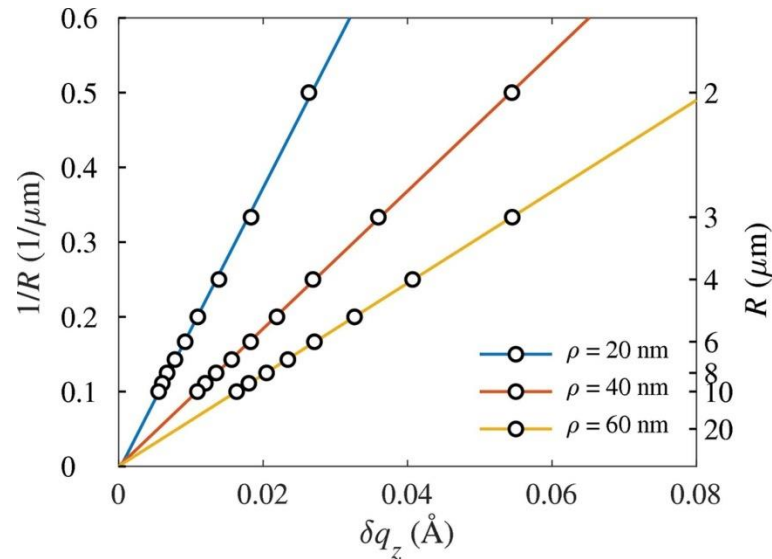


**Figure 2.9.** The linear dependence of the reciprocal bending radius on the width of the 111 diffraction maximum in the  $q_z$  direction calculated for various NW radii (parameters of the curves). The circles represent the data obtained by calculation using equation (2.2); the lines are their linear fits.

## 2.7 Results and discussion

Using the measured data presented above as well as the theory introduced in the previous section, we will further process the experimental data and compare them with simulations to assess the strain state of the nanowires.

For this purpose, we replot the experimental data from Figure 2.4 using the radial coordinate  $q_r = |\mathbf{q}|$  and the tilt angle  $\chi$  as coordinates in Figure 2.10. It can be seen that in the case of NW1 and NW2 of sample 1 with higher bending radius the signal extends up to  $\chi \approx 20$  and  $22^\circ$ , respectively. Around  $\chi = 18^\circ$  for NW1 and  $\chi = 21^\circ$  for NW2 a sudden change is detected in the RSM, which we associate with the top segment of the NW. This segment is likely to have a different chemical composition, since it might originate from axial wire growth during the shell growth, similarly found by AlHassan *et al.*<sup>27</sup> In Figure 2.10c showing data of NW3 of sample 2 no such anomaly from the top of the wire is observed, since the top part according to the SEM images is tilted almost  $90^\circ$  far beyond the end of the measurement range. As concluded from the simulations, the different tilt range of the signal in Figure 2.10a and 2.10b could be a result of differences in either the bending radii or the lengths of the NWs. Since the lengths determined from the SEM images shown in Figure 2.1a are rather similar, the likely explanation is that the bending radii of these wires are slightly different. A close inspection of the SEM images in agreement with the higher tilt range of NW2 seen in Figure 2.10b suggests that the top of NW2 is more bent as compared with NW1.

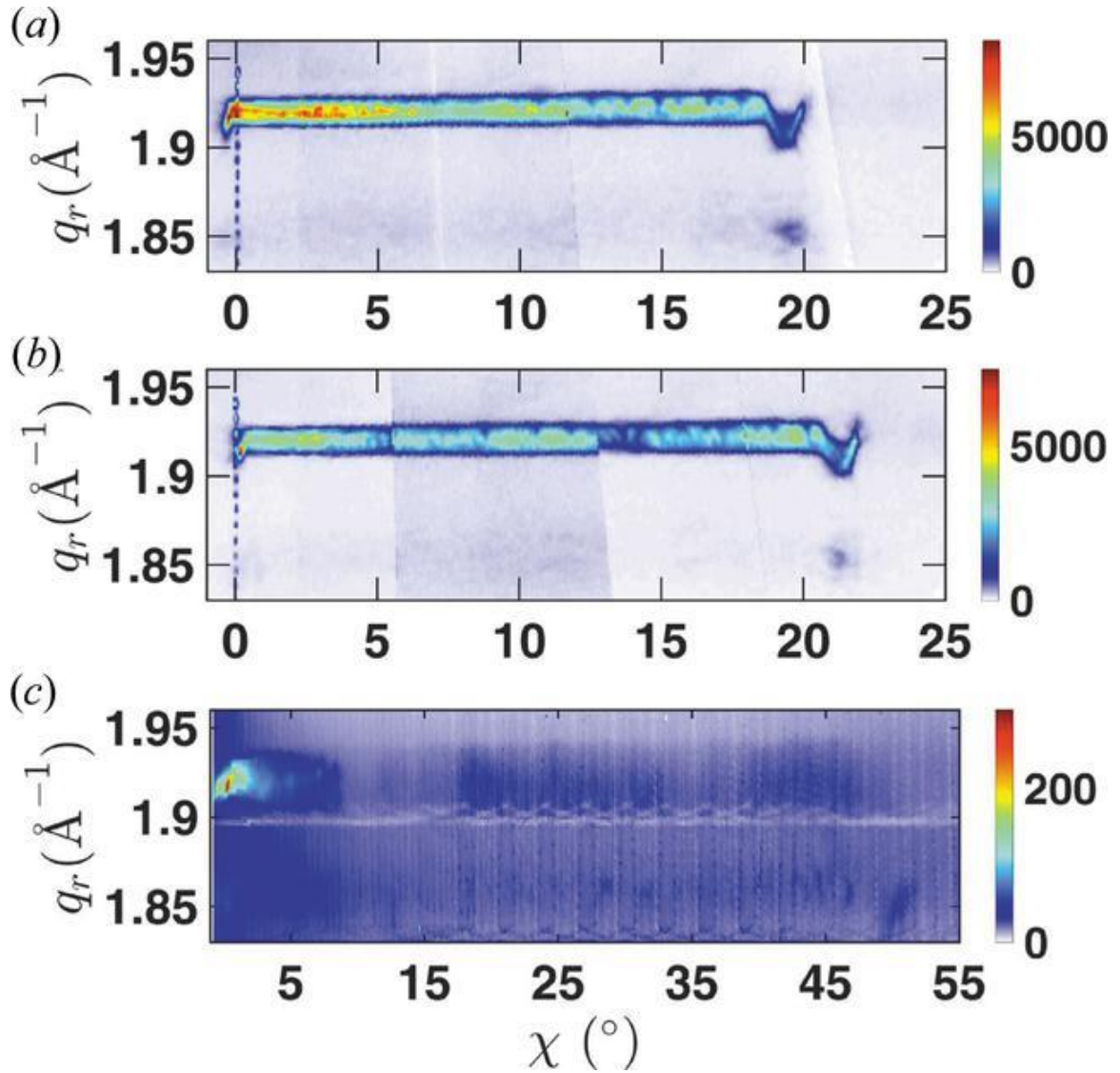


**Figure 2.10.** Radial integration of the combined RSMs of (a) NW1 and (b) NW2 of sample 1 and (c) NW3 of sample 2. Data are plotted versus the angle  $\chi$  which specifies the tilt with respect to the substrate surface.

To further compare the diffraction signal of the NWs, we obtain line cuts along the radial direction averaged over different ranges of tilt  $\chi$  and compare them in Figure 2.11. In

agreement with the expectations from our model calculations, the higher bending radius of NW1 and NW2 of sample 1 causes their signal to be considerably narrower than that of NW3 of sample 2. Another observation is that the width of the curves gets slightly wider when it is extracted from higher tilt values. This means that the bending radius is not entirely homogeneous along the NW axis. Considering that the base of the NW is fixed epitaxially to a rigid support, it makes sense that the bending at the bottom needs to develop and can reach its highest values only a certain distance away from the wire–substrate interface. Since the deposition geometry also gets highly complicated and evolves during growth, one also expects an inhomogeneity in the shell thickness along the NW growth axis. Both effects support a change of the bending for different positions along the NW.

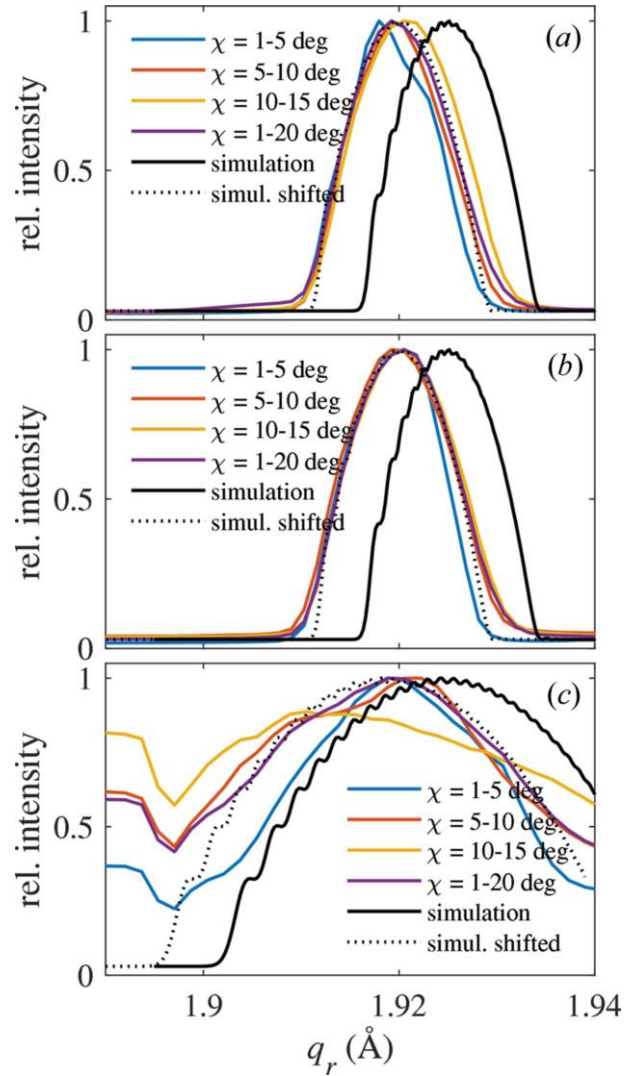


**Figure 2.11.** Comparison of experimentally measured intensity profiles (color lines) along the  $q_r$  direction with respect to calculation based on bent circular NWs (full and dotted black lines). Panels (a), (b) and (c) show data for NW1 and NW2 of sample 1 and NW3 of sample 2, respectively. Various tilt integration ranges indicated in the figure legend were used to obtain these curves from data shown in Figure 2.10.

In order to understand the contribution of the individual effects, we performed simplified model calculations of the shell growth process as described by Lewis *et al.*<sup>8</sup> Since the deposition rate on the NW sidewall is related to the angle between the sidewall and the incident flux, the deposition rate changes as the NW bends and also varies along the

length of a bent NW. The predicted shell thickness and local bending radius along the NW were calculated using an iterative approach, approximating the NW core to have a circular cross section. In this model, the 40 nm thickness (planar deposition) was divided into 100 deposition steps and the NW was divided into segments of 25 nm length, each having a constant deposition rate. For each deposition step, the local deposition was calculated (taking bending into account) and the curvature of the segment was calculated using the analytic model of Lewis *et al.*<sup>8</sup> For sample 1, since the lattice mismatch for the 5 nm GaAs and 10 nm GaAs/Al<sub>0.3</sub>Ga<sub>0.7</sub>As components is negligible and the InAs sub-shell of 2 nm is very thin, we combine all these shells and assume a GaAs core of 111 nm thickness for the simulations. The calculations predict that the shell thickness increases significantly from 27 nm at the base to 45 nm near the top of the bent NW, and the bending radius varies from 3080 nm at the base to 2980 nm near the top. For sample 2, the shell thickness also varies from 27 nm at the base to 45 nm near the top, and the local bending radius varies from 1990 nm at the base to 2080 nm near the top. We note that the predicted radius for both samples is significantly smaller than what is observed experimentally. This could be either due to an overestimation of the shell thickness or because the shell growth is considered to be pseudomorphic. Plastic relaxation is, however, present at the core-shell interface as we observed the diffraction signal of the shell with a different lattice parameter in Figure 2.3. Nevertheless, the model confirms that an inhomogeneous shell thickness causes a slight variation of the bending radius leading to higher bending near the top, qualitatively in agreement with our experimental

observations. We note that reducing the asymmetric shell thickness in the model increases both the average bending radius and the variation in radius along the NW.

In order to assess the strain state of the NW core we look at the comparison of the experimental data with X-ray diffraction simulations. We showed in the theory section that the width of the diffraction signal for purely elastic bending and our experimental parameters can be associated with the bending. For the simulation curves shown in Figure 2.11 we used the nominal NW thickness, which was found to agree well with the thickness fringes observed in our RSMs. Again we approximate the entire core and symmetric shell structure of sample 1 as a GaAs core. Having fixed the NW geometry the only relevant parameter which remains is the NW bending radius. For the simulation curves for sample 1 [Figure 2.11*a* and 2.11*b*] we find that a radius of  $11.0 \pm 0.5 \mu\text{m}$  explains the observed width of the diffraction curves well. The radius is in good agreement with that determined earlier and that seen in the scanning electron microscope images. This suggests that the deformation of the NW core is indeed fully elastic without signs of plastic deformation inside the core.

In order to find an agreement for the peak position we had to shift the diffraction curve by approximately  $0.005 \text{ \AA}^{-1}$  towards smaller  $q$  values. The reason for this could be twofold. Either a small amount of WZ phase mixed into the NW or the asymmetric placement of the shell with larger lattice parameter can explain this. Since the partially grown shell causes tensile strain of the NW on the side it is attached to, which has no counterpart on the opposing side, the overall strain in the NW is more tensile. This means that the average lattice parameter in the NW is slightly larger than that of bulk GaAs used

in the simulation. If all the shift of the diffraction curve in Figure 2.11 corresponds to a change of the average lattice parameter it would amount to  $0.014 \text{ \AA}$ . For the bimetallic strip scenario mentioned in the Introduction this scenario is consistent with the neutral line, i.e. the unstrained part of the core material, being located towards the far side of the partial shell. Overall this causes the peak of the NW to move slightly towards lower  $q$  values. Since in our simulations the neutral line is located in the center of the NW we have to mimic this offset by shifting the diffraction curve. Because we know from TEM investigations that some WZ phase might be present, it is likely that a combination of the two effects (WZ inclusion and asymmetric strain) determines the resulting shift of the diffraction peak.

For NW3 of sample 2 a bending radius of  $3 \mu\text{m}$  leads to rough agreement between the calculated line profile and the experimental observations averaged over the full measured tilt range [Figure 2.11c]. It can, however, be clearly seen that the experimental curves for tilt ranges corresponding to segments of the NW closer to the substrate interface are significantly narrower and therefore less bent, corresponding to a bending radius almost  $1 \mu\text{m}$  larger. This suggests that the different bending radii seen in different parts of the TEM images indeed reflect an intrinsic variation of the bending radius within the NWs. The growth modeling, however, predicts only a much smaller variation of the bending radius due to the inhomogeneous shell thickness. Therefore, we speculate that in this sample not only the shell thickness but also the degree of plastic relaxation might change along the NW, potentially leading to a stronger change of the bending.

The bending radius determined from the peak width can also be converted to a change of strain from the facet in contact with the partial shell to the opposite side. For purely elastic bending this difference in strain is trivially given by  $2\rho/R$ , which is  $\sim 0.9\%$  in NW1 and NW2 and  $\sim 2.5\%$  in NW3. Such high uniaxial strain values can otherwise only be produced by the method of strain redistribution in micro-bridges which are lithographically produced out of thin films.

## 2.8 Conclusion

We have demonstrated measurement strategies and analysis of X-ray diffraction data for highly bent NWs in their as-grown geometry with micro-focus X-ray diffraction. By extending the kinematical X-ray scattering theory for circularly bent crystal structures, we performed model calculations and reached good agreement with experimental data. By comparing simulations with our experimental data we obtain the bending radii of individual NWs. Our results further provide insights into the homogeneity of the bending of the NWs along their growth axis and allow us to directly access the amount of strain in the NW core material. We have shown that the bottom part of the NWs can have significantly lower bending/strain. Model calculations suggest that this can be related to an inhomogeneous shell thickness along the NW. The amount of uniaxial strain present in the NWs is comparable to the highest strains reported in micro-bridges but is present directly in the as-grown state.

## **Supporting Information**

Supporting information is provided by Journal of Applied Crystallography free of charge at <https://doi.org/10.1107/S1600576720011516/to5214sup1.pdf> or provided in appendix.

## References

- (1) Larsson, M. W.; Wagner, J. B.; Wallin, M.; Håkansson, P.; Fröberg, L. E.; Samuelson, L.; Wallenberg, L. R. Strain Mapping in Free-Standing Heterostructured Wurtzite InAs/InP Nanowires. *Nanotechnology* 2007, 18 (1). <https://doi.org/10.1088/0957-4484/18/1/015504>.
- (2) Johansson, J.; Dick, K. A. Recent Advances in Semiconductor Nanowire Heterostructures. *CrystEngComm* 2011, 13 (24), 7175–7184. <https://doi.org/10.1039/c1ce05821e>.
- (3) Hilse, M.; Takagaki, Y.; Herfort, J.; Ramsteiner, M.; Herrmann, C.; Breuer, S.; Geelhaar, L.; Riechert, H. Ferromagnet-Semiconductor Nanowire Coaxial Heterostructures Grown by Molecular-Beam Epitaxy. *Appl Phys Lett* 2009, 95 (13). <https://doi.org/10.1063/1.3240405>.
- (4) Caroff, P.; Wagner, J. B.; Dick, K. A.; Nilsson, H. A.; Jeppsson, M.; Deppert, K.; Samuelson, L.; Wallenberg, L. R.; Wernersson, L. E. High-Quality InAs/InSb Nanowire Heterostructures Grown by Metal-Organic Vapor-Phase Epitaxy. *Small* 2008, 4 (7), 878–882. <https://doi.org/10.1002/sml.200700892>.
- (5) Lehmann, S.; Jacobsson, D.; Dick, K. A. Crystal Phase Control in GaAs Nanowires: Opposing Trends in the Ga- and As-Limited Growth Regimes. *Nanotechnology* 2015, 26 (30). <https://doi.org/10.1088/0957-4484/26/30/301001>.
- (6) Tomioka, K.; Kobayashi, Y.; Motohisa, J.; Hara, S.; Fukui, T. Selective-Area Growth of Vertically Aligned GaAs and GaAs/AlGaAs Core-Shell Nanowires on

- Si(111) Substrate. *Nanotechnology* 2009, 20 (14). <https://doi.org/10.1088/0957-4484/20/14/145302>.
- (7) Alhassan, A.; Lähnemann, J.; Leake, S.; Küpers, H.; Niehle, M.; Bahrami, D.; Bertram, F.; Lewis, R. B.; Davtyan, A.; Schüllli, T. U.; Geelhaar, L.; Pietsch, U. Spatially-Resolved Luminescence and Crystal Structure of Single Core-Shell Nanowires Measured in the as-Grown Geometry. *Nanotechnology* 2020, 31 (21). <https://doi.org/10.1088/1361-6528/ab7590>.
- (8) Lewis, R. B.; Corfdir, P.; Küpers, H.; Flissikowski, T.; Brandt, O.; Geelhaar, L. Nanowires Bending over Backward from Strain Partitioning in Asymmetric Core-Shell Heterostructures. *Nano Lett* 2018, 18 (4), 2343–2350. <https://doi.org/10.1021/acs.nanolett.7b05221>.
- (9) Süess, M. J.; Geiger, R.; Minamisawa, R. A.; Schiefler, G.; Frigerio, J.; Chrastina, D.; Isella, G.; Spolenak, R.; Faist, J.; Sigg, H. Analysis of Enhanced Light Emission from Highly Strained Germanium Microbridges. *Nat Photonics* 2013, 7 (6), 466–472. <https://doi.org/10.1038/nphoton.2013.67>.
- (10) Gassenq, A.; Guilloy, K.; Osvaldo Dias, G.; Pauc, N.; Rouchon, D.; Hartmann, J. M.; Widiez, J.; Tardif, S.; Rieutord, F.; Escalante, J.; Duchemin, I.; Niquet, Y. M.; Geiger, R.; Zabel, T.; Sigg, H.; Faist, J.; Chelnokov, A.; Reboud, V.; Calvo, V. 1.9% Bi-Axial Tensile Strain in Thick Germanium Suspended Membranes Fabricated in Optical Germanium-on-Insulator Substrates for Laser Applications. *Appl Phys Lett* 2015, 107 (19). <https://doi.org/10.1063/1.4935590>.

- (11) Etzelstorfer, T.; Süess, M. J.; Schiefler, G. L.; Jacques, V. L. R.; Carbone, D.; Chrastina, D.; Isella, G.; Spolenak, R.; Stangl, J.; Sigg, H.; Diaz, A. Scanning X-Ray Strain Microscopy of Inhomogeneously Strained Ge Micro-Bridges. *J Synchrotron Radiat* 2014, 21 (1), 111–118.  
<https://doi.org/10.1107/S1600577513025459>.
- (12) Sukhdeo, D. S.; Nam, D.; Kang, J.-H.; Brongersma, M. L.; Saraswat, K. C. Direct Bandgap Germanium-on-Silicon Inferred from 57%  $\langle 100 \rangle$  Uniaxial Tensile Strain [Invited]. *Photonics Res* 2014, 2 (3), A8.  
<https://doi.org/10.1364/prj.2.0000a8>.
- (13) Balaghi, L.; Bussone, G.; Grifone, R.; Hübner, R.; Grenzer, J.; Ghorbani-Asl, M.; Krasheninnikov, A. V.; Schneider, H.; Helm, M.; Dimakis, E. Widely Tunable GaAs Bandgap via Strain Engineering in Core/Shell Nanowires with Large Lattice Mismatch. *Nat Commun* 2019, 10 (1), 1–10. <https://doi.org/10.1038/s41467-019-10654-7>.
- (14) Yudin, P. V.; Ahluwalia, R.; Tagantsev, A. K. Upper Bounds for Flexoelectric Coefficients in Ferroelectrics. *Appl Phys Lett* 2014, 104 (8).  
<https://doi.org/10.1063/1.4865208>.
- (15) Diaz, A.; Mocuta, C.; Stangl, J.; Mandl, B.; David, C.; Vila-Comamala, J.; Chamard, V.; Metzger, T. H.; Bauer, G. Coherent Diffraction Imaging of a Single Epitaxial InAs Nanowire Using a Focused X-Ray Beam. *Phys Rev B Condens Matter Mater Phys* 2009, 79 (12). <https://doi.org/10.1103/PhysRevB.79.125324>.

- (16) Robinson, I.; Harder, R. Coherent X-Ray Diffraction Imaging of Strain at the Nanoscale. *Nature Materials*. Nature Publishing Group 2009, pp 291–298.  
<https://doi.org/10.1038/nmat2400>.
- (17) Newton, M. C.; Leake, S. J.; Harder, R.; Robinson, I. K. Three-Dimensional Imaging of Strain in a Single ZnO Nanorod. *Nat Mater* 2010, 9 (2), 120–124.  
<https://doi.org/10.1038/nmat2607>.
- (18) Stankevič, T.; Hilner, E.; Seiboth, F.; Ciechonski, R.; Vescovi, G.; Kryliouk, O.; Johansson, U.; Samuelson, L.; Wellenreuther, G.; Falkenberg, G.; Feidenhans'l, R.; Mikkelsen, A. Fast Strain Mapping of Nanowire Light-Emitting Diodes Using Nanofocused X-Ray Beams. *ACS Nano* 2015, 9 (7), 6978–6984.  
<https://doi.org/10.1021/acsnano.5b01291>.
- (19) Keplinger, M.; Grifone, R.; Greil, J.; Kriegner, D.; Persson, J.; Lugstein, A.; Schüllli, T.; Stangl, J. Strain Distribution in Single, Suspended Germanium Nanowires Studied Using Nanofocused x-Rays. *Nanotechnology* 2016, 27 (5).  
<https://doi.org/10.1088/0957-4484/27/5/055705>.
- (20) Keplinger, M.; Kriegner, D.; Stangl, J.; Mårtensson, T.; Mandl, B.; Wintersberger, E.; Bauer, G. Core-Shell Nanowires: From the Ensemble to Single-Wire Characterization. *Nucl Instrum Methods Phys Res B* 2010, 268 (3–4), 316–319.  
<https://doi.org/10.1016/j.nimb.2009.09.043>.
- (21) Wallentin, J.; Jacobsson, D.; Osterhoff, M.; Borgström, M. T.; Salditt, T. Bending and Twisting Lattice Tilt in Strained Core-Shell Nanowires Revealed by

- Nanofocused X-Ray Diffraction. *Nano Lett* 2017, 17 (7), 4143–4150.  
<https://doi.org/10.1021/acs.nanolett.7b00918>.
- (22) Serrano, J.; Ferrero, C.; Servidori, M.; Härtwig, J.; Krisch, M. DuMond Analysis of Bending in Single Crystals by Laue Diffraction Using  $\sigma$ - $\pi$  Polarization Geometry. *J Appl Crystallogr* 2008, 41 (6), 1053–1056.  
<https://doi.org/10.1107/S0021889808029981>.
- (23) Kaganer, V. M.; Petrov, I.; Samoylova, L. X-Ray Diffraction from Strongly Bent Crystals and Spectroscopy of X-Ray Free-Electron Laser Pulses. *Acta Crystallogr A Found Adv* 2020, 76, 55–69. <https://doi.org/10.1107/S2053273319014347>.
- (24) Chahine, G. A.; Richard, M. I.; Homs-Regajo, R. A.; Tran-Caliste, T. N.; Carbone, D.; Jaques, V. L. R.; Grifone, R.; Boesecke, P.; Katzer, J.; Costina, I.; Djazouli, H.; Schroeder, T.; Schüllli, T. U. Imaging of Strain and Lattice Orientation by Quick Scanning X-Ray Microscopy Combined with Three-Dimensional Reciprocal Space Mapping. *J Appl Crystallogr* 2014, 47 (2), 762–769.  
<https://doi.org/10.1107/S1600576714004506>.
- (25) Mandula, O.; Elzo Aizarna, M.; Eymery, J.; Burghammer, M.; Favre-Nicolin, V. PyNX.Ptycho: A Computing Library for X-Ray Coherent Diffraction Imaging of Nanostructures. *J Appl Crystallogr* 2016, 49 (5), 1842–1848.  
<https://doi.org/10.1107/S1600576716012279>.
- (26) Jacobsson, D.; Yang, F.; Hillerich, K.; Lenrick, F.; Lehmann, S.; Kriegner, D.; Stangl, J.; Wallenberg, L. R.; Dick, K. A.; Johansson, J. Phase Transformation in

Radially Merged Wurtzite GaAs Nanowires. *Cryst Growth Des* 2015, 15 (10), 4795–4803. <https://doi.org/10.1021/acs.cgd.5b00507>.

- (27) Al Hassan, A.; Lewis, R. B.; Küpers, H.; Lin, W. H.; Bahrami, D.; Krause, T.; Salomon, D.; Tahraoui, A.; Hanke, M.; Geelhaar, L.; Pietsch, U. Determination of Indium Content of GaAs/(In,Ga)As/(GaAs) Core-Shell(-Shell) Nanowires by x-Ray Diffraction and Nano x-Ray Fluorescence. *Phys Rev Mater* 2018, 2 (1). <https://doi.org/10.1103/PhysRevMaterials.2.014604>.

## Chapter 3

# Analytical Modeling of Nanowire Directional Growth of Asymmetric Shells and Bending

### 3.1 Published: Bending of GaAs–InP Core–Shell Nanowires by Asymmetric Shell Deposition: Implications for Sensors

#### Declaration

**Bending of GaAs–InP Core–Shell Nanowires by Asymmetric Shell Deposition: Implications for Sensors** [ *ACS Applied Nano Materials*, 4(10), 10164–10172.]

Authors: Spencer McDermott and Ryan B. Lewis

Published in **September 2021** in **ACS Applied Nano Materials**, manuscript is cited above and linked here, <https://pubs.acs.org/doi/10.1021/acsanm.1c01636>.

### 3.2 Introduction

The mechanical flexibility of nanowires has recently opened up new possibilities for unconventional strain engineering in semiconductor devices. For example, immense strains of up to 16%—approaching the theoretical elastic limit—have been realized in mechanically stretched Si nanowires,<sup>1</sup> and misfit strain in GaAs-based core–shell nanowire heterostructures has enabled the bandgap of GaAs to be adjusted by up to

40%.<sup>2</sup> In addition to uniform strain fields, bending in nanowires presents a unique opportunity to engineer large strain gradients and to control the nanowire geometry. Bending has been achieved by mechanical manipulation of nanowires<sup>3-8</sup> and spontaneously in asymmetric lattice-mismatched core-shell heterostructures. Asymmetric core-shell bent nanowires have been achieved with III-V materials<sup>9-16</sup> including nitrides,<sup>17</sup> group IV,<sup>18,19</sup> and semiconductor-superconductor hybrids.<sup>10,20,21</sup> The resulting strain gradients can induce quasielectric,<sup>4,5,13</sup> piezoelectric,<sup>3,22,23</sup> and flexoelectric<sup>23,24</sup> fields, which can be employed to control the motion of charge carriers. Strain gradients have been used to enhance the emission intensity of quantum dots (QDs) embedded within the nanowires by more than an order of magnitude compared to straight nanowires.<sup>13</sup> These effects have the potential to lead to faster and more efficient optoelectronic devices. In 2021, the photoconductive properties of In(As,Sb) core-shell bent nanowires were reported.<sup>16</sup>

Fabrication techniques using directional deposition sources have a natural ability to produce the asymmetric nanowire heterostructures that lead to bending. We previously demonstrated that the directionality of molecular beam epitaxy (MBE) is well-suited for controlled bending by asymmetric nanowire shell growth.<sup>13</sup> More recently, controlled bending was also demonstrated using metal-organic molecular beam epitaxy (MOMBE) using metal-organic III sources,<sup>14</sup> as well as electron beam evaporation of transition metals on silicon nanowires.<sup>19</sup> Nano X-ray diffraction analysis on highly bent nanowire heterostructures has revealed large strain and shell thickness variations along the nanowire length.<sup>15</sup> These results highlight the need for a more detailed investigation into

how bending and asymmetric shell deposition proceed in this novel bottom-up bent nanowire growth process.

Theoretical modeling has been used to elucidate bending in asymmetric lattice-mismatched core-shell nanowires by revealing the relationship between shell thickness, asymmetry, and composition on bending curvature.<sup>12,14,25</sup> Modeling has shown that thermal expansion/contraction effects have a negligible effect on bending, with bending resulting from relaxation of the lattice strain.<sup>14</sup> Additionally, a thermodynamic model was used to account for both surface and strain energy effects in the bending of thin nanowires.<sup>25</sup> While these models help to elucidate asymmetric core-shell bending, the effects of bending on the growth process itself—essential for bent nanowire fabrication—have not been explored.

The shadowing of deposition fluxes by neighboring nanowires has been shown to affect nanowire core morphology<sup>26-28</sup> and asymmetric shell growth.<sup>13,19</sup> This flux shadowing has posed challenges for the growth of dense core-shell nanowire arrays. However, the ability to locally influence the deposition on a nanowire by a neighboring object also presents opportunities.

Semiconductor nanowires have been used as ultrasensitive sensors, which take advantage of the nanostructures' high surface-to-volume ratio.<sup>29-34</sup> Recently, InP-based nanowire sensors—attractive because of their low surface recombination and resistance to oxidation—have been fabricated, including a label-free biosensor for DNA and protein markers<sup>35</sup> and a NO<sub>2</sub> gas sensor.<sup>36</sup> These InP sensors were fabricated by first removing

the nanowires from the growth substrate. A bottom-up method of connecting nanowires would allow for straightforward scalable fabrication of sensor devices.

In this work, we model the synthesis of bent nanowires by asymmetric lattice-mismatched shell deposition by a directional flux. We show how bending affects the local deposition along the nanowire, resulting in large variations in the shell thickness, local curvature, and strain along the nanowire, as well as the overall nanowire shape and bending angle. The impact of core and shell dimensions and materials, as well as the geometry of the deposition system, is shown to crucially influence the bending process. Finally, shadowing between nanowire pairs is modeled, presenting a promising means to further control the nanowire geometry and an easier approach for connecting nanowires to form devices. Modeling results are compared to growth experiments of asymmetric GaAs–InP and GaAs–(Al,In)As core–shell bent nanowires. The goal of this paper is to demonstrate the principles of asymmetric nanowire shell growth and present opportunities for employing bending in nanowire device fabrication.

### **3.3 Methods**

The GaAs nanowire cores were grown by self-catalyzed vapor–liquid–solid growth by gas source MBE on p-type Si(111) substrates. The gas sources are arsine and phosphine, cracked for deposition of As<sub>2</sub> and P<sub>2</sub>, respectively. After depositing 30 nm of SiO<sub>2</sub> by chemical vapor deposition, the substrates were patterned with 60–110 nm diameter holes using electron beam lithography and reactive ion etching. Before loading in the molecular beam epitaxy system, the substrates were dipped for 28 s in a dilute solution of 10%

buffered oxide etch 10:1 to remove the native oxide from the holes. The substrates were subsequently heated to 630 °C in the MBE, and then, gallium was predeposited on the wafer for 250 s as depicted in Figure 3.1a. The nanowire cores were grown at a substrate temperature of 630 °C with a V:III flux ratio of 2:4 (Figure 3.1b). After core growth, the substrate was cooled to 300 °C, the substrate rotation was stopped and aligned, and the arsine source was switched to phosphine. The InP shells were grown at a V:III flux ratio of 10 without rotation at a 0.25  $\mu\text{m}/\text{h}$  planar growth rate, as illustrated in Figure 3.1c. The fluxes were incident at an angle of 35° from the substrate normal. An illustration of the resulting asymmetric core-shell bent nanowire can be seen in Figure 3.1d.

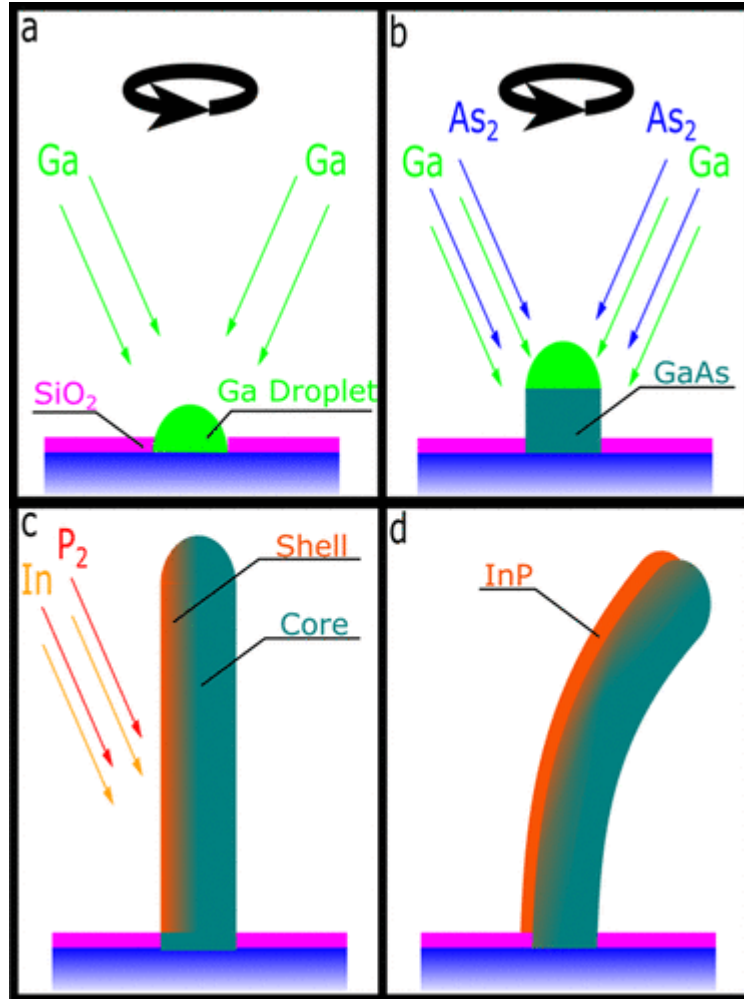


**Figure 3.1.** Illustration of nanowire core and asymmetric shell growth. GaAs nanowire core growth (a,b) is carried out with sample rotation, while shell growth (c,d) is not. (a) Depiction of the Ga predeposition and Ga droplet formation in the patterned oxide holes. (b) GaAs core growth under Ga and As<sub>2</sub> fluxes. (c) Asymmetric InP shell deposition under In and P<sub>2</sub> fluxes. (d) Bent nanowire resulting from the growth process.

Bending in isolated nanowires and nanowire pairs was modeled using GNU Octave.

Asymmetric core-shell nanowires with circular cores were explored, and shell deposition was assumed to be perfectly directional (i.e., surface diffusion and flux divergence were

neglected). A schematic of a core-shell nanowire cross section is shown in Figure 3.2a. Nanowires are divided into 25 nm-long segments along their axis. Within a given segment, the core and shell thicknesses and segment curvature are assumed constant. However, these properties can vary between segments and along the nanowire length. Asymmetric shell deposition is modeled as follows: nanowire cores are initially straight and standing vertically on the substrate. A directional shell deposition is incident at an angle  $\theta$  with respect to the substrate normal. The deposition process is broken into increments (each step corresponding to a planar deposited thickness of 0.05–0.43 nm), and the local deposition on a segment varies as the cosine of the average angle between the segment normal (perpendicular to the nanowire axis) and the incident flux. During a deposition increment, the nanowire shape is held fixed, and the resulting step deposition thickness along the nanowire is calculated. After each deposition step, the curvature of each segment is calculated from linear elastic theory,<sup>13</sup> and the segments are linked to create the complete bent nanowire. The resulting nanowire geometry is used to carry out the next deposition step, and this process is repeated until the shell deposition is completed. There is no deposition on a nanowire segment if the angle between the segment normal and the incident flux is  $>90^\circ$ . In this case, the deposition on the nanowire is self-shadowed by the nanowire itself. This is determined by projecting the flux from the tip of the first nanowire (or object) to the shadowed nanowire. If the segment is below the projected path, then it is shadowed. For both cases, we model shadowing to be fully effective (no deposition on shadowed areas).

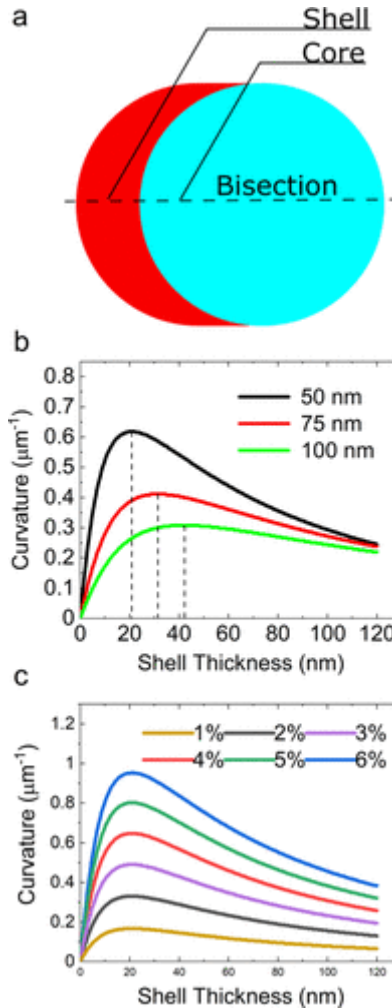


**Figure 3.2.** (a) Schematic representation of the nanowire core–shell cross-sectional geometry with a dashed bisection line. (b) Nanowire segment curvature as a function of shell thickness for three GaAs–InP core–shell nanowires (lattice mismatch of 3.8%) with core diameters of 50, 75, and 100 nm. Maximum curvature occurs for a shell thickness of  $0.42\times$  the nanowire diameter, as indicated with vertical dashed lines in (b). (c) Nanowire curvature as a function of shell thickness for different core–shell lattice mismatches for a 50 nm diameter core.

Shells are assumed to be coherently strained and have a positive lattice mismatch from the core. The accumulation of positive-lattice-mismatched material asymmetrically

deposited on the nanowire results in compressive axial strain in the shell and tensile axial strain in the core. This strain is calculated as described in the Supporting Information of Lewis et al.<sup>13</sup>

Assuming that the nanowire is constrained to be straight, the core and shell share a single axial lattice constant,  $a_{interface}$ , given by eq 3.1. In this case, we define the resulting strain in the core and shell with eqs 3.2 and 3.3.

$$a_{interface} = \frac{a_{core}a_{shell}(a_{core}A_{shell}E_{shell} + a_{shell}A_{core}E_{core})}{a_{core}^2A_{shell}E_{shell} + a_{shell}^2A_{core}E_{core}} \quad (3.1)$$

$$\epsilon_{core} = \frac{a_{interface} - a_{core}}{a_{core}} \quad (3.2)$$

$$\epsilon_{shell} = \frac{a_{interface} - a_{shell}}{a_{shell}} \quad (3.3)$$

Analogous to a bimetallic strip, strain in an unconstrained wire can be partially relieved by bending—resulting in a linear strain gradient along a bisecting line (eq 3.4)—such as that shown in Figure 3.2a.

$$\epsilon = \begin{cases} \epsilon_{core} + \kappa(x - \bar{x}_c) & x < x_{interface} \\ \epsilon_{shell} + \kappa(x - \bar{x}_c) & x \geq x_{interface} \end{cases} \quad (3.4)$$

where  $\kappa$  is the curvature of the nanowire and  $x$  is the position along the bisecting line from right to left in Figure 3.2a. The bending strain gradient is directly proportional to the nanowire's curvature. The strain from bending reduces the total strain energy in the

nanowire compared to the straight case. The point where there is zero bending strain ( $\bar{x}_c$ ) is the Young's modulus weighted centroid. The Young's modulus weighted centroid is the average centroid of the core and shell weighted by their Young's moduli and cross-sectional area (eq 3.5)

$$\bar{x}_c = \frac{\sum_{i=1}^N A_i E_i \bar{x}_i}{\sum_{i=1}^N A_i E_i} \quad (3.5)$$

where  $A_i$  is the cross-sectional area of component  $i$ ,  $E_i$  is the Young's modulus,  $\bar{x}_i$  is the centroid of the component along the bisection, and  $N$  is the total number of components of the nanowire [core plus shell(s)].

The curvature of the nanowire segment is found by minimizing the total elastic potential with respect to the segment curvature. Points are generated along the bisection to numerically compute the elastic potential. The trapezoidal method gives the elastic potential over the cross section (eq 3.6).

$$U = \int_{x_{shell}}^{x_{core}} w(x) E(x) \epsilon(x)^2 \delta x \quad (3.6)$$

where  $E(x)$  is Young's modulus,  $\epsilon(x)$  is strain, and  $w(x)$  is the width along the bisection.  $x_{core}$  and  $x_{shell}$  are the boundary points on the bisection—the innermost surface of the core and the outermost surface of the shell.

Figure 3.2b shows the local segment curvature as a function of shell thickness for GaAs–InP core–shell nanowires with three different core diameters ( $D$ ). The maximum curvature occurs for a shell thickness of  $0.42 \times$  the core diameter. The maximum curvature is inversely proportional to the diameter and obeys eq 3.7.

$$D_1 \times \kappa_{max}(D1) = D_2 \times \kappa_{max}(D2) \quad (3.7)$$

where  $D_1$  and  $D_2$  represent two independent nanowire diameters with the same core–shell material. Therefore, the product of maximum curvature and the diameter is a constant, which depends on the materials composing the nanowire core and shell ( $D_1 \times \kappa_{1,max}$ ). For GaAs–InP nanowires, this constant is 0.031.

### 3.4 Results and Discussion

In Figure 3.2b, the curvature peak broadens with the increasing core diameter. The full width at half maximum (FWHM) is 93 nm for the 50 nm diameter core and scales linearly with the diameter. For a fixed core–shell thickness ratio, the curvature is inversely proportional to the core diameter. For a nanowire with uniform curvature, the bending angle—the angle between the substrate normal and the axis of the tip of the nanowire—is given by the product of the nanowire length and curvature. Consequently, the maximum achievable bending angle is determined by the nanowire core aspect ratio. We note that for real nanowires, the relation between the core diameter and length depends nontrivially on the growth process.

Figure 3.2c presents the local curvature as a function of shell thickness for nanowire segments with 50 nm diameter cores and various core–shell lattice mismatches. The curvature is directly proportional to lattice mismatch, so all curves have the same shape and the peak curvature occurs at a shell thickness of 42% of the core diameter. We note that these results for circular nanowires are consistent,<sup>13</sup> where hexagonal nanowires are considered. The core and shell Young’s moduli were taken as those of GaAs (85.5 GPa)

and InP (61.1 GPa), respectively. There is a small effect from Young's modulus differences between the core and shell: increasing the shell modulus increases and sharpens the peak curvature, and the peak occurs with a thinner shell.

It is important to note that our model ignores adatom diffusion during shell deposition, which could act to reduce the asymmetry of the deposited shells, as atoms could migrate around the nanowire and incorporate on surfaces on which no flux is incident. In principle, the present model could be extended to include symmetric shell growth to account for diffusion. In such a case, the resulting bending would be less than that for our ideal case where diffusion is nonexistent. Diffusion along the nanowire axis is also possible and is expected to have less of an impact on nanowire bending. We expect that the degree to which diffusion impacts the nanowire shape will be highly dependent on the chemical composition of the shell (e.g., In would be expected to diffuse much more than Al) as well as growth conditions (e.g., V:III ratio and substrate temperature). This could be particularly important for the growth of alloy shells, potentially resulting in composition variations around the shell and twisting of the nanowire. The effect of composition variation and shell asymmetry on the bending of GaP-(In,Ga)P core-shell nanowires has previously been reported.<sup>12</sup> The present bending model can be considered as an upper limit on the amount of bending, which can be achieved for a given material system and core geometry. We expect that at sufficiently low temperatures, the role of diffusion would be minimized. In similar light, relaxation from dislocations—important for large core-shell lattice mismatches and large nanowire diameters—would reduce bending, and this is not accounted for in the model. We note that twisting has also been

observed in GaAs-(Ga,In)P core-shell nanowires grown by metal-organic chemical vapor deposition with rotation,<sup>11</sup> and we have not observed this effect in our wires.

During shell growth, the local instantaneous shell deposition rate depends on the local orientation of the nanowire segment relative to the incident flux. Consequently, while the deposition rate is uniform along the length of a straight nanowire, the deposition rate will vary along the length of a bent nanowire and evolve throughout the deposition as the nanowire bends. Figure 3.3a illustrates a bent nanowire under an incident flux. The effective flux on the nanowire sidewall varies along the length of the bent nanowire as a result of the changing local angle between the nanowire surface normal and the incident flux. Variation in total local shell thickness is indicated by shading of the nanowire, showing the shell to be thinner at the base and tip compared to the middle, for this geometry. The tip of this nanowire is self-shadowed.

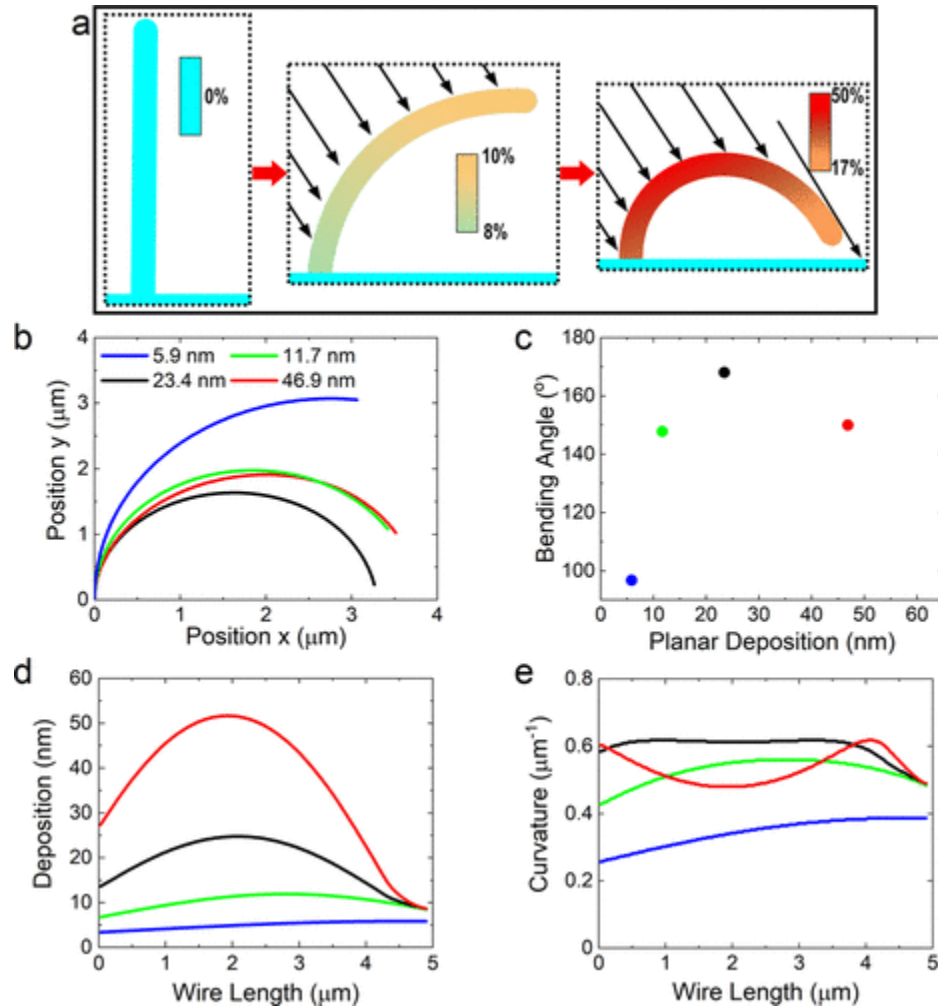


**Figure 3.3.** (a) Schematic representation of a nanowire's bending evolution as the nanowire progresses from being straight to optimally bent. The deposition flux is indicated by black arrows, and the shading on the nanowires indicates the local shell thickness relative to the core diameter. (b–e) Modeling GaAs–InP core–shell nanowires with a 50 nm core diameter and an aspect ratio of 85 for four planar shell depositions: 5.9, 11.7, 23.4, and 46.9 nm at a deposition angle of  $30^\circ$ . (b) Wire geometries projected on a 2D plane. (c) Bending angle of the nanowire tips plotted as a function of planar deposition. (d) Shell thickness along the wire length from the base to the tip. (e) Curvature along the wires. The legend in (b) corresponds to all panels.

The shape and bending angle of GaAs–InP nanowires with a core diameter of 50 nm and an aspect ratio of 85 are shown in Figure 3.3b,c for different stages of shell growth corresponding to four planar deposition thicknesses. Planar depositions of 5.9 and 11.7 nm correspond to fully under-deposited shells (local shell thickness below that corresponding to maximum curvature along the entire nanowire length). In this case, further shell growth will increase the curvature everywhere along the nanowire. The 23.4 nm thickness corresponds to near optimal deposition, resulting in the maximum possible bending angle and average nanowire curvature. Finally, the 46.9 nm thickness results in an over-deposited shell. In this case, the bending angle and average curvature along the nanowire are lower than for the optimally bent nanowire, and further deposition will further reduce the bending angle.

Figure 3.3d,e shows the resulting shell thickness and local curvature along the length of the nanowires for the deposition thicknesses presented in Figure 3.3b. With increasing shell growth, the deposition shifts from the tip of the nanowire toward the nanowire base. The 23.4 nm planar deposition corresponds to an average shell thickness of 19.0 nm, close to the optimal value of 22.5 nm (42% of the core dimension). However, we note that in this case, the local thickness varies by a factor of 2 along the nanowire. Figure 3.3e illustrates the complex dependence of the local curvature on the distance along the nanowire and the deposition thickness. Initially, when the shell is fully under-deposited, the local curvature follows the same trend as the local deposition thickness, showing an initial peak at the nanowire tip, which shifts toward the base with increasing shell growth. At optimal shell deposition, the middle of the nanowire is

slightly over-deposited, while the tip and base are still under-deposited. Under these conditions, the curvature is remarkably constant along a large portion of the nanowire (a result of the slowly decreasing curvature with over-deposition). For the largest shell deposition displayed, the curvature is now peaked at the base and near the tip, with the highly over-deposited middle showing less curvature. These results illustrate the complex evolution of the nanowire shape, shell thickness, and curvature profile along the nanowire with deposition.

The local deposition rate follows the cosine of the angle between the flux and the segment normal, exhibiting a maximum when the segment is perpendicular to the flux. However, when this angle exceeds  $90^\circ$ , the nanowire surface is self-shadowed and local deposition does not occur. Figure 3.3a illustrates self-shadowing at the nanowire tip. Significant self-shadowing has also occurred for the two largest deposition thicknesses in Figure 3.3d,e, explaining why the shell thickness at the nanowire tip remains largely unchanged above 11.7 nm planar deposition.

The deposition angle of the incident flux (fixed by the growth system configuration) has a significant impact on the shell deposition profile and the resulting nanowire geometry. Figure 3.4a,b presents the nanowire side profile and the bending angle of the nanowire tip, respectively, for shell depositions corresponding to 33.3 nm (parallel to the incident flux direction) at varying incident flux angles on nanowire cores of 4  $\mu\text{m}$  length and 50 nm diameter. Figure 3.4a reveals that the final shape is considerably affected by the flux angle, particularly at the tip of the nanowire. At the beginning of shell deposition—the nanowire standing vertically on the substrate—the  $90^\circ$  flux angle results

in the highest shell growth rate. However, this situation changes as the nanowire bends throughout the deposition. As shown in Figure 3.4b, the highest bending angle is achieved for a flux angle of  $30^\circ$  for these conditions. Notably, the amount of deposition affects this result—if deposition continued, then the  $10^\circ$  flux could create a higher bending angle than the  $30^\circ$  flux as less shadowing occurs at the nanowire tip. The low initial growth rate for the  $10^\circ$  flux causes less deposition overall, resulting in a lower bending angle than for the  $30^\circ$  flux. Figure 3.4c reveals how the shell deposition is distributed along the nanowire for different flux angles. For higher deposition angles, the deposition is shifted toward the base of the nanowire, peaking at the base for  $90^\circ$  deposition. Furthermore, the maximum local deposition increases with increasing deposition angle. In contrast, the onset of self-shadowing occurs sooner for higher flux angles, resulting in a larger shadowed region toward the tip of the nanowire, as indicated in Figure 3.4c by the reduced shell thickness toward the nanowire tips. This shadowing reduces the tip curvature, as seen in the curvature plot displayed in Figure 3.4d. These results show that the geometry, bending angle, shell thickness, and curvature along the nanowire depend nontrivially on the deposition angle, as well as the other growth conditions. While the exact behavior depends on other deposition conditions (e.g., nanowire geometry and the deposition amount), in general, shell deposition shifts toward the base of the nanowire as the flux angle increases. Depending on the other deposition conditions, this can have different implications for the bending angle. For instance, as the initial deposition rate (on vertical straight nanowires) increases with increasing flux angle, higher flux angles will result in more bending for highly under-deposited

nanowires (since the shell will be thicker) compared to smaller flux angles, in contrast to the case shown in Figure 3.4, which considers a larger deposition amount. The large impact of the flux angle on shell growth is in contrast to conventional planar layer growth, where the flux angle is essentially irrelevant.

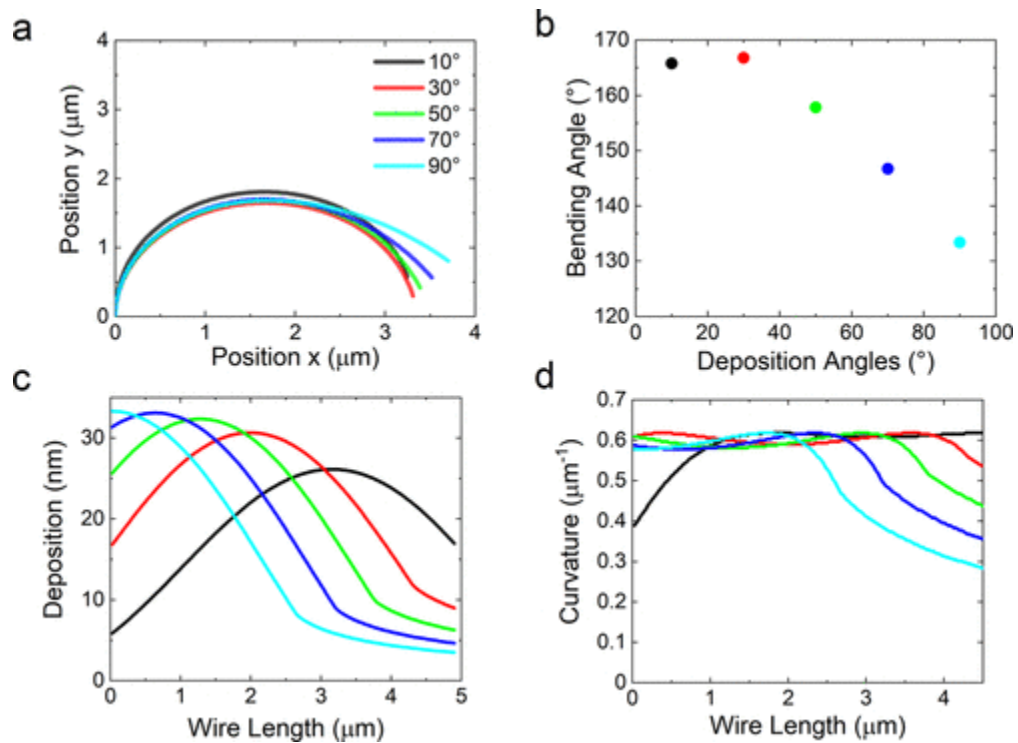


**Figure 3.4.** Effect of varying the angle of the incident flux with respect to the substrate normal for GaAs–InP wires. A deposition of 33.3 nm in the direction parallel to the incident flux was considered for flux angles of 10, 30, 50, 70, and 90 (corresponding to 32.8, 28.9, 21.4, 11.4, and 0 nm planar depositions, respectively), as indicated in the legend in (a), which corresponds to all panels. The wires are 4  $\mu\text{m}$  long with a 50 nm core diameter. (a) Wire geometry projected on a 2D plane. (b) Tip bending angle plotted as a function of the incident flux angle. (c) Local shell thickness along the wire length. The decreasing thickness toward the nanowire tip with increasing deposition angle results from self-shadowing. (d) Local curvature along the wire length.

In addition to self-shadowing, the flux incident on a nanowire can also be shadowed by neighboring nanowires. Figure 3.5a presents a scanning electron micrograph (SEM) of pairs of MBE-grown asymmetric GaAs–InP core–shell nanowires bent to the point of contact. These wires are of a similar composition to Wallentin et al.’s<sup>11</sup> GaAs–GaInP bent core–shell nanowires. As discussed in our previous report,<sup>13</sup> contacting of nanowire pairs with uniform curvature would require bending angles of  $\geq 90^\circ$ . Clearly, the nanowires in Figure 3.5a are bent by much less. In this case, contacting is a result of the different bending profiles of the two nanowires—a result of one nanowire shadowing the flux incident on the other. We modeled pair shadowing assuming that a nanowire will fully block the flux on a portion of a shadowed nanowire if it obstructs the path between that portion of the nanowire and the flux. This assumes a nondivergent flux source and that the nanowire pairs and the incident flux reside in a single plane. Deviations in the alignment of the nanowires as well as broadening of the incident flux angle distribution in the azimuthal direction would result in a reduction in the shadowing effect. Thus, these results represent an upper limit on the effect of pair flux shadowing. Figure 3.5b schematically illustrates pair shadowing, where the flux is partially obstructed from depositing on the nanowire on the right by the nanowire on the left. Figure 3.5c presents model results of three different GaAs–InP nanowire pairs with separations of 1.5–2.5  $\mu\text{m}$ , deposited on until the nanowires are just touching. The cores are 4  $\mu\text{m}$  long and 50 nm in diameter, and the flux is incident at  $30^\circ$  from the substrate normal. The leading nanowire contacts the shadowed nanowire when it bends a horizontal distance approximately equal to the initial separation due to the negligible bending in the lower portion of the

shadowed nanowire. Pair shadowing can dramatically reduce the amount of bending required to connect nanowire pairs, especially if the nanowires are in close proximity. Figure 3.5d,e shows the deposition and curvature along nanowire pairs. The impact of shadowing increases when nanowires are placed closer together. Pair shadowing initially only affects the lower portion of a shadowed nanowire; however, this impacts the bending, which in turn impacts the deposition profile even at the unshadowed tip portion of the nanowire. These results demonstrate how flux shadowing can be employed to further control the shape of bent nanowires, in particular to connect nanowires together for device fabrication. Bent nanowire devices have already been fabricated, e.g., chemical field-effect transistors (chem-FET) by mechanical bending.<sup>6</sup> Pair shadowing presents an easier path for using bending in achieving multiple electrical/optical connections to nanowire-based devices, such as sensors. Such contacts can be made in situ to as-grown nanowires. We propose that by predefining electrically isolated contact regions on the substrate, FET-based nanowire sensors can be fabricated without manipulation of the nanowire post growth. This simple device structure can be the basis for scalable nanowire sensor fabrication. We note that the crystal quality at the tip of nanowires is usually poor, and the material quality at the point where pairs connect is currently unknown. Consequently, one could expect the connection between nanowire pairs to contain crystallographic defects. For bent nanowire chemical field effect transistors, we suggest that the impact of these defects could be mitigated by high doping of the nanowire tips.<sup>6</sup>

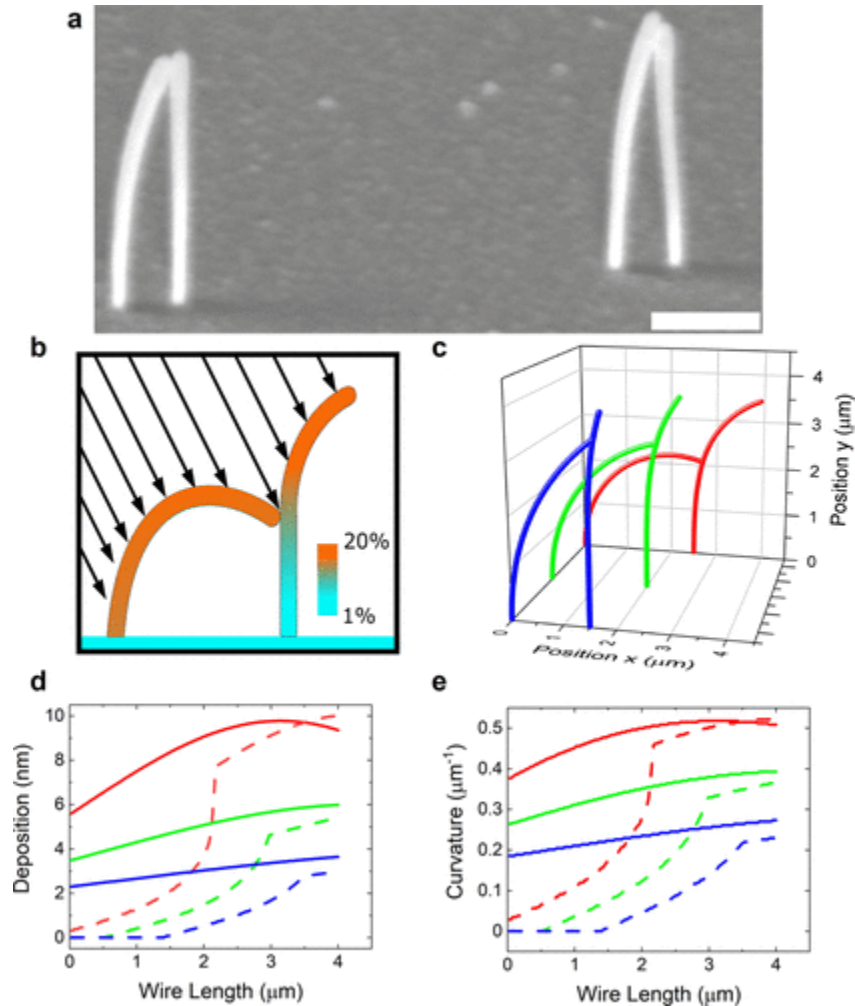


**Figure 3.5.** (a) Scanning electron micrograph of GaAs–InP core–shell nanowire pairs, separated by 600 nm and bent to the point of contact as a result of pair shadowing; the sample is tilted 30°, and the scale bar is 1 μm. (b) Schematic illustration of one nanowire shadowing the incident flux from another; the scale bar represents shell thickness relative to the core diameter. (c) 3D plot of modeled wire geometry of three GaAs–InP nanowire pairs with different separation distances, bent by deposition incident from the left until the point of contact. The pair separations are (blue) 1.5, (green) 2, and (red) 2.5 μm, and the corresponding planar depositions are 4.0, 6.0, and 9.7 nm, respectively. The deposition angle is 30°, and the core aspect ratio is 80 with a diameter of 50 nm. (d) Deposition and (e) curvature along the wire length for the pairs shown in (c). The solid and dashed lines correspond to the unshadowed and shadowed nanowires, respectively.

To further validate our bending model, we compared it to an asymmetric GaAs– $\text{Al}_{0.5}\text{In}_{0.5}\text{As}$  core–shell nanowire from Lewis et al.<sup>13</sup> An SEM image of the nanowire is shown in Figure 3.6a along with modeling results for three sets of conditions: the first is (black curve) the nominal conditions of a uniform shell thickness of 20 nm deposited on a uniform core of 45 nm thickness. These conditions greatly overestimate the curvature of the nanowire. The second is the (red curve) 4.7 nm of deposition on a uniform 45 nm core following our model. This results in a much better fit; however it underestimates the curvature toward the tip of the nanowire. The third is (green curve) a planar deposition of 6.9 nm according to our model with a linearly varying core diameter from 61 to 30 nm from the base to the tip. This core thickness variation is consistent with SEM images of the nanowire cores in the Supporting Information of Lewis et al.<sup>13</sup> Also, the results are consistent with previous modeling done by Greenberg et al.,<sup>14</sup> where it is demonstrated that excluding tapering in the nanowire leads to less bending in the model than the experimental result. Figure 3.6b depicts the curvature along the nanowire for the three models described above. Uniform deposition causes a uniform curvature as seen by the first model (black line). The model corresponding to the tapered core exhibits a rapidly increasing curvature from the base to the tip, consistent with the actual shape of the nanowire in the SEM. These results show how the shape of this wire results from the complex shell deposition process modeled here. Furthermore, they show that tapering in the nanowire core can further complicate the final nanowire shape.

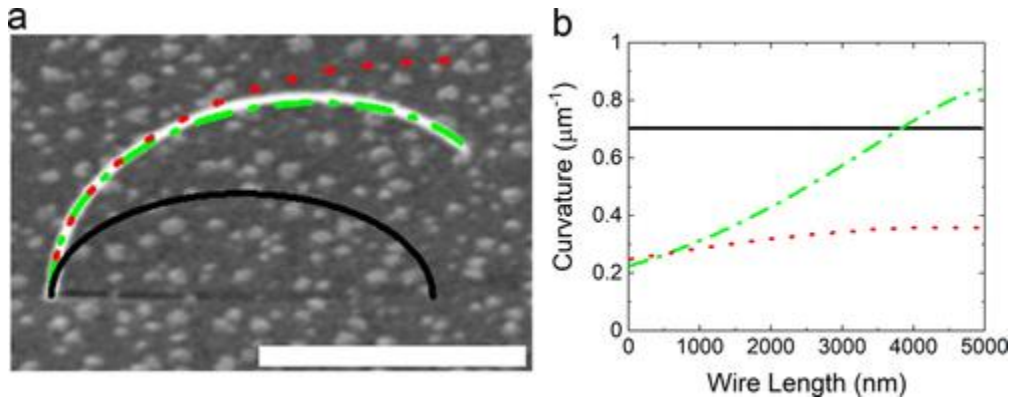


**Figure 3.6.** SEM image of an asymmetric GaAs–Al<sub>0.5</sub>In<sub>0.5</sub>As core–shell nanowire from ref 13 and fit with various shell deposition models. The deposition angle is 33.5° for the GaAs–Al<sub>0.5</sub>In<sub>0.5</sub>As core–shell nanowire. Three model fits are shown: (black line) uniform, unshadowed deposition with the nominal parameters from ref (13) (uniform 20 nm shell and 45 nm core diameter); (red dots) core diameter of 45 nm with a 3.9 nm planar deposition according to our model; (green dot–dashes) linear variation in the core diameter from 61 nm at the base to 30 nm at the tip and a planar deposition of 6.9 nm. The plots have been rescaled to account for the imaging angle of 45° from the substrate plane. The scale bar is 2 μm for the SEM image. (b) Curvature along the wire length from the three models. Reproduced from ref 13. Copyright 2018 American Chemical Society.

### 3.5 Conclusions

A model was developed to explore the underlying mechanisms in nanowire bending from asymmetric shell deposition. Nanowire curvature is limited by core diameter and core–shell lattice mismatch, while the nanowire bending angle is limited by the aspect ratio of the core. Shell deposition and local curvature vary along the length of a nanowire, a consequence of the evolution of the projected flux on the nanowire sidewall, which varies throughout the deposition and along the nanowire as it bends. Our results demonstrate that these effects can have dramatic consequences for the overall growth and nanowire geometry. For instance, in highly bent nanowires, self-shadowing of the nanowire by itself can block deposition completely. Shell deposition is strongly dependent on the

angle of the incident flux from the substrate normal, in contrast to conventional planar layer growth. Shadowing in nanowire pairs was modeled and presents an easy path to connect nanowires without the need for high amounts of bending. Such connected nanowire structures are prospective for nanowire sensors without being removed from the growth substrate, reducing risks of contamination or damage to the nanowires. Our modeling results are consistent with experimental observations from asymmetric GaAs-InP and GaAs-(Al,In)As core-shell nanowires. These findings present new considerations and opportunities for controlling the geometry and strain in nanowires and for enabling the bottom-up fabrication of connected nanowire devices.

## References

- (1) Zhang, H.; Tersoff, J.; Xu, S.; Chen, H.; Zhang, Q.; Zhang, K.; Yang, Y.; Lee, C.-S.; Tu, K.-N.; Li, J.; Lu, Y. Approaching the Ideal Elastic Strain Limit in Silicon Nanowires. *Sci. Adv.* 2016, 2, e1501382 DOI: 10.1126/sciadv.1501382
- (2) Balaghi, L.; Bussone, G.; Grifone, R.; Hübner, R.; Grenzer, J.; Ghorbani-Asl, M.; Krasheninnikov, A. V.; Schneider, H.; Helm, M.; Dimakis, E. Widely Tunable GaAs Bandgap via Strain Engineering in Core/Shell Nanowires with Large Lattice Mismatch. *Nat. Commun.* 2019, 10, 2793, DOI: 10.1038/s41467-019-10654-7
- (3) Kwon, S. S.; Hong, W. K.; Jo, G.; Maeng, J.; Kim, T. W.; Song, S.; Lee, T. Piezoelectric Effect on the Electronic Transport Characteristics of ZnO Nanowire Field-Effect Transistors on Bent Flexible Substrates. *Adv. Mater.* 2008, 20, 4557–4562, DOI: 10.1002/adma.200800691
- (4) Dietrich, C. P.; Lange, M.; Klüpfel, F. J.; von Wenckstern, H.; Schmidt-Grund, R.; Grundmann, M. Strain Distribution in Bent ZnO Microwires. *Appl. Phys. Lett.* 2011, 98, 031105 DOI: 10.1063/1.3544939
- (5) Fu, X.; Su, C.; Fu, Q.; Zhu, X.; Zhu, R.; Liu, C.; Liao, Z.; Xu, J.; Guo, W.; Feng, J.; Li, J.; Yu, D. Tailoring Exciton Dynamics by Elastic Strain-Gradient in Semiconductors. *Adv. Mater.* 2014, 26, 2572–2579, DOI: 10.1002/adma.201305058

- (6) Zhao, Y.; Yao, J.; Xu, L.; Mankin, M. N.; Zhu, Y.; Wu, H.; Mai, L.; Zhang, Q.; Lieber, C. M. Shape-Controlled Deterministic Assembly of Nanowires. *Nano Lett.* 2016, 16, 2644– 2650, DOI: 10.1021/acs.nanolett.6b00292
- (7) Zhang, C.; Kvashnin, D. G.; Bourgeois, L.; Fernando, J. F. S.; Firestein, K.; Sorokin, P. B.; Fukata, N.; Golberg, D. Mechanical, Electrical, and Crystallographic Property Dynamics of Bent and Strained Ge/Si Core-Shell Nanowires As Revealed by in Situ Transmission Electron Microscopy. *Nano Lett.* 2018, 18, 7238– 7246, DOI: 10.1021/acs.nanolett.8b03398
- (8) Ghosh, P.; Lu, J.; Luo, H.; Wang, W.; Xu, Z.; Qiu, M.; Li, Q. Constructing Metal Arch Nanobridges Utilizing a Photothermal-Induced Nanobonding Technique. *Adv. Electron. Mater.* 2019, 5, 1800807, DOI: 10.1002/aelm.201800807
- (9) Keplinger, M.; Kriegner, D.; Stangl, J.; Mårtensson, T.; Mandl, B.; Wintersberger, E.; Bauer, G. Core-Shell Nanowires: From the Ensemble to Single-Wire Characterization. *Nucl. Instrum. Methods Phys. Res., Sect. B* 2010, 268, 316– 319, DOI: 10.1016/j.nimb.2009.09.043
- (10) Krogstrup, P.; Ziino, N. L. B.; Chang, W.; Albrecht, S. M.; Madsen, M. H.; Johnson, E.; Nygård, J.; Marcus, C. M.; Jespersen, T. S. Epitaxy of Semiconductor-Superconductor Nanowires. *Nat. Mater.* 2015, 14, 400– 406, DOI: 10.1038/nmat4176
- (11) Wallentin, J.; Jacobsson, D.; Osterhoff, M.; Borgström, M. T.; Salditt, T. Bending and Twisting Lattice Tilt in Strained Core-Shell Nanowires Revealed by

- Nanofocused X-Ray Diffraction. *Nano Lett.* 2017, 17, 4143– 4150, DOI: 10.1021/acs.nanolett.7b00918
- (12) Gagliano, L.; Albani, M.; Verheijen, M. A.; Bakkers, E. P. A. M.; Miglio, L. Twofold Origin of Strain-Induced Bending in Core-Shell Nanowires: The GaP/InGaP Case. *Nanotechnology* 2018, 29, 315703, DOI: 10.1088/1361-6528/aac417
- (13) Lewis, R. B.; Corfdir, P.; Küpers, H.; Flissikowski, T.; Brandt, O.; Geelhaar, L. Nanowires Bending over Backward from Strain Partitioning in Asymmetric Core-Shell Heterostructures. *Nano Lett.* 2018, 18, 2343– 2350, DOI: 10.1021/acs.nanolett.7b05221
- (14) Greenberg, Y.; Kelrich, A.; Cohen, S.; Kar-Narayan, S.; Ritter, D.; Calahorra, Y. Strain-Mediated Bending of InP Nanowires through the Growth of an Asymmetric InAs Shell. *Nanomaterials* 2019, 9, 1327, DOI: 10.3390/nano9091327
- (15) Davtyan, A.; Kriegner, D.; Holý, V.; AlHassan, A.; Lewis, R. B.; McDermott, S.; Geelhaar, L.; Bahrami, D.; Anjum, T.; Ren, Z.; Richter, C.; Novikov, D.; Müller, J.; Butz, B.; Pietsch, U. X-Ray Diffraction Reveals the Amount of Strain and Homogeneity of Extremely Bent Single Nanowires. *J. Appl. Crystallogr.* 2020, 53, 1310– 1320, DOI: 10.1107/S1600576720011516
- (16) Yao, X.; Zhang, X.; Sun, Q.; Wei, D.; Chen, P.; Zou, J. Anomalous Photoelectrical Properties through Strain Engineering Based on a Single Bent

- InAsSb Nanowire. *ACS Appl. Mater. Interfaces* 2021, 13, 5691– 5698, DOI: 10.1021/acsami.0c16028
- (17) Hetzl, M.; Winnerl, J.; Francaviglia, L.; Kraut, M.; Döblinger, M.; Matich, S.; FontcubertaMorral, A.; Stutzmann, M. Surface Passivation and Self-Regulated Shell Growth in Selective Area-Grown GaN-(Al,Ga)N Core-Shell Nanowires. *Nanoscale* 2017, 9, 7179– 7188, DOI: 10.1039/c7nr00802c
- (18) Day, R. W.; Mankin, M. N.; Lieber, C. M. Plateau-Rayleigh Crystal Growth of Nanowire Heterostructures: Strain-Modified Surface Chemistry and Morphological Control in One, Two, and Three Dimensions. *Nano Lett.* 2016, 16, 2830– 2836, DOI: 10.1021/acs.nanolett.6b00629
- (19) Xu, Y.; Li, L.; Zang, Y.; Hu, J.; Li, Z.; Chen, H.; Zhang, G.; Xia, C.; Cho, J.-H. Forward Bending of Silicon Nanowires Induced by Strain Distribution in Asymmetric Growth. *Mater. Lett.* 2021, 297, 129929, DOI: 10.1016/j.matlet.2021.129929
- (20) Hilse, M.; Takagaki, Y.; Herfort, J.; Ramsteiner, M.; Herrmann, C.; Breuer, S.; Geelhaar, L.; Riechert, H. Ferromagnet-Semiconductor Nanowire Coaxial Heterostructures Grown by Molecular-Beam Epitaxy. *Appl. Phys. Lett.* 2009, 95, 133126, DOI: 10.1063/1.3240405
- (21) Bjergfelt, M.; Carrad, D. J.; Kanne, T.; Aagesen, M.; Fiordaliso, E. M.; Johnson, E.; Shojaei, B.; Palmstrøm, C. J.; Krogstrup, P.; Jespersen, T. S.; Nygård, J. Superconducting Vanadium / Indium-Arsenide Hybrid Nanowires. *Nanotechnology* 2019, 30, 294005, DOI: 10.1088/1361-6528/ab15fc

- (22) Xu, S.; Guo, W.; Du, S.; Loy, M. M. T.; Wang, N. Piezotronic Effects on the Optical Properties of ZnO Nanowires. *Nano Lett.* 2012, 12, 5802– 5807, DOI: 10.1021/nl303132c
- (23) Geng, D.; Pook, A.; Wang, X. Mapping of Strain-Piezopotential Relationship along Bent Zinc Oxide Microwires. *Nano Energy* 2013, 2, 1225– 1231, DOI: 10.1016/j.nanoen.2013.05.008
- (24) Fu, Q.; Zhang, Z. Y.; Kou, L.; Wu, P.; Han, X.; Zhu, X.; Gao, J.; Xu, J.; Zhao, Q.; Guo, W.; Yu, D. Linear Strain-Gradient Effect on the Energy Bandgap in Bent CdS Nanowires. *Nano Res.* 2011, 4, 308– 314, DOI: 10.1007/s12274-010-0085-6
- (25) Zang, H.; Chen, H.; Li, X.; Zhao, Y. An Analytical Model for the Bending of Radial Nanowire Heterostructures. *Phys. Chem. Chem. Phys.* 2019, 21, 9477– 9482, DOI: 10.1039/c9cp00434c
- (26) Kelrich, A.; Calahorra, Y.; Greenberg, Y.; Gavrilov, A.; Cohen, S.; Ritter, D. Shadowing and Mask Opening Effects during Selective-Area Vapor-Liquid-Solid Growth of InP Nanowires by Metalorganic Molecular Beam Epitaxy. *Nanotechnology* 2013, 24, 475302, DOI: 10.1088/0957-4484/24/47/475302
- (27) Gibson, S. J.; LaPierre, R. R. Model of Patterned Self-Assisted Nanowire Growth. *Nanotechnology* 2014, 25, 415304, DOI: 10.1088/0957-4484/25/41/415304
- (28) Schroth, P.; Al Humaidi, M.; Feigl, L.; Jakob, J.; Al Hassan, A.; Davtyan, A.; Küpers, H.; Tahraoui, A.; Geelhaar, L.; Pietsch, U.; Baumbach, T. Impact of the Shadowing Effect on the Crystal Structure of Patterned Self-Catalyzed GaAs Nanowires. *Nano Lett.* 2019, 19, 4263– 4271, DOI: 10.1021/acs.nanolett.9b00380

- (29) Cui, Y.; Wei, Q.; Park, H.; Lieber, C. M. Nanowire Nanosensors for Highly Sensitive and Selective Detection of Biological and Chemical Species. *Science* 2001, 293, 1289– 1292, DOI: 10.1126/science.1062711
- (30) Law, M.; Kind, H.; Messer, B.; Kim, F.; Yang, P. Photochemical Sensing of NO<sub>2</sub> with SnO<sub>2</sub> Nanoribbon Nanosensors at Room Temperature. *Angew. Chem., Int. Ed.* 2002, 41, 2405– 2408, DOI: 10.1002/1521-3773(20020703)41:13 3.0.CO;2-3
- (31) Comini, E.; Faglia, G.; Sberveglieri, G.; Pan, Z.; Wang, Z. L. Stable and Highly Sensitive Gas Sensors Based on Semiconducting Oxide Nanobelts. *Appl. Phys. Lett.* 2002, 81, 1869– 1871, DOI: 10.1063/1.1504867
- (32) Zhou, X. T.; Hu, J. Q.; Li, C. P.; Ma, D. D. D.; Lee, C. S.; Lee, S. T. Silicon Nanowires as Chemical Sensors. *Chem. Phys. Lett.* 2003, 369, 220– 224, DOI: 10.1016/S0009-2614(02)02008-0
- (33) Hahm, J. I.; Lieber, C. M. Direct Ultrasensitive Electrical Detection of DNA and DNA Sequence Variations Using Nanowire Nanosensors. *Nano Lett.* 2004, 4, 51– 54, DOI: 10.1021/nl034853b
- (34) Wang, W. U.; Chen, C.; Lin, K.-H.; Fang, Y.; Lieber, C. M. Label-Free Detection of Small-Molecule-Protein Interactions by Using Nanowire Nanosensors. *Proc. Natl. Acad. Sci. U. S. A.* 2005, 102, 3208– 3212, DOI: 10.1073/pnas.0406368102
- (35) Janissen, R.; Sahoo, P. K.; Santos, C. A.; da Silva, A. M.; von Zuben, A. A. G.; Souto, D. E. P.; Costa, A. D. T.; Celedon, P.; Zanchin, N. I. T.; Almeida, D. B.; Oliveira, D. S.; Kubota, L. T.; Cesar, C. L.; Souza, A. P. D.; Cotta, M. A. InP Nanowire Biosensor with Tailored Biofunctionalization: Ultrasensitive and

Highly Selective Disease Biomarker Detection. *Nano Lett.* 2017, 17, 5938– 5949,

DOI: 10.1021/acs.nanolett.7b01803

- (36) Bai, M.; Huang, H.; Liu, Z.; Zhan, T.; Xia, S.; Li, X.; Sibirev, N.; Bouravleuv, A.; Dubrovskii, V. G.; Cirilin, G. InAs/InP Core/Shell Nanowire Gas Sensor: Effects of InP Shell on Sensitivity and Long-Term Stability. *Appl. Surf. Sci.* 2019, 498, 143756, DOI: 10.1016/j.apsusc.2019.143756

## Chapter 4

# Indium-diffusion-limited and Phosphorus- Controlled Nanoepitaxy of InP Shell on GaAs Nanowires

### 4.1 Published: Phosphorus-Controlled Nanoepitaxy of Asymmetric GaAs–InP Core–Shell Bent Nanowires:

### Implications for Bottom-Up Nanowire Transistors and Sensors

#### Declaration

Phosphorus-Controlled Nanoepitaxy of Asymmetric GaAs–InP Core–Shell Bent  
Nanowires: Implications for Bottom-Up Nanowire Transistors and Sensors

Declaration [ *ACS Applied Nano Materials*, 7(1), 1257–1264.]

Authors: Spencer McDermott, Trevor R. Smith, Ray R. LaPierre and Ryan B. Lewis

Published in **December 2023** in **ACS Applied Nano Materials**, manuscript is cited  
above and linked here, <https://pubs.acs.org/doi/10.1021/acsanm.3c05235>.

## 4.2 Introduction

The epitaxial growth of three-dimensional nano-heterostructures presents a vast design landscape to realize novel and creative nanostructures and devices with bottom-up and scalable fabrication. To harness these wide-ranging design opportunities, the complex three-dimensional (3D) deposition geometries and the role of adatom diffusion on faceted nanostructures present growth challenges that must be understood. Recently, spontaneous bending of free-standing nanowires with an asymmetric lattice-mismatched core-shell heterostructure has gathered interest, presenting novel strain and geometry engineering opportunities with applications in sensing and optoelectronics. These structures undergo spontaneous bending to relieve misfit strain between the core and the asymmetric shell, which can be fabricated by directional deposition (selective flux exposure around the nanowire). Bent nanowires have been synthesized using molecular beam epitaxy (MBE),<sup>1-6</sup> metal-organic MBE,<sup>7</sup> and electron beam evaporation.<sup>8-10</sup> A variety of shell materials have been explored, including group III-V,<sup>2-5,7,9,11-15</sup> group IV,<sup>16</sup> nitrides,<sup>17</sup> and transition-metal-based shells with III-V or IV cores.<sup>1,8,10</sup> Additionally, bent nanowires<sup>18</sup> and nanowires connected through bending<sup>2,3</sup> have been proposed as a scalable fabrication approach for ultrasensitive sensors. InP-based nanowires have been used as transducers in field-effect transistors (FET),<sup>19,20</sup> and FET-based devices fabricated by bending nanowire pairs together have been proposed.<sup>3</sup> Bending nanowires together is a massively parallel deterministic fabrication technique allowing for bottom-up connection of nanowire pairs on a substrate. This technique can simplify current

processes for fabricating nanowire FET-based sensors by forming structures with two substrate electrical connection points and an out-of-substrate-plane geometry. The ability to control the pitch and density of the nanowires through selective area growth also enables tailoring mass transport for sensor-based applications,<sup>21</sup> and the out-of-plane geometry (off the substrate) of the nanowire pair is highly favorable for mass transport, similar to suspended nanowire sensors<sup>21-25</sup> and suspended film sensors,<sup>26</sup> making this method ideal for mass production of nanosensors.

For III–V nanowires, deliberate bending was shown to take place along the group III flux direction, and the role of adatom diffusion has thus far been ignored.<sup>2,3</sup> In general, the distribution of the asymmetric shell determines the bending direction, and for positive lattice-mismatched shells (shell lattice parameter > core lattice parameter), the nanowires bend away from where the shell forms.<sup>2,3,13-15</sup> However, recent reports by Al-Humaidi et al.<sup>4,5</sup> observed bending both along the V ( $\text{As}_4$ ) flux direction and along the III (Ga) flux direction during the growth of the  $\text{In}_x\text{Ga}_{1-x}\text{As}$  shells on GaAs cores, although an explanation for this observation was not provided. Additionally, for the Bi surfactant-directed growth of InAs quantum dots on nanowire sidewalls, InAs growth was shown to occur on As-facing facets and not on In-facing facets.<sup>2</sup> These results highlight the need for a more detailed understanding of the nanoepitaxial growth process.

For the GaAs MBE on planar and faceted GaAs surfaces, differences in the partial pressure of arsenic have been shown to alter the Ga incorporation diffusion length, driving selective and asymmetrical growth. For growth on faceted GaAs surfaces, the

transfer of Ga adatoms (and growth) to facets receiving higher incident  $\text{As}_4$  flux has been demonstrated.<sup>27</sup> The effect of arsenic partial pressure on Ga adatom incorporation diffusion length has been shown to be linear at lower and quadratic at higher arsenic pressures,<sup>27,28</sup> for both  $\text{As}_4$  and  $\text{As}_2$ .<sup>29</sup> Similarly, InAs quantum dot growth on rippled GaAs surfaces are known to favor areas of the surface with locally higher incident  $\text{As}_4$  flux.<sup>30</sup> The effect was observed at temperatures above 500 °C where In adatom diffusion was sufficient to enable selective growth.<sup>30-33</sup> However, the impact of adatom diffusion and incorporation on nanowire shell growth has not been explored.

In this work, we reveal the crucial role that adatom diffusion and deposition geometry play in the MBE growth of GaAs–InP core–shell bent nanowires and connected bent nanowire pairs. InP has a 3.75% lattice mismatch from GaAs ( $a_{\text{InP}} = 5.87 \text{ \AA}$ ,  $a_{\text{GaAs}} = 5.65 \text{ \AA}$ ). By varying the InP shell growth temperatures—and thus the In adatom migration length—the growth transitions from In-diffusion-controlled to phosphorus-flux-controlled, with the resulting InP shell geometry determined by the incident In and  $\text{P}_2$  fluxes, respectively. Transmission electron microscopy (TEM) and energy-dispersive X-ray spectroscopy (EDS) analysis elucidate the nanowire cross sections and shell distributions, revealing the phosphorus-controlled growth regime as a stable and deterministic process for precise synthesis of bent nanowire structures. This growth regime is employed to synthesize bent nanowire pairs, which are of high interest for sensing applications. TEM and EDS analysis of these structures quantifies the impact of flux shadowing and demonstrates that the connected nanowires are intimately fused

together by the InP shell. These results will pave the way for the fabrication of bottom-up scalable nanosensors.

### 4.3 Methods

Samples were grown on patterned SiO<sub>2</sub>-covered Si(111) substrates (substrate preparation described in the Supporting Information on pages S1 and S2) by gas-source MBE in a SVTA-MBE35 reactor. The Ga and In fluxes were provided by solid-source effusion cells, while the P<sub>2</sub> flux was provided via phosphine flow cracked at 1000 °C. The sources were incident on the substrate at an angle of 33.5° from the substrate normal. GaAs nanowire cores were grown with a gallium droplet catalyst (see the Supporting Information on pages S2 and S3 for core growth details). After core growth, the substrate rotation angle (and thus the angle of the incident fluxes with respect to the nanowire side facets) was set to a fixed position for InP shell deposition (cf. Figure 4.1c). InP shells were deposited under a V:III flux ratio (P:In) of 10:1 at an In flux corresponding to a planar InP growth rate of 0.25 μm/h. The In and P<sub>2</sub> fluxes were separated by an azimuthal angle of 108°. Nanowire pairs were aligned in the direction of either the In beam or the P<sub>2</sub> beam. The side facet geometry corresponds with the substrate crystallographic directions. The nanowire side facets are aligned (with respect to the source fluxes) before shell deposition by rotating the substrate to a desired azimuthal angle. The substrate oxide is patterned in such a way that aligning the crystallographic directions of the Si substrate also aligned the nanowire pairs. InP asymmetric shells were grown at various substrate temperatures: 210, 295, 380, and 440 °C.

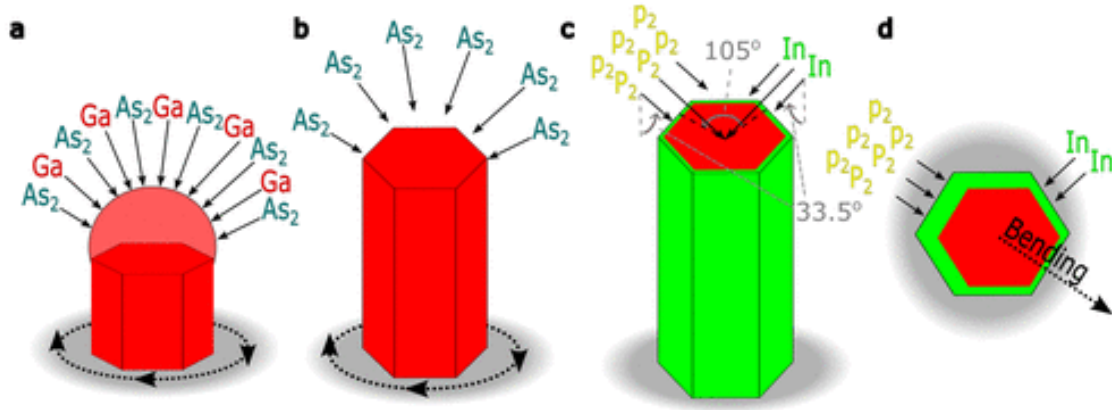


**Figure 4.1.** Illustration of the asymmetric core-shell nanowire MBE growth process. (a) Vapor-liquid-solid GaAs core growth showing the gallium droplet (red and translucent) on the top of the nanowire (red) under incident Ga and  $\text{As}_2$  fluxes. (b) Consumption of the gallium droplet after core growth under  $\text{As}_2$ . The arrows at the base of the nanowire in (a) and (b) indicate substrate rotation. (c) InP shell grown around the core with  $\text{P}_2$  incident from the left and indium from the right. Both fluxes are unidirectional and have an azimuthal separation angle of  $108^\circ$  and an inclination angle of  $33.5^\circ$  measured from the substrate normal. (d) Top view of an asymmetric core-shell nanowire with a bending direction in line with the  $\text{P}_2$  flux. This bending direction is observed for temperatures  $\geq 380^\circ\text{C}$ .

The nanowire morphology was examined by scanning electron microscopy (SEM) with a JEOL JSM-7000F and with TEM in a Talos F200X. The SEM images were obtained using a positively charged JEOL Everhart-Thornley detector to measure secondary electrons. Nanowire cross sections for TEM were obtained from microtomy with a Leica UCT ultramicrotome. The microtome cuts were placed on TEM grids. Once loaded they were tilted to align the  $\langle 111 \rangle$  nanowire axis for high-angle annular dark field (HAADF), EDS, bright-field, and phase-contrast TEM imaging. EDS was performed in the TEM on

the nanowire cross sections. The shell thickness around the nanowire perimeter was deduced from the EDS maps (see Supporting Information pages S3–S8 for details).

## 4.4 Results and Discussion

Top-view and side-view SEM images of GaAs–InP core–shell nanowires grown with various InP shell growth temperatures are presented in Figure 4.2a–d. InP shell growth at the lowest temperature (210 °C) with a planar deposition of 40 nm (Figure 4.2a) exhibits little bending. We note that the nanowire sidewalls appear rough, and there is substantial parasitic growth on the substrate at this growth temperature. Increasing the shell growth temperature to 295 °C at the same planar deposition (Figure 4.2b) results in smoother nanowire sidewall facets and more bending. The azimuthal bending direction from the In flux is  $\sim 70^\circ$  at the nanowire base, curling toward  $\sim 45^\circ$  at the tip, suggesting that shell growth occurred predominantly on the nanowire sidewall facet with the highest overlapping In and P<sub>2</sub> fluxes. This twisting is visible in the top view from the path traced by the observable side facets. There is an increase of length between nanowires grown with shells at 295 and 210 °C. It is unknown whether the difference in length is a result of axial InP growth or variation in the core length. For higher growth temperatures of 380 and 440 °C with a planar deposition of 9 nm (Figures 4.2c and 2d, respectively), the nanowires are highly bent along the incident P<sub>2</sub> flux direction, suggesting that shell growth occurred predominantly on the P<sub>2</sub>-facing facets. We note that the incident P<sub>2</sub> flux on the left nanowire in Figure 4.2d was impacted by the proximity of the nanowire on the right. This shadowing effect is discussed below and is not expected to impact the right

nanowire. Most bending occurred at 380 °C with a projected in-plane length of 1.2  $\mu\text{m}$ . We note that Al-Humaidi et al. recently observed the bending direction of GaAs–In<sub>x</sub>Ga<sub>1-x</sub>As core–shell nanowires depended on the substrate.<sup>4</sup> The present findings suggest a difference in adatom diffusion along the nanowires as a possible explanation—from the temperature or other factors.

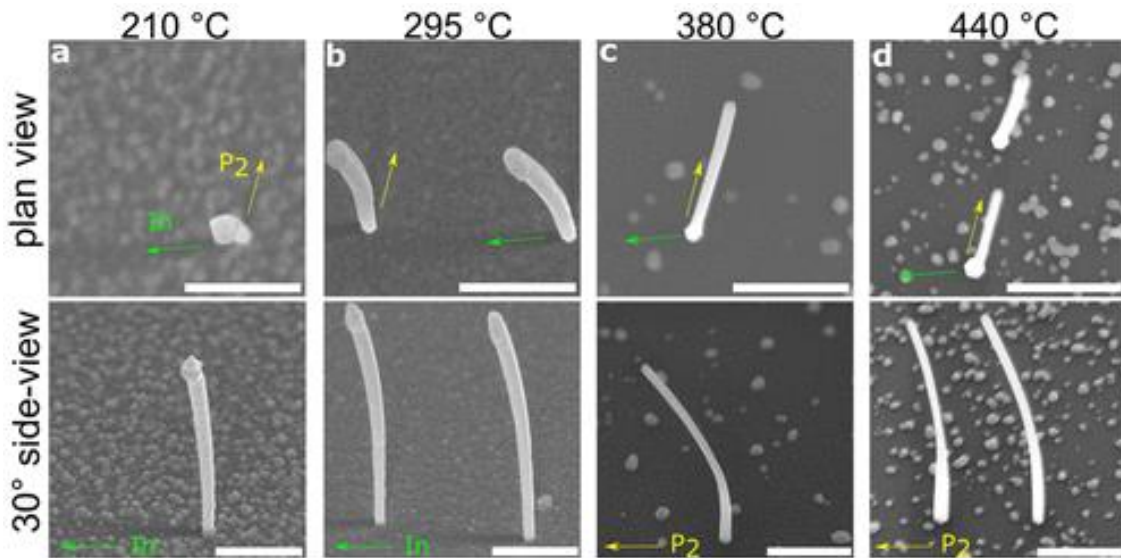


**Figure 4.2.** SEM images of GaAs–InP core–shell nanowires grown at InP shell growth temperatures of 210 (a), 295 (b), 380 (c), and 440 °C (d). The top row shows plan view micrographs, indicating the bending direction with respect to the incident In and P<sub>2</sub> fluxes. The bottom row presents inclined side-view images aligned azimuthally perpendicular to either the incident In (a, b) or P<sub>2</sub> (c, d) flux. The In and P<sub>2</sub> source fluxes projected on the substrate are indicated by green and yellow arrows, respectively. Scale bars correspond to 1  $\mu\text{m}$ .

Nanowires were characterized by cross-sectional TEM and EDS to further investigate the impact of substrate temperature on the InP shell growth. Figure 4.3 presents HAADF micrographs and EDS maps of nanowires grown at 210 °C with a planar deposition of 40

nm (a, c) and 380 °C with a planar deposition of 9 nm (d–f). For shell growth at 210 °C, the HAADF image (Figure 4.3a) indicates inhomogeneous shell growth, with considerable variation in shell thickness on each facet (see additional TEM images and EDS maps in the Supporting Information on pages S9 and S10). The shell morphology and HAADF contrast are hypothesized to be the result of plastic strain relaxation. We note the similarity to previously reported plastically relaxed (In,Ga)As mounds,<sup>34</sup> mounds resulting from strain relaxation in Ge–Si core–shell nanowire heterostructures.<sup>35,36</sup> Mound formation resulting from plastic strain relaxation has also been modeled on nanowire side facets.<sup>37</sup> The presence of plastic relaxation in the core–shell heterostructure would explain why these nanowires do not exhibit significant bending despite considerable asymmetry in the shell.

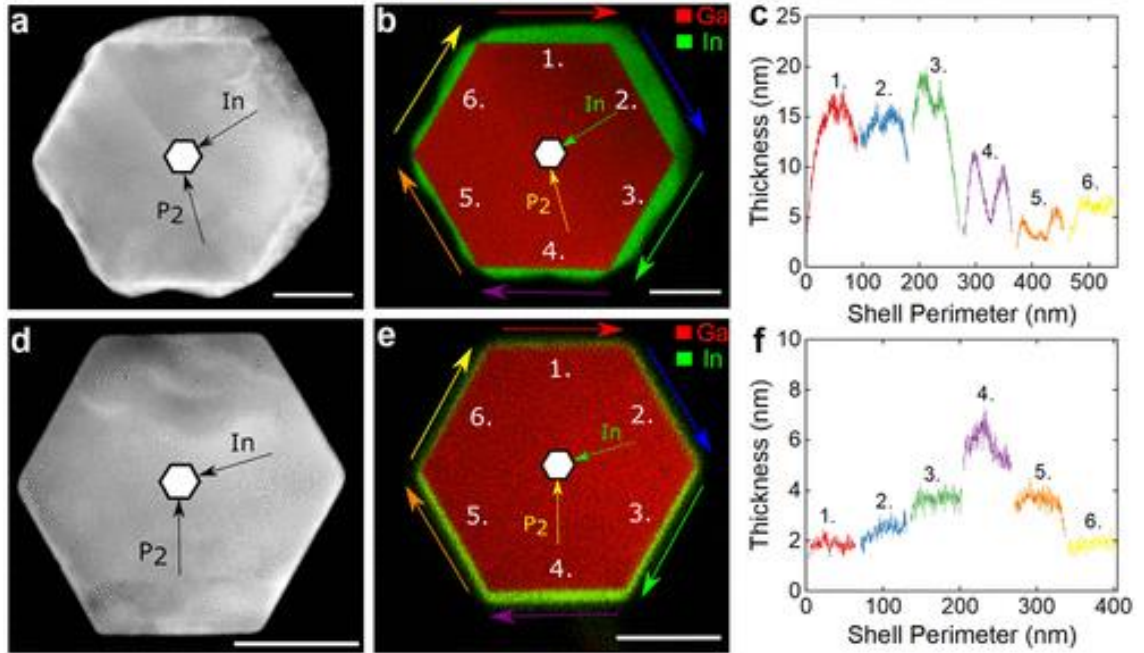


**Figure 4.3.** TEM investigation of microtome cross sections for nanowires with shells grown at 210 °C (a, c) and 380 °C (d, f) presenting HAADF micrographs (a, d) and EDS maps (b, e). The EDS maps show that while shell growth occurred on all facets, it occurred predominantly on In-facing facets at 210 °C and P<sub>2</sub>-facing facets at 380 °C. This is confirmed by plotting the shell thickness—extracted from the EDS maps—around the nanowire core, as illustrated in (c) and (f) for 210 and 380 °C, respectively. The incident flux directions are indicated in (a) and (d), corresponding to In impingement on facet 2 and P<sub>2</sub> impingement on facet 4, respectively. The color and numbering of the EDS line scans correspond to the labels on the EDS maps, indicating the path around the nanowire shell. Scale bars are 50 nm. Both EDS maps are of net intensity.

The corresponding EDS map of In and Ga is shown in Figure 4.3b, demarcating the InP shell and the GaAs core. The EDS map demonstrates that the facets with direct In impingement received the most InP deposition at 210 °C. EDS line scans around the shell are shown in Figure 4.3c, where the number and color correspond to the labels in Figure 4.3b. We note the presence of contrast variations between shell facets in the EDS

map and plotted thickness for growth at 210 °C (see the Supporting Information on page S11 for additional images). The three facets that received direct In impingement (line scans 1–3) all show more InP growth than the facets that did not receive direct In flux (line scans 4–6). The cross-sectional shell area was  $1330 \pm 90 \text{ nm}^2$  for facet 2, almost twice the  $730 \pm 50 \text{ nm}^2$  for facet 4. These results indicate that the diffusion of In around the nanowire was an important limiting factor in shell formation.

In contrast to shell growth at 210 °C, the HAADF image of the nanowire grown at 380 °C (Figure 4.3d) exhibits a smooth hexagonal sidewall surface with consistent contrast. In this case, the EDS map (Figure 4.3e) and InP shell thickness (Figure 4.3f) show that the three facets facing toward the  $P_2$  flux all have thicker shells than those facing away. Specifically, the shell thicknesses on facets 3 and 5 are similar, despite facet 3 being exposed to the In beam and facet 5 facing away from the In flux—both facets received the same direct  $P_2$  flux. The favoring of shell formation under the  $P_2$  flux at 380 °C is similar to the selective growth of InAs QDs on wavy surfaces, where the QDs formed on areas with locally higher direct As impingement.<sup>30</sup> These results suggest coherent InP shell growth—necessary to maximize bending and for most device applications—requires sufficient substrate temperature as seen for shells grown at 380 °C and greater. In planar GaAs growth studies, the Ga incorporation diffusion length was found to be linearly proportional to the impinging  $As_2$  flux.<sup>29</sup> As the group V surface diffusion length is negligible,<sup>38</sup> we expect the relative growth rate to be proportional to the incident  $P_2$  flux on a facet if the In adatom diffusion length is considerably larger than the nanowire

circumference, such that In adatoms can freely diffuse around the nanowire. In this case, the InP shell growth rate will depend on the relative P<sub>2</sub> flux around the cross section.

The sources of impinging phosphorus on the nanowire facets are direct impingement and scattering/re-emission from the oxide mask. Assuming the scattered flux to be equivalent in all directions (equal scattered flux on all side facets) and assuming that the growth rate is directly proportional to the incident P<sub>2</sub> flux, the growth rate,  $\frac{\partial g_s}{\partial t}$ , on a side facet,  $s$ , is

$$\frac{\partial g_s}{\partial t} = C F_{P,s} = C \begin{cases} F_{P,direct} \langle \hat{b}_p \cdot -\hat{n} \rangle + F_{P,scattered} & 0 < \langle \hat{b}_p \cdot -\hat{n} \rangle \\ F_{P,scattered} & 0 \geq \langle \hat{b}_p \cdot -\hat{n} \rangle \end{cases} \quad (4.1)$$

where  $F_{P,scattered}$  and  $F_{P,direct}$  are the P<sub>2</sub> impingement from scattering and the direct beam, respectively.  $F_{P,s}$  is the total P<sub>2</sub> impingement on a side facet,  $s$ ,  $\hat{b}_p$  is a vector pointing along the direction of the P<sub>2</sub> flux,  $\hat{n}$  is the normal vector of the side facet, and  $C$  is a constant relating P<sub>2</sub> impingement to growth. From the average measured thickness of the side facets, we calculate growth rate contributions for the direct beam ( $F_{P,direct} \langle \hat{b}_p \cdot -\hat{n} \rangle$ ) of  $0.16 \pm 0.03$   $\mu\text{m/h}$  and scattering ( $C F_{P,scattered}$ ) of  $0.05 \pm 0.01$   $\mu\text{m/h}$  (see the Supporting Information on pages S8 and S9 for details). This corresponds to a P<sub>2</sub> scattering flux of  $31 \pm 8\%$  of the total P<sub>2</sub> flux on the side facet 4. Given the flux orientation illustrated in Figure 4.3d, this corresponds approximately to a shell thickness ratio (and thus P<sub>2</sub> flux ratio) of 3:2:1 on facets 4:(3 and 5):(1,2 and 6) in Figure 4.3e,f. We note that Ramdani et al.<sup>39</sup> and Küpers et al.<sup>40</sup> reported a similar contribution from scattered As flux incident on isolated GaAs nanowires during MBE growth. The close agreement with the measured

shell growth around the nanowire supports the assumption of an In diffusion length considerably larger than the nanowire cross-sectional dimension. However, we expect that as the group V flux increases, the diffusion length of In adatoms will decrease.<sup>27-29</sup> If the In diffusion length becomes comparable to or smaller than the nanowire circumference, the growth will begin to favor the In-facing facets, as is the case at 210 °C.<sup>3</sup>

The height along the nanowire length at which the cross section was taken does not impact the 3:2:1 flux distribution ratio. It is expected that the re-evaporated flux follows a standard cosine distribution. By symmetry, for an isolated straight nanowire the scattered flux is independent of the height above the surface (nanowire length). The present nanowires were grown in low density, such that the neighboring nanowires were not expected to impact the flux scattering (by producing or blocking re-evaporation). We note that the projected flux angles will change throughout the growth as the nanowire bends,<sup>3</sup> which will have some effect on the incident fluxes. However, while the absolute  $P_2$  flux incident on a highly bent nanowire can vary considerably along the nanowire length,<sup>3</sup> we expect shell thickness variations along the nanowire to be considerably less than the variation in the  $P_2$  flux. Specifically, referring to the nanowire in Figure 4.3e, as the nanowire bends, the ratio of the direct  $P_2$  flux will remain 2:1:0 on facets 4:(3 and 5):(1,2 and 6), respectively (assuming the nanowire does not bend completely over to shadow itself). Furthermore, as the nanowire bends, the increase in the direct flux on  $P_2$  source-facing facets is balanced by a relative increase in the scattered  $P_2$  flux incident on the other facets, thus approximately maintaining the 3:2:1 total  $P_2$  flux ratio and thus

the shell thickness ratio. Consequently, we expect group V controlled growth to increase shell uniformity along the nanowire compared to group III diffusion-limited growth. A full modeling of the impact of bending is not provided here, as the nanowires are not highly bent and the present findings are well explained by neglecting this perturbation on the shell growth.

The sum of the growth rates on all side facets is equal to a constant,  $G$ , which is proportional to the incident  $I_n$  flux:

$$G = \sum_{s=1}^6 \frac{\partial g_s}{\partial t} \quad (4.2)$$

From eqs 4.1 and 4.2, we can express the side facet growth rate as

$$\frac{\partial g_s}{\partial t} = G \frac{F_{P,s}}{\sum_{s=1}^6 F_{P,s}} \quad (4.3)$$

We note that for the  $P_2$ -rich conditions used in this study, the total growth is limited by the incident  $I_n$  flux. The  $P_2$  flux determines the relative distribution around the six side facets. In this growth mode, moderate variations in the  $P_2$  flux are not expected to impact the relative  $P_2$  flux (and, hence, growth) on the individual side facets. However, it is possible that dramatically increasing the V/III flux ratio could limit diffusion, thus impacting the distribution of growth.

Pair shadowing occurs when one nanowire blocks a unidirectional flux from reaching its neighbor. Recently, we reported group III shadowing effects in III–V nanowires.<sup>3</sup> In that work, we modeled shadowing for a perfectly aligned unidirectional beam. To explore the shadowing effect in the context of the  $P_2$ -mediated InP shell growth revealed above, growths were performed with the nanowire pairs aligned along the  $P_2$  beam. Shadowing also provides a means to vary the incident group V flux distribution around the nanowire cross section and thus validate the above conclusions about the growth process.

Figure 4.4a presents SEM images of nanowire pairs with varying spacings grown with incident  $P_2$  flux from the right, resulting in the partial shadowing of the direct  $P_2$  flux for the left-hand nanowires. The shell growth temperature was 440 °C for a planar deposition of 9 nm. For each pair, both nanowires are exposed to the same In beam incident at an azimuthal angle of 108° from the  $P_2$  beam. For these growth conditions, we observe that pairs spaced by 0.2 and 0.6  $\mu\text{m}$  at the base of the nanowire can be in contact (Figure 4.4a). It is noted that contact between pairs impacts bending and results in some pair-to-pair irregularities, presumably due to slight misalignments. The observed nanowire contacting is a consequence of the decrease in bending from the shadowed nanowire of the pairs, observed for these spacings. The shadowed nanowire experiences less asymmetric growth from the obstruction of the  $P_2$  beam—in the ideal case of perfect shadowing, only receiving the uniform scattered  $P_2$  flux on all sidewall facets. The efficacy of pair connections is strongly related to spacing. For pairs spaced by 0.2  $\mu\text{m}$ , 86% of the observed pairs were found to be connected. The connection efficacy decreases to 24% for pairs spaced by 0.6  $\mu\text{m}$  as the nanowire alignment must be precise to result in

connection for further spaced pairs. Pairs greater than  $1.2\ \mu\text{m}$  do not contact after bending or exhibit decreased bending due to shadowing (Figure 4.4a). As the pair spacing increases, less of the nanowire is shadowed (only the lower portion). For an incident  $P_2$  inclination angle of  $\theta$  ( $33.5^\circ$  here), no part of the nanowire will be shadowed if the spacing is  $>L \tan \theta$ , where  $L$  is the nanowire length.

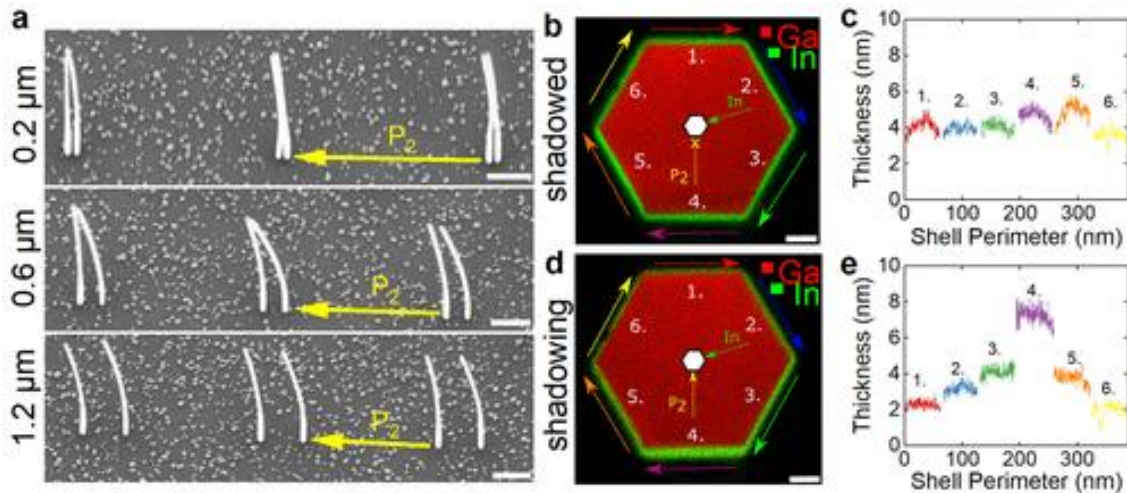


**Figure 4.4.** Nanowire pairs. (a) SEM images of nanowire pairs with shells grown at  $440\ ^\circ\text{C}$  imaged at a tilt of  $30^\circ$ . The pairs are aligned in the  $P_2$  beam direction (incident from the right). Pairs are spaced base-to-base by  $0.2$ ,  $0.6$ , and  $1.2\ \mu\text{m}$ . Scale bars for (a) are  $1\ \mu\text{m}$ , and yellow arrows indicate the  $P_2$  flux direction. (b, d) Net intensity EDS maps of a microtome cross section of a shadowed nanowire (b) and shadowing nanowire (d) of a pair separated by  $0.6\ \mu\text{m}$  at the base of the nanowire with shells grown at  $380\ ^\circ\text{C}$ . (c, e) Shell thickness plots corresponding to (b) and (d). The direction of the direct  $P_2$  and In fluxes is indicated on the EDS maps. The yellow “x” in (b) indicates that the direct  $P_2$  flux is blocked from reaching the nanowire. The color and numbering of the EDS line scans correspond to the labels on the EDS maps, indicating the path around the nanowire shell. Scale bars are  $20\ \text{nm}$  for the EDS maps.

Microtome nanowire cross sections of nanowire pairs were characterized by TEM and

EDS. Figure 4.4b,c shows EDS maps of a nanowire pair with a shell growth temperature

of 380 °C and pair separation of 0.6  $\mu\text{m}$  between the bases of the pairs. The actual separation distance observed in TEM was 0.35  $\mu\text{m}$ —a consequence of the nanowires being bent toward one another and suggesting the microtome slice was taken from near the midsection along the nanowire length. The unshadowed nanowire (Figure 4.4d,e) exhibits a shell thickness distribution that is nearly identical with the isolated nanowire in Figure 4.3e,f, with the shell growth occurring mostly on the  $P_2$ -facing facets in the manner discussed earlier. This is expected, as the unshadowed nanowires experience the same incident  $I_n$  and  $P_2$  fluxes. In contrast, the shadowed nanowire of the pair in Figure 4.4b exhibits a relatively symmetric shell of approximately 5 nm thickness. This is entirely consistent with the six sidewalls receiving only the symmetric scattered  $P_2$  flux—the direct beam being shadowed. These results are fully consistent with the above result that the relative growth rate is proportional to the total incident  $P_2$  flux on each facet. Furthermore, the total shell area measured from the cross sections is nearly equal for both nanowires,  $1420 \pm 190 \text{ nm}^2$  for the unshadowed nanowire and  $1490 \pm 200 \text{ nm}^2$  for the shadowed nanowire, which is expected as the total shell growth is limited by the  $I_n$  flux for these group V rich growth conditions, which is the same on both nanowires. Thus, the assumption of a symmetric phosphorus scattering flux is experimentally confirmed by the shadowing of the  $P_2$  beam and the resulting symmetric shell.

Lastly, we explore the connection between nanowire pairs. Figure 4.5 displays TEM micrographs and EDS maps for three pairs initially separated by 0.2  $\mu\text{m}$  and connected during shell growth at 380 °C. These images were chosen to represent the different

morphologies observed for connected pairs. For all three pairs, the nanowires appear to be intimately fused together. Figure 4.5a shows a phase-contrast TEM micrograph of a fused pair with a higher magnification image of the connection region shown in Figure 4.5b. The boundary between the fused pair exhibits contrast variations—possibly a result of strain or dislocations. Figure 4.5c presents a bright-field image of a second fused pair with a large amount of shell growth between the two cores, especially above the pair. A HAADF TEM micrograph of a third connected pair is shown in Figure 4.5d, where the InP shell appears brighter compared with the GaAs core. This is confirmed by the EDS map from the same nanowire pair presented in Figure 4.5e. We note that for all the connected pairs InP growth is concentrated in the concave regions above and below the interface between the pairs. This is in contrast to the above findings, where the growth is dictated by the relative  $P_2$  flux on a facet. The reason for this different shell geometry is unknown. However, we note that filling in the concave regions would reduce the total surface area, suggesting surface energy minimization as a possible driving force. Alternatively, strain-relieving defects at the interface between the two nanowires may act as a catalyst for InP crystal growth. The EDS image reveals that the two cores are separated by an  $\sim 2$  nm InP layer—in general, this thickness is expected to depend on the pair separation and the position along the nanowire length.

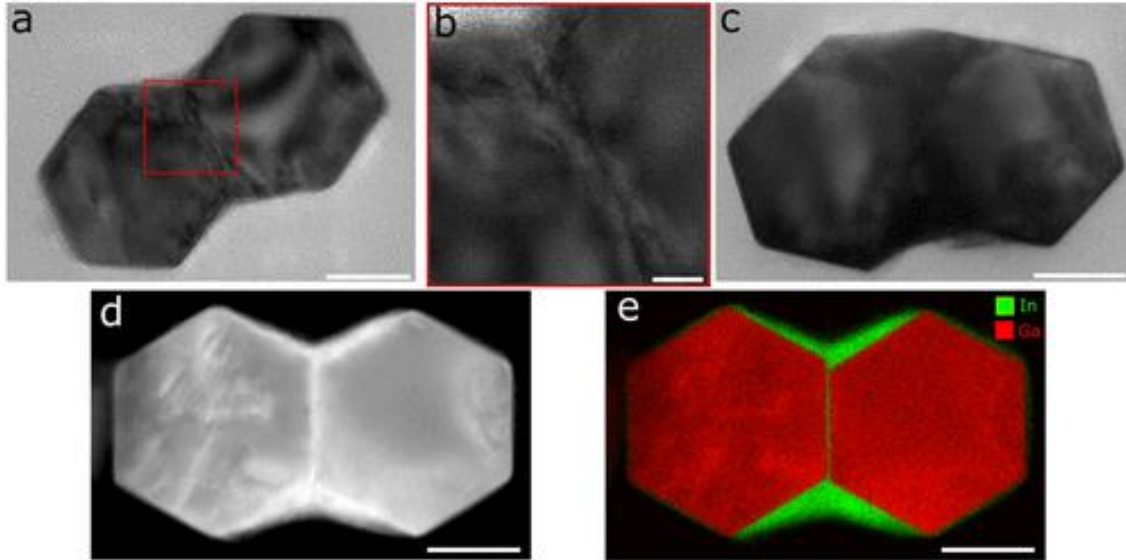


**Figure 4.5.** TEM characterization of fused nanowire pairs. (a) Phase-contrast TEM micrograph of a fused nanowire pair. (b) High-magnification image of the interface region indicated by the red box in (a). (c) Bright-field micrograph of a second connected pair. (d, e) HAADF image (d) and corresponding EDS map (e) of Ga (red) and In (green) for a third connected nanowire pair. Scale bars are 50 nm in parts (a, c, d, and e) and 10 nm in (b).

## 4.5 Conclusion

In summary, the symmetry and thus bending of nanowires with asymmetric lattice-mismatched shells are critically dependent on the adatom diffusion on the nanowire sidewalls during shell formation. InP shell growth was studied under two regimes: a low temperature, In diffusion limited regime, where growth favors facets receiving direct In impingement, and a high temperature, high In diffusion regime, where the growth on a facet is linearly proportional to the incident  $P_2$  flux—comprising the directional source

flux and an isotropic re-evaporation flux (approximately 50% of the direct source flux). These results are consistent with established planar GaAs growth kinetics and have important implications for nanowire shell growth and the development of prospective nanowire devices. The group V controlled growth regime was employed to quantify nanowire pair shadowing and to bend nanowires together to form connected arches—structures that are of high interest for nanowire chemical sensors and interconnects. Connected nanowires were found to form an intimate contact, which is highly encouraging for electrical conductivity between these structures and related prospective devices. This detailed understanding of 3D nanoepitaxy elucidates important processes that can be employed in fabrication of novel 3D nanostructures of other materials and will help pave the way for bottom-up, scalable fabrication of nanowire sensors based on bent nanowires.

### **Supporting Information**

Supporting information is provided by ACS Applied Nano Materials free of charge at <https://pubs-acsc-org.libaccess.lib.mcmaster.ca/doi/10.1021/acsanm.3c05235> or provided in appendix.

## References

- (1) Hilse, M.; Takagaki, Y.; Herfort, J.; Ramsteiner, M.; Herrmann, C.; Breuer, S.; Geelhaar, L.; Riechert, H. Ferromagnet-Semiconductor Nanowire Coaxial Heterostructures Grown by Molecular-Beam Epitaxy. *Appl. Phys. Lett.* 2009, 95 (13), 133126, DOI: 10.1063/1.3240405
- (2) Lewis, R. B.; Corfdir, P.; KüPers, H.; Flissikowski, T.; Brandt, O.; Geelhaar, L. Nanowires Bending over Backward from Strain Partitioning in Asymmetric Core-Shell Heterostructures. *Nano Lett.* 2018, 18 (4), 2343–2350, DOI: 10.1021/acs.nanolett.7b05221
- (3) McDermott, S.; Lewis, R. B. Bending of GaAs–InP Core–Shell Nanowires by Asymmetric Shell Deposition: Implications for Sensors. *ACS Appl. Nano Mater.* 2021, 4, 10164, DOI: 10.1021/acsanm.1c01636
- (4) Al-Humaidi, M.; Feigl, L.; Jakob, J.; Schroth, P.; Alhassan, A.; Davtyan, A.; Herranz, J.; Anjum, T.; Novikov, D.; Francoual, S.; Geelhaar, L.; Baumbach, T.; Pietsch, U. Situ X-Ray Analysis of Misfit Strain and Curvature of Bent Polytypic GaAs-In<sub>x</sub>Ga<sub>1-x</sub>As Core-Shell Nanowires. *Nanotechnology* 2022, 33 (1), 015601, DOI: 10.1088/1361-6528/ac29d8
- (5) Al-Humaidi, M. Al; Jakob, J.; Al Hassan, A.; Davtyan, A.; Schroth, P.; Feigl, L.; Herranz, J.; Novikov, D.; Geelhaar, L.; Baumbach, T.; Pietsch, U. Exploiting of Flux Shadowing Effect on In<sub>x</sub>Ga<sub>1-x</sub>As Asymmetric Shell Growth for Strain and Bending Engineering in GaAs - In<sub>x</sub>Ga<sub>1-x</sub>As Core - Shell NW Arrays, 2022. DOI: 10.48550/arXiv.2203.04073.

- (6) Kryvyi, S.; Kret, S.; Domagala, J.; Wojnar, P. Reconstruction of Three-Dimensional Strain Field in an Asymmetrical Curved Core-Shell Hetero-Nanowire. *Nanotechnology* 2023, 34, 445705, DOI: 10.1088/1361-6528/acebf6
- (7) Greenberg, Y.; Kelrich, A.; Cohen, S.; Kar-Narayan, S.; Ritter, D.; Calahorra, Y. Strain-Mediated Bending of InP Nanowires through the Growth of an Asymmetric InAs Shell. *Nanomaterials* 2019, 9 (9), 1–11, DOI: 10.3390/nano9091327
- (8) Bjergfelt, M.; Carrad, D. J.; Kanne, T.; Aagesen, M.; Fiordaliso, E. M.; Johnson, E. Superconducting Vanadium/Indium-Arsenide Hybrid Nanowires. *Nanotechnology* 2019, 30 (29), 294005, DOI: 10.1088/1361-6528/ab15fc
- (9) Krogstrup, P.; Ziino, N. L. B.; Chang, W.; Albrecht, S. M.; Madsen, M. H.; Johnson, E.; Nygård, J.; Marcus, C. M.; Jespersen, T. S. Epitaxy of Semiconductor-Superconductor Nanowires. *Nat. Mater.* 2015, 14 (4), 400–406, DOI: 10.1038/nmat4176
- (10) Xu, Y.; Li, L.; Zang, Y.; Hu, J.; Li, Z.; Chen, H.; Zhang, G.; Xia, C.; Cho, J. Forward Bending of Silicon Nanowires Induced by Strain Distribution in Asymmetric Growth. *Mater. Lett.* 2021, 297, 129929 DOI: 10.1016/j.matlet.2021.129929
- (11) Keplinger, M.; Kriegner, D.; Stangl, J.; Mårtensson, T.; Mandl, B.; Wintersberger, E.; Bauer, G. Core-Shell Nanowires: From the Ensemble to Single-Wire Characterization. *Nucl. Instrum Methods Phys. Res. B* 2010, 268 (3–4), 316–319, DOI: 10.1016/j.nimb.2009.09.043

- (12) Wallentin, J.; Jacobsson, D.; Osterhoff, M.; Borgström, M. T.; Salditt, T. Bending and Twisting Lattice Tilt in Strained Core-Shell Nanowires Revealed by Nanofocused X-Ray Diffraction. *Nano Lett.* 2017, 17 (7), 4143–4150, DOI: 10.1021/acs.nanolett.7b00918
- (13) Gagliano, L.; Albani, M.; Verheijen, M. A.; Bakkers, E. P. A. M.; Miglio, L. Twofold Origin of Strain-Induced Bending in Core-Shell Nanowires: The GaP/InGaP Case. *Nanotechnology* 2018, 29 (31), 315703, DOI: 10.1088/1361-6528/aac417
- (14) Davtyan, A.; Kriegner, D.; Holý, V.; AlHassan, A.; Lewis, R. B.; McDermott, S.; Geelhaar, L.; Bahrami, D.; Anjum, T.; Ren, Z.; Richter, C.; Novikov, D.; Müller, J.; Butz, B.; Pietsch, U. X-Ray Diffraction Reveals the Amount of Strain and Homogeneity of Extremely Bent Single Nanowires. *J. Appl. Crystallogr.* 2020, 53 (111), 1310–1320, DOI: 10.1107/S1600576720011516
- (15) Yao, X.; Zhang, X.; Sun, Q.; Wei, D.; Chen, P.; Zou, J. Anomalous Photoelectrical Properties through Strain Engineering Based on a Single Bent InAsSb Nanowire. *ACS Appl. Mater. Interfaces* 2021, 13 (4), 5691–5698, DOI: 10.1021/acsami.0c16028
- (16) Day, R. W.; Mankin, M. N.; Lieber, C. M. Plateau-Rayleigh Crystal Growth of Nanowire Heterostructures: Strain-Modified Surface Chemistry and Morphological Control in One, Two, and Three Dimensions. *Nano Lett.* 2016, 16 (4), 2830–2836, DOI: 10.1021/acs.nanolett.6b00629

- (17) Hetzl, M.; Winnerl, J.; Francaviglia, L.; Kraut, M.; Döblinger, M.; Matich, S.; FontcubertaMorral, A.; Stutzmann, M. Surface Passivation and Self-Regulated Shell Growth in Selective Area-Grown GaN-(Al,Ga)N Core-Shell Nanowires. *Nanoscale* 2017, 9 (21), 7179–7188, DOI: 10.1039/C7NR00802C
- (18) Zhao, Y.; Yao, J.; Xu, L.; Mankin, M. N.; Zhu, Y.; Wu, H.; Mai, L.; Zhang, Q.; Lieber, C. M. Shape-Controlled Deterministic Assembly of Nanowires. *Nano Lett.* 2016, 16 (4), 2644–2650, DOI: 10.1021/acs.nanolett.6b00292
- (19) Janissen, R.; Sahoo, P. K.; Santos, C. A.; Da Silva, A. M.; Von Zuben, A. A. G.; Souto, D. E. P.; Costa, A. D. T.; Celedon, P.; Zanchin, N. I. T.; Almeida, D. B.; Oliveira, D. S.; Kubota, L. T.; Cesar, C. L.; Souza, A. P. D.; Cotta, M. A. InP Nanowire Biosensor with Tailored Biofunctionalization: Ultrasensitive and Highly Selective Disease Biomarker Detection. *Nano Lett.* 2017, 17 (10), 5938–5949, DOI: 10.1021/acs.nanolett.7b01803
- (20) Bai, M.; Huang, H.; Liu, Z.; Zhan, T.; Xia, S.; Li, X.; Sibirev, N.; Bouravleuv, A.; Dubrovskii, V. G.; Cirilin, G. InAs/InP Core/Shell Nanowire Gas Sensor: Effects of InP Shell on Sensitivity and Long-Term Stability. *Appl. Surf. Sci.* 2019, 498, 143756, DOI: 10.1016/j.apsusc.2019.143756
- (21) Lim, Y.; Kim, S.; Kwon, Y. M.; Baik, J. M.; Shin, H. A Highly Sensitive Gas-Sensing Platform Based on a Metal-Oxide Nanowire Forest Grown on a Suspended Carbon Nanowire Fabricated at a Wafer Level. *Sens Actuators B Chem.* 2018, 260, 55–62, DOI: 10.1016/j.snb.2017.12.167

- (22) Choi, J.; Kim, J. Highly Sensitive Hydrogen Sensor Based on Suspended, Functionalized Single Tungsten Nanowire Bridge. *Sens Actuators B Chem.* 2009, 136 (1), 92–98, DOI: 10.1016/j.snb.2008.10.046
- (23) Lim, Y.; Lee, Y.; Lee, J.; Shin, H. Circumferentially Grown ZnO Nanowire Forest on a Suspended Carbon Nanowire for a Highly Sensitive Gas Sensor, 2015; Vol. MEMS 2015 28th.
- (24) Lim, Y.; Lee, Y.; Heo, J. Il; Shin, H. Highly Sensitive Hydrogen Gas Sensor Based on a Suspended Palladium/Carbon Nanowire Fabricated via Batch Microfabrication Processes. *Sens Actuators B Chem.* 2015, 210, 218–224, DOI: 10.1016/j.snb.2014.12.109
- (25) Baek, D. H.; Choi, J.; Kim, J. Fabrication of Suspended Nanowires for Highly Sensitive Gas Sensing. *Sens Actuators B Chem.* 2019, 284, 362–368, DOI: 10.1016/j.snb.2018.12.159
- (26) Cheng, Z.; Li, Q.; Li, Z.; Zhou, Q.; Fang, Y. Suspended Graphene Sensors with Improved Signal and Reduced Noise. *Nano Lett.* 2010, 10 (5), 1864–1868, DOI: 10.1021/nl100633g
- (27) Nishinaga, T.; Shen, X. Q.; Kishimoto, D. Surface Diffusion Length of Cation Incorporation Studied by Microprobe-RHEED/SEM MBE. *J. Cryst. Growth* 1996, 163 (1–2), 60–66, DOI: 10.1016/0022-0248(95)01050-5
- (28) Yamashiki, A.; Nishinaga, T. Arsenic Pressure Dependence of Incorporation Diffusion Length on (0 0 1) and (1 1 0) Surfaces and Inter-Surface Diffusion in

- MBE of GaAs. *J. Cryst. Growth* 1999, 198, 1125–1129, DOI: 10.1016/S0022-0248(98)01135-X
- (29) Ogura, T.; Nishinaga, T. Efficiency Difference in Ga Adatom Incorporation in MBE Growth of GaAs with As<sub>2</sub> and As<sub>4</sub> Molecular Beams. *J. Cryst. Growth* 2000, 211, 416–420, DOI: 10.1016/S0022-0248(99)00804-0
- (30) Arciprete, F.; Placidi, E.; Magri, R.; Fanfoni, M.; Balzarotti, A.; Patella, F. The Unexpected Role of Arsenic in Driving the Selective Growth of InAs Quantum Dots on GaAs. *ACS Nano* 2013, 7 (5), 3868–3875, DOI: 10.1021/nn401338v
- (31) Arciprete, F.; Placidi, E.; Magri, R.; Del Gaudio, D.; Patella, F. Kinetically Driven Selective Growth of InAs Quantum Dots on GaAs. *J. Mater. Res.* 2013, 28 (23), 3201–3209, DOI: 10.1557/jmr.2013.340
- (32) Magri, R.; Placidi, E.; Arciprete, F.; Patella, F. Selective Growth of InAs Quantum Dots on GaAs Driven by as Kinetics. In *Crystal Research and Technology*; Wiley-VCH Verlag: 2014; Vol. 49, pp 546–551.
- (33) Placidi, E.; Arciprete, F.; Sarti, F.; Gurioli, M.; Vinattieri, A.; Patella, F. Single QD Emission from Arrays of QD Chains Obtained by Patterning-Free Method. *Advanced Device Materials* 2015, 1 (1), 33–37, DOI: 10.1179/2055031614Y.0000000007
- (34) Lewis, R. B.; Nicolai, L.; KüPers, H.; Ramsteiner, M.; Trampert, A.; Geelhaar, L. Anomalous Strain Relaxation in Core-Shell Nanowire Heterostructures via Simultaneous Coherent and Incoherent Growth. *Nano Lett.* 2017, 17 (1), 136–142, DOI: 10.1021/acs.nanolett.6b03681

- (35) Goldthorpe, I. A.; Marshall, A. F.; McIntyre, P. C. Synthesis and Strain Relaxation of Ge-Core/Si-Shell Nanowire Arrays. *Nano Lett.* 2008, 8 (11), 4081–4086, DOI: 10.1021/nl802408y
- (36) Dayeh, S. A.; Tang, W.; Boioli, F.; Kavanagh, K. L.; Zheng, H.; Wang, J.; Mack, N. H.; Swadener, G.; Huang, J. Y.; Miglio, L.; Tu, K. N.; Picraux, S. T. Direct Measurement of Coherency Limits for Strain Relaxation in Heteroepitaxial Core/Shell Nanowires. *Nano Lett.* 2013, 13 (5), 1869–1876, DOI: 10.1021/nl3022434
- (37) Ni, Y.; He, L. H.; Liao, X. B. Stress Anisotropy Controlled Morphological Evolution in Core–Shell Nanowires. *Extreme Mech Lett.* 2016, 8, 160–166, DOI: 10.1016/j.eml.2016.01.002
- (38) Dubrovskii, V. G.; Glas, F. Vapor–Liquid–Solid Growth of Semiconductor Nanowires. In *Fundamental Properties of Semiconductor Nanowires*; Fukata, N., Rurali, R., Eds.; Springer: Singapore, 2021.
- (39) Ramdani, M. R.; Harmand, J. C.; Glas, F.; Patriarche, G.; Travers, L. Arsenic Pathways in Self-Catalyzed Growth of GaAs Nanowires. *Cryst. Growth Des* 2013, 13 (1), 91–96, DOI: 10.1021/cg301167g
- (40) KüPers, H.; Lewis, R. B.; Tahraoui, A.; Matalla, M.; Krüger, O.; Bastiman, F.; Riechert, H.; Geelhaar, L. Diameter Evolution of Selective Area Grown Ga-Assisted GaAs Nanowires. *Nano Res.* 2018, 11 (5), 2885–2893, DOI: 10.1007/s12274-018-1984-1

## **Chapter 5**

# **Electron Microscopy Study of the Effect of Cross-section Orientation on Directional Growth**

## **5.1 To Be Submitted: Electron Microscopy Study of Core–Shell Nanowire Bending and Twisting**

**Electron Microscopy Study of Core–Shell Nanowire Bending and Twisting**

Authors: Spencer McDermott, Trevor R. Smith, and Ryan B. Lewis

**Manuscript awaits submission to a journal.**

## 5.2 Introduction

Bent nanowire heterostructures have garnered significant interest for sensors due to their scalable fabrication and the advantageous out-of-plane sensor geometry. To leverage bending for the mass production of nanowire devices, the fabrication processes must be well understood. Asymmetric core-shell nanowire heterostructures have been grown by physical vapor deposition processes—molecular beam epitaxy (MBE)<sup>1-10</sup> and electron beam evaporation<sup>11-14</sup>—as well as chemical vapor deposition with metal-organic MBE.<sup>15</sup> Nanowires are normally faceted to minimize surface energy<sup>16-18</sup>, whereby both zinc-blende and wurtzite lattices can feature a hexagonal cross-section terminated at  $\{1\bar{1}0\}$  and  $m$ -plane facets, respectively. Due to their non-cylindrical shape, equivalent directional deposition processes with fluxes incident on different nanowire crystallographic orientations can result in differing cross-sections and shell distributions.<sup>2,6,9,10</sup> The modeling of bending phenomena often assumes a cylindrical geometry,<sup>15,19,20</sup> but the actual faceted geometries for crystalline nanowires have also been modeled.<sup>4,21-24</sup> Furthermore, nanowire twisting has been observed in nanowires on occasion,<sup>7,25,26</sup> but the reason why some nanowires exhibit twisting while others do not is still unclear. Thus, further investigation is needed to determine the role of the cross-sectional orientation for directional nanoepitaxy of bent nanowires.

Cross-sectional transmission electron microscopy (TEM) characterization of nanowire heterostructures has been carried out on nanowire sections prepared by microtomy<sup>9,27,28</sup> and focused ion beam (FIB) milling,<sup>6,10,23,29,30</sup> allowing for characterization of the core-shell interface, shell distribution, and asymmetry in the distribution. Atom probe tomography<sup>31-33</sup> offers high three-dimensional (3D) spatial and compositional resolution; however, it has constraints concerning the size and shape of nanowires that can be examined—one of which is the requirement for straight nanowires. Electron tomography utilizing scanning transmission electron microscopy (STEM) with energy-dispersive X-ray spectroscopy (EDS) or electron energy loss spectroscopy (EELS) in combination with a specialized tomography holder allows for conventional tomography of heterostructures.<sup>34-36</sup> The necessity of the specialized holder arises due to the requirement for numerous (time-consuming) scans across a broad range of angles.<sup>37</sup> However, reconstruction techniques can help reduce the required angular scan range and the number of scans. For example, the knowledge of faceting geometry in crystalline nanomaterials has been employed to reconstruct 3D nanomaterials<sup>38,39</sup> and cross-sections along nanowires.<sup>7,40-43</sup> In bent nanowires, bending variations along the nanowire can occur due to variations in core or shell geometry.<sup>3,7,25,26,44</sup> To explain nanowires with twisting or bending, it is crucial to understand the local cross-section along the nanowire.

In this paper, we investigate the influence of shell deposition orientation on the bending behavior and shell distribution of asymmetric core-shell nanowires. GaAs-InP core-shell nanowires are synthesized using phosphorus-controlled nanoepitaxy with gas-source MBE.<sup>9</sup> Scanning electron microscopy (SEM) is employed to examine the nanowires' shape, bending, and side facet orientation. The orientation of the phosphorus beam with respect to the nanowire side facets induces variations in the nanowire shape, bending, and twisting. A practical analytical transmission electron tomography reconstruction technique is presented to characterize the nanowire shell distribution, which employs the hexagonal faceting to reconstruct the 3D profile. This method circumvents the 'missing wedge problem'.<sup>37</sup> requiring only two scans at moderately-separated tilt angles, resulting in an efficient approach to nanowire tomography and reducing beam damage. This technique is used to study the variations in core and shell along the length of bent nanowires. Two-dimensional (2D) cross-sectional distributions are generated from the STEM data and modeled with linear elastic theory. Nanowire twisting is observed in some nanowires and explained by the minimization of strain energy with respect to the shell distribution, which favors two shell orientations, symmetric about  $\langle 1\bar{1}0 \rangle$  and  $\langle 11\bar{2} \rangle$ , respectively.

### 5.3 Methods

GaAs–InP core–shell nanowires were grown on patterned Si (111) substrates by gas-source MBE. The substrates were prepared by first depositing 30 nm of SiO<sub>2</sub> via atomic layer deposition (ALD) with a FlexAL ALD cluster system. Next, a hole pattern in the oxide was created using electron beam lithography (EBL), where AR-P 6200.3:Anisole (1:1) e-beam resist was spun at 6000 rpm for 1 minute. The resist was soft baked at 150°C for 1 minute before undergoing EBL with a Raith EBPG 5000+ system. The pattern was then developed with ZED-N50, and reactive ion etching was used to transfer the pattern into the oxide. Immediately before loading the substrates into a SVTA-MBE35 MBE system, the substrates were immersed in a solution of 1 part Fujifilm Buffered Oxide Etchant 10:1 (NH<sub>4</sub>F:HF with Fujifilm surfactant) and 9 parts water for 28 seconds to remove native oxide from the hole pattern. GaAs–InP core–shell nanowire heterostructures were subsequently grown by MBE with solid-source effusion cells providing the gallium and indium. The V-sources, As<sub>2</sub> and P<sub>2</sub>, were introduced via Arsine and Phosphine gases thermally cracked at 1000 °C.

GaAs nanowire cores were synthesized via vapor-liquid-solid growth at a substrate temperature of 630 °C. A pre-deposition of Ga for 250 seconds was performed before initiating nanowire growth via the addition of an As<sub>2</sub> flux at a V:III ratio of 2. The GaAs planar growth rate was 0.125 μm/h. After 20 minutes of GaAs growth, the As<sub>2</sub> flux was increased to a V:III ratio of 5.6 and maintained for 1 hour, after which, the Ga flux was terminated and the conditions held for one minute to consume the Ga droplets before cooling and reducing the As<sub>2</sub> flux. The same core growth process was used for all samples. InP nanowire shells were subsequently deposited at a substrate temperature of 410 °C in the absence of substrate rotation, with the substrate oriented so that the P<sub>2</sub> source was incident at various angles relative to the nanowire facets. Shell growth was initiated by opening the In shutter at a planar InP growth rate of 0.25 μm/h with a V:III ratio of 10 for a duration of 130 seconds. The P<sub>2</sub> and In sources were separated by an azimuthal angle of 108°. The In shutter was closed to terminate the shell growth.

As-grown nanowire samples were examined in an FEI Magellan 400 SEM operating at an accelerating voltage of 1 kV and a current of 13 pA. The secondary electron signal was detected using an in-lens detector in immersion mode. The nanowires were imaged normal to the substrate and at a 30° tilt. Top-view images (normal to the substrate) were collected under a stage bias of 500 V. Transmission electron microscopy samples were prepared by ultrasonically cleaning as-grown samples in isopropyl alcohol for 2 minutes before drop casting on lacy carbon TEM grids. These samples were measured in a Talos F200X TEM with a X-FEG source equipped with a double tilt holder. Imaging was done in high-angle annular dark field (HAADF) STEM mode. EDS line scans were collected perpendicular to the nanowire's axial direction using four Super-X SDD in-column detectors. At each chosen location along the nanowire, two EDS scans were conducted, rotated by  $23 \pm 4^\circ$  about the nanowire axis. Velox by Thermo Fisher Scientific was used to analyze the net intensity of the K-shell for Ga and the L-shell for In in the nanowire heterostructure. Linear elastic modeling was conducted using MathWorks MATLAB to model curvature and strain energy for various core-shell distributions from different  $P_2$  beam orientations.

## 5.4 Results and Discussion

Figure 1 shows SEM images of GaAs-InP core-shell nanowires with shells grown under different substrate azimuthal orientations relative to the In and  $P_2$  sources. The nanowires show a significant difference in the amount of bending for different  $P_2$  beam alignments. Nanowires grown with the  $P_2$  beam incident along  $\langle 1\bar{1}0 \rangle$  ( $P_2$  beam alignment of  $0^\circ$ ,

c.f. Figure 1a) exhibit greater overall bending compared to samples grown with  $10^\circ$ ,  $20^\circ$ ,  $30^\circ$  deposition angles (c.f. Figure 1b-d, respectively). For all nanowires observed on the samples, the bending direction is approximately in line with the incident  $P_2$  beam direction, as previously reported.<sup>9</sup> The average curvature of the nanowires is plotted in Figure 1e, showing a monotonic decrease by about a factor of two as the deposition transitions from on the facet to on the edge between facets—from  $0^\circ$  to  $30^\circ$ . This illustrates a dramatic role of the flux orientation, not just for dictating the bending direction but also the amount of bending.

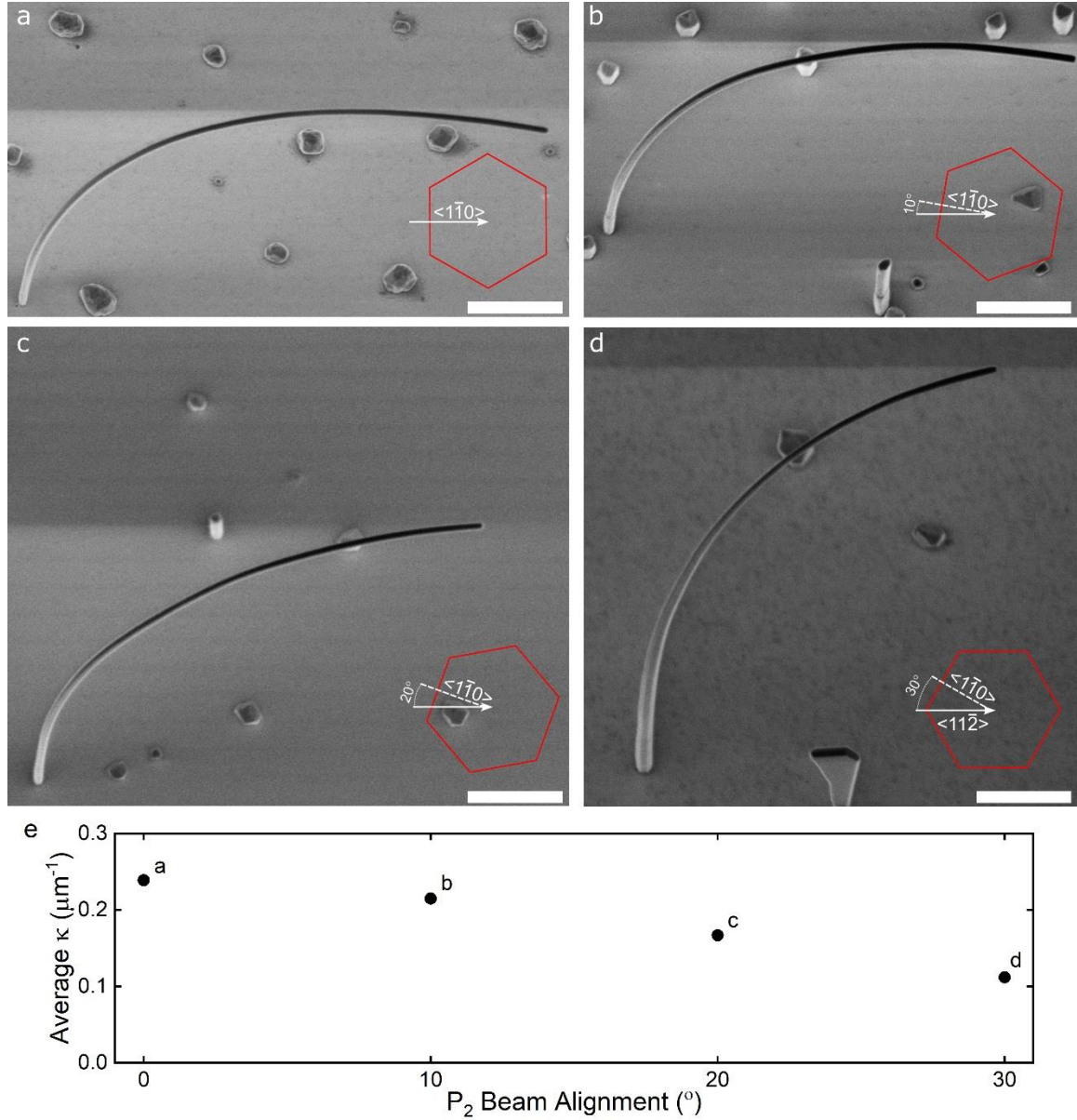


**Figure 5.1.** SEM images of core-shell nanowires with InP shells grown under various incident flux azimuthal angles. (a) Projected  $P_2$  beam along the  $\langle 1\bar{1}0 \rangle$  direction, (b–d)  $P_2$  beam offset from  $\langle 1\bar{1}0 \rangle$  by  $10^\circ$ ,  $20^\circ$  and  $30^\circ$ , respectively. Images are taken at a tilt of  $30^\circ$  from the substrate normal and the insets show the angle of the incident  $P_2$  beam with respect to the nanowire shape. All scale bars are  $1 \mu\text{m}$ . (e) Average curvatures measured in (a–d) plotted with respect to  $P_2$  beam alignment relative to  $\langle 1\bar{1}0 \rangle$ .

Figure 2 presents top-view, high-magnification SEM images of the four samples shown in Fig. 1. Magnified views are shown of the base, mid-section and tip of each wire, where the dashed lines indicate the intersection of side facets. In Figure 2a— $P_2$  beam alignment along  $\langle 1\bar{1}0 \rangle$ —no twisting is observed with side facets exhibiting a consistent orientation of  $\langle 1\bar{1}0 \rangle$  at the base, middle and tip of the nanowire. For the nanowire with  $P_2$  beam offset by  $10^\circ$  (Figure 2b), the nanowire exhibits twisting. Specifically, at the base of the nanowire, the facet orientation is consistent with the expected bending/deposition direction, while the middle and tip of the nanowire indicate that the nanowire is rotated such that the  $\langle 11\bar{2} \rangle$  (intersection of the facets) is now in the middle of the nanowire (pointing up). Similarly, for the nanowire grown with a  $20^\circ$   $P_2$  beam offset (Figure 1c), the facet orientation mid-section and tip have  $\langle 11\bar{2} \rangle$  pointing up, contrasting the geometry at the base of the nanowire and thus indicating that twisting has occurred. The nanowire grown with a  $30^\circ$   $P_2$  beam offset (Figure 1d) exhibits no twisting and is bent along the  $\langle 11\bar{2} \rangle$  orientation from base to tip. For samples grown with  $10^\circ$  and  $20^\circ$   $P_2$  beam offsets, the nanowires twist such that the  $\langle 11\bar{2} \rangle$  points upward—corresponding to twist angles of  $20^\circ$  and  $10^\circ$ , respectively. Only the nanowire grown without a  $P_2$  beam offset shows bending along  $\langle 1\bar{1}0 \rangle$ . Thus, the nanowires aligned at  $0^\circ$  and  $30^\circ$  do not twist and the nanowires with at  $10^\circ$  and  $20^\circ$   $P_2$  beam direction twist to orient the  $\langle 11\bar{2} \rangle$  direction upward.

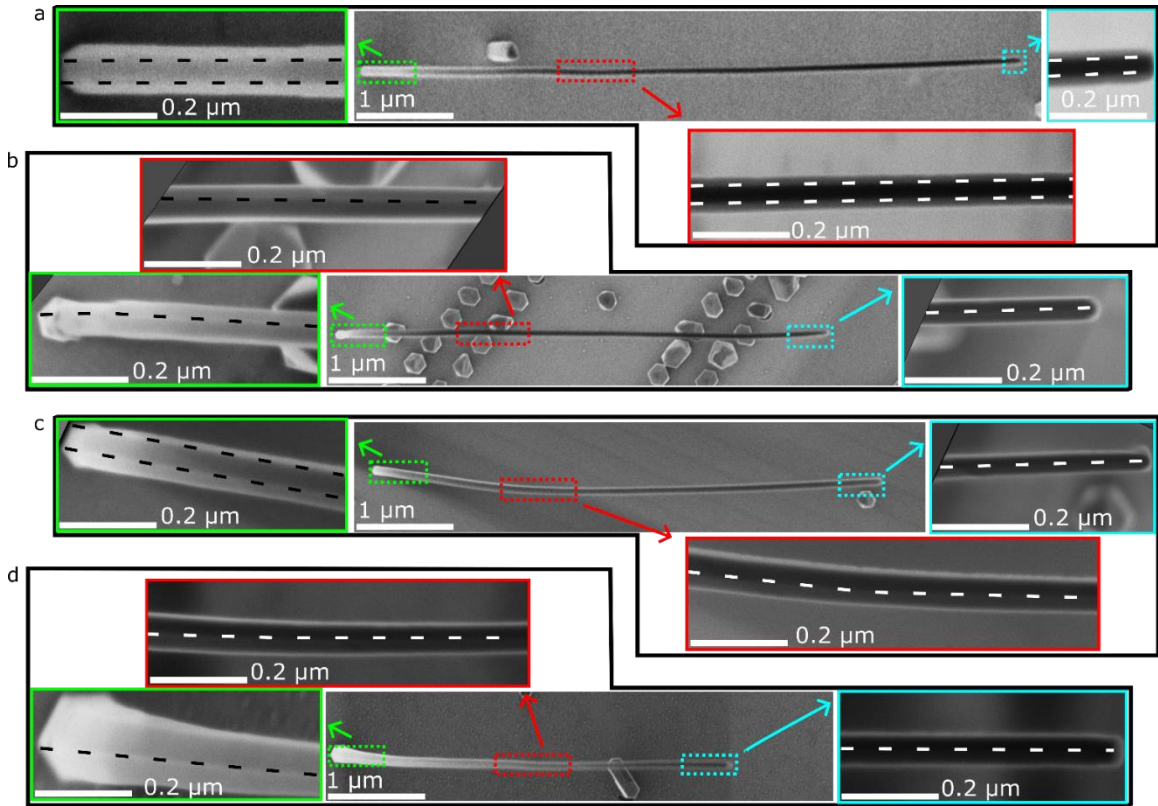


**Figure 5.2.** Top-view SEM Images of the bending series of Figure 1. Each sub-figure shows the nanowire in its entirety, along with three (5x) higher magnification images of the nanowire base (green), mid-section (red), and tip (cyan). The  $P_2$  beam alignment in (a) is along the  $\langle 1\bar{1}0 \rangle$  direction and (b), (c), (d) are offset by  $10^\circ$ ,  $20^\circ$ , and  $30^\circ$ , respectively. Black and white dashed lines denote the intersection of  $\{1\bar{1}0\}$  side facets.

To quantify the core and shell distribution along the nanowire length, we developed a STEM tomographic method to reconstruct the core-shell geometry based on pairs of EDS lines scans collected at two different tilt angles about the nanowire axis. The STEM image in Figure 3a shows a nanowire grown with  $P_2$  beam incident at  $10^\circ$  from  $\langle 1\bar{1}0 \rangle$ , where EDS line scans are collected at ten segments along the length—shown as blue boxes. Each segment is measured at two angles, rotated by  $23 \pm 4^\circ$  around the nanowire

axis. This is significantly less than the number of scans and the angular range required for traditional tomography,<sup>37</sup> made possible by employing features known of nanowire geometry in the reconstruction—e.g., a hexagonal GaAs core, discussed below. Figures 3b and 3c show thickness profile reconstructions for a pair of scans at the same location along the nanowire. The EDS thickness profile reconstructions are created by assuming the faceting of the GaAs nanowire core— $\{1\bar{1}0\}$  facets terminating on the  $\langle 11\bar{2} \rangle$  direction—is preserved for the InP shell, as seen in McDermott et al.<sup>9</sup> To convert the Ga line scans into thickness profiles, we assume hexagonal cross-sections for the GaAs cores and project the cross-section at different angles to best match the line scans. The intensity is scaled to align with each profile for each cross-sectional orientation and the orientation with the highest coefficient of determination is chosen as the correct profile of the nanowire core. The resulting profiles are plotted in Figures 3b and 3c and further detailed in the Supporting Information (SI). To fit the shell profile, it is assumed that both core and shell share the same faceting, so the slope of the rising edge of the core and shell thickness profiles are equivalent, as seen in Figure 3b–c. By fitting the In profile in this manner, the shell thickness profile is determined (see SI for further details).

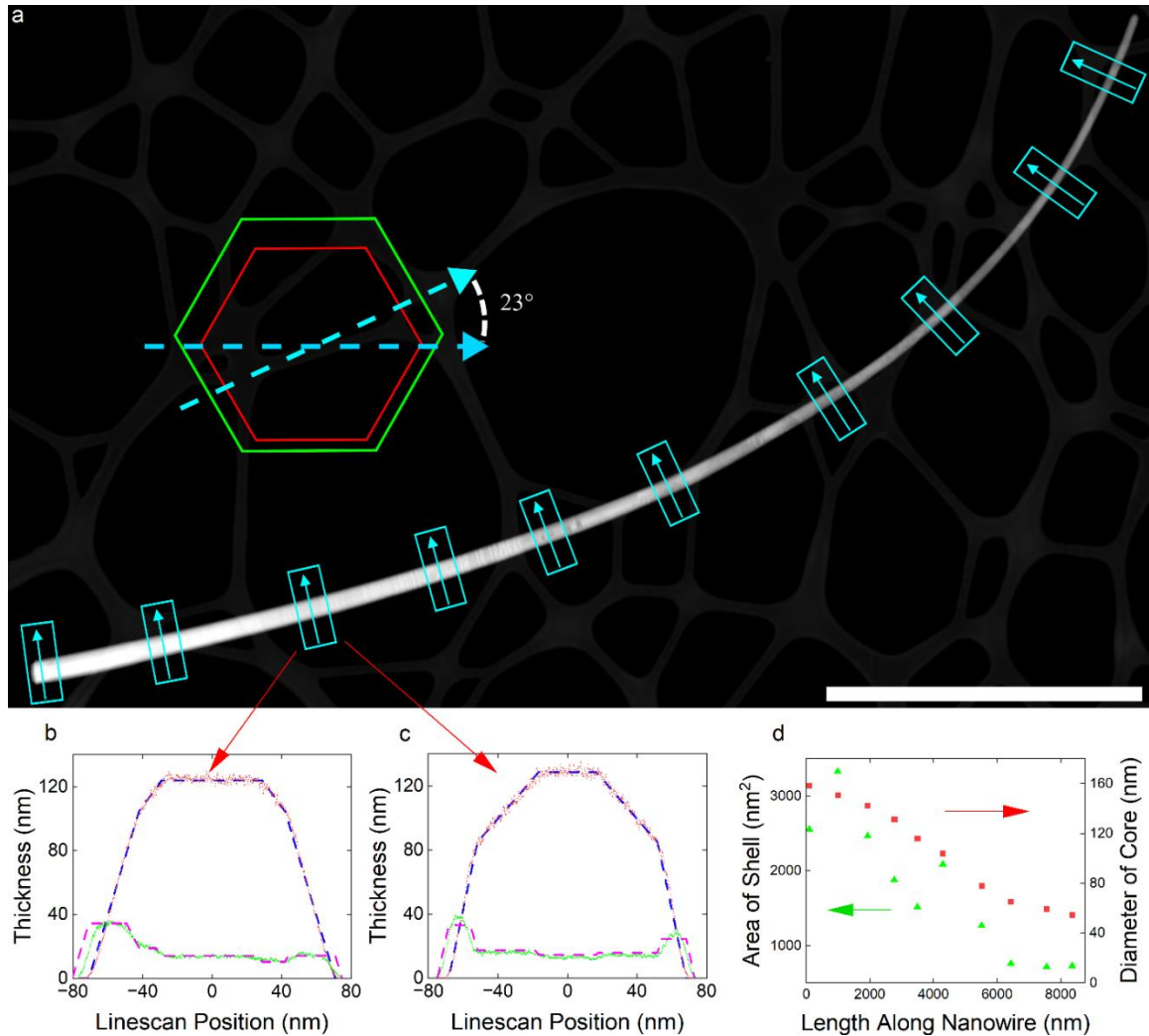


**Figure 5.3.** (a) Overview STEM image of a dispersed nanowire grown with incident  $\text{P}_2$  flux  $10^\circ$  offset to  $\langle 1\bar{1}0 \rangle$ . 10 EDS line scan pairs are displayed along the length, as indicated on the image by the blue arrow boxes. Pairs of scans are rotated by  $23 \pm 4^\circ$  about the nanowire axis, as illustrated in the top left corner of (a). The scale bar is  $2\ \mu\text{m}$ . (b–c) Exemplary thickness profiles extracted from a pair of EDS line scans. The blue and magenta dashed lines are the projection of the simulated core and shell, respectively. The EDS-measured core and shell data—scaled for appropriate thickness—are plotted in red (core) and green (shell). (d) Summary of measured diameter and shell area along the nanowire.

The 2D cross-sections are extracted from the EDS line profiles with three assumptions: 1) the shell is in contact with the nanowire core, 2) the compositions of the core and shell are pure GaAs and InP, respectively, and 3) the shell has  $\langle 1\bar{1}0 \rangle$  terminating facets that intersect to enclose the shell. A single thickness profile will have multiple solutions that are unbounded along the direction from which the thickness profile was taken. A second thickness profile is thus required to extract a unique 2D cross-section with the above assumptions. To extract a profile, the unbounded shell profiles for each scan rotation are projected onto each other, where the best fit—projection with the highest coefficient of determination—is chosen as the 2D profile (see SI for details). As shown in Figure 3b–c, there is excellent agreement between the core-shell modeling (dashed lines) and the EDS line scan data for both imaging directions. The core diameter and shell area along the nanowire is plotted in Figure 3d, indicating the nanowire core is highly tapered, with the core diameter decreasing from 158 nm at the base to 54 nm at the tip. On average, the shell area also decreases from the base to the tip, from 3300 nm<sup>2</sup> to 700 nm<sup>2</sup>, respectively. The reduction in shell area is approximately proportional to the decrease in diameter, which is explained by the amount of In impinging per unit length being proportional to the nanowire diameter. It is noted that the maximum shell area is observed about 1 μm from the base and the decreasing area is not monotonic along the nanowire length.

The cross-sections reconstructed from the 10 EDS line scan pairs are displayed in Figures 4a–j. Averaging over all the segments, the two facets normal to 90° and 150° have relative shell thicknesses of 30.4±7.0% and 29.1±6.5% of the total thickness (summed of all facets), respectively. The opposite facets (normal to 270° and 330°) have relative shell

thicknesses of  $8.2 \pm 6.5\%$  and  $8.5 \pm 4.5\%$ , respectively. The symmetry of this average cross section the  $P_2$  direction was incident from  $118.5^\circ$  which is approximately aligned to the  $\langle 11\bar{2} \rangle$  orientation. This means the nanowire has twisted  $18.5^\circ$  from its initial orientation.

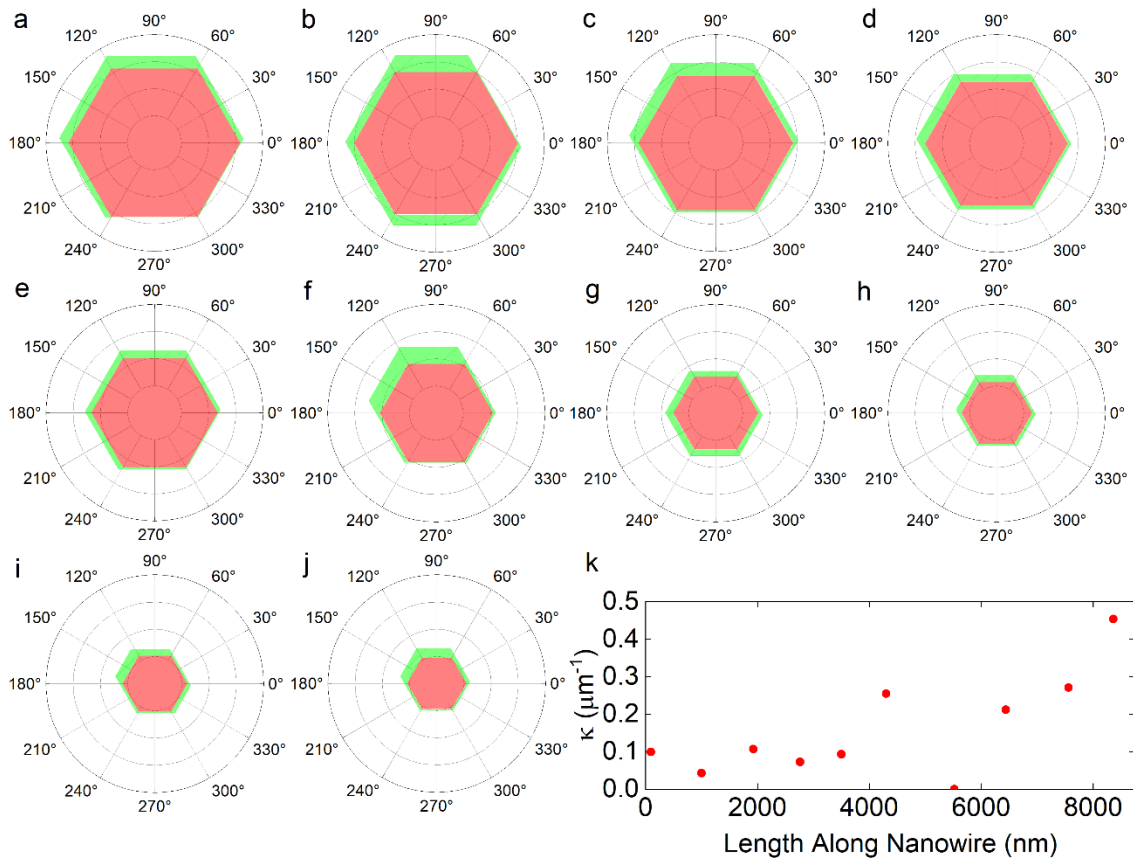


**Figure 5.4.** Extracted nanowire cross-sections from EDS measurements. The 10 cross-sections correspond to the 10 sections measured from the nanowire presented in Figure 3a, from base to tip (a–j). The red area corresponds to the GaAs core and the green area to the InP shell. The radial line spacing is 25 nm. (k) Linear-elastic-theory-predicted curvature ( $\kappa$ ) of the 10 cross-sections.

With the phosphorus beam incident from  $120^\circ$ , the two facets normal to  $270^\circ$  and  $330^\circ$  were shadowed from the  $P_2$  beam and only receive  $P_2$  flux from scattering—previously reported to be half of the direct beam flux.<sup>9,45,46</sup> Assuming the deposition to be proportional to the total incident  $P_2$  flux, the shell thickness on facets normal to  $270^\circ$  and  $330^\circ$  suggest an average  $P_2$  flux from scattering of 41–43% of direct beam. The calculated curvature is plotted for all ten cross-sections in Figure 4k using linear elastic theory with an assumed bending direction of  $\langle 11\bar{2} \rangle$  from  $120^\circ$ . The calculated average curvature is  $0.159 \mu\text{m}^{-1}$ , which is slightly higher than the value obtained from the STEM image of the same nanowire in Figure 3 ( $0.126 \mu\text{m}^{-1}$ ). However, despite the agreement between the modeled and measured curvature for this nanowire, the average curvature is significantly lower than that observed in SEM for nanowires from this sample—the nanowire in Figure 1b has a curvature of  $0.215 \mu\text{m}^{-1}$ . The cause of this discrepancy is unclear, and it is possible that the TEM-investigated nanowire is not representative of the average nanowire from this sample. Nevertheless, the fact that the modeled curvature agrees with the TEM-observed curvature on the same wire validates the EDS-extracted shell profile. The curvature locally modeled along the nanowire, as depicted in Figure 4k, reveals an approximately inverse relationship with core diameter (cf. Figure 3d). This inverse relationship has been previously demonstrated for nanowires with similar geometry in McDermott et al.<sup>3</sup>

To explore the twisting phenomena and differences in bending, we simulated the bending of a 100-nm-diameter GaAs core with different InP shell configurations. For the model, the local shell thicknesses are assumed to be proportional to the  $P_2$  flux received, based

on are previous findings,<sup>9</sup> and the scattered flux is assumed to be half of the direct beam flux and equally impinge on all side facets. Figure 5a displays the calculated curvature as a function of shell area for four P<sub>2</sub> deposition directions: the  $\langle 1\bar{1}0 \rangle$  direction, 10° offset, 20° offset, and the  $\langle 11\bar{2} \rangle$  direction. The curvature can be categorized into three regimes: under-deposited, critically-deposited, and over-deposited, as detailed by McDermott et al.<sup>3</sup> Critical deposition corresponds to the peak curvature. As depicted in Figure 5a, the critical deposition does not significantly depend on the deposition orientation. For nanowires with P<sub>2</sub> flux along  $\langle 11\bar{2} \rangle$ , the critical deposition takes place at 5400 nm<sup>2</sup>, which is marginally less than the 5900 nm<sup>2</sup> observed for nanowires oriented in the  $\langle 1\bar{1}0 \rangle$  direction. At critical deposition, the maximum curvature occurs when the phosphorus flux aligns with the  $\langle 1\bar{1}0 \rangle$  direction and diminishes as the nanowire orientation shifts to the  $\langle 11\bar{2} \rangle$  direction, consistent with the experimental observations above. Importantly however, the difference in the modeled curvature is small, in sharp contrast with the experimental observation (Figure 1e). We speculate that the experimentally-observed reduction in bending might result from a variation in cross-sectional shell distribution, or favorable dislocation formation for certain shell geometries. Tomographic analysis reveals additional shell growth on side facets parallel to the phosphorus beam, which would reduce curvature. Further experiments are necessary to explore the origin of this discrepancy.

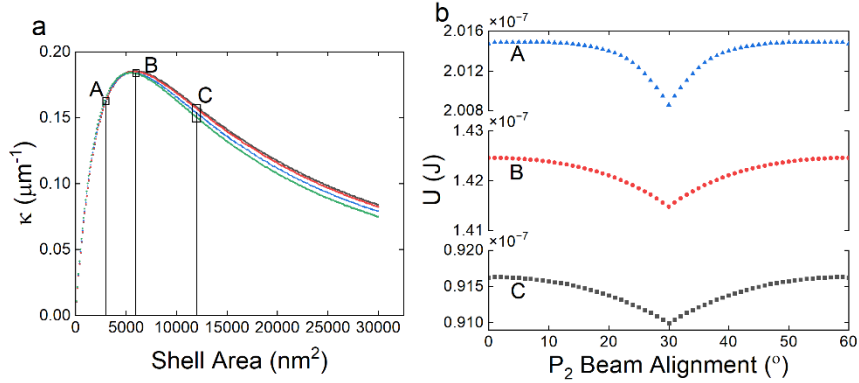


**Figure 5.5.** Linear elastic modeling of nanowire cross-sections with 100 nm diameter cores. (a) Curvature ( $\kappa$ ) plotted as a function of shell area for four  $P_2$  beam alignments offset from the  $\langle 1\bar{1}0 \rangle$  direction by  $0^\circ$  (black),  $10^\circ$  (red),  $20^\circ$  (blue), and  $30^\circ$  (green). Points A (3000  $\text{nm}^2$ ), B (6000  $\text{nm}^2$ ), and C (12000  $\text{nm}^2$ ) show under-deposited, critically-deposited, and over-deposited shell areas, respectively. The strain energies for depositions corresponding to Point A (blue), Point B (red), and Point C (black) are plotted in (b) for  $P_2$  beam alignments varying from  $0^\circ$  to  $60^\circ$

Figure 5b displays the strain energy plotted as a function of  $P_2$  flux direction for under-deposited, critically-deposited, and over-deposited regimes (points A, B, and C in Figure 5a). For each curve, the minimum energy corresponds to the  $P_2$  beam incident along  $\langle 11\bar{2} \rangle$ . Thus, the reason the nanowire twists to bend along the  $\langle 11\bar{2} \rangle$  crystallographic direction involves energy minimization during shell deposition. Nanowires energetically favor growth in this direction and twist to reduce strain energy. Figure 5b shows two stable  $P_2$  beam orientations:  $\langle 1\bar{1}0 \rangle$  and  $\langle 11\bar{2} \rangle$ . Twisting happens due to an energy gradient with the  $P_2$  beam angle twisting towards an energy minima. The  $\langle 1\bar{1}0 \rangle$   $P_2$  beam alignment is a local minimum within  $\pm 1^\circ$ , so most initial  $P_2$  beam alignments will result in twisting towards the  $\langle 11\bar{2} \rangle$  direction. Thus, the twisting in Figure 2 occurs

because the nanowire orients itself in the  $\langle 11\bar{2} \rangle$  direction to minimize strain energy. Interestingly, these findings are corroborated in Rossi et al.<sup>30</sup> where InSb core–asymmetric shell geometry of As-poor and As-rich regions has a  $\langle 11\bar{2} \rangle$  preferential bending orientation without any intentional beam alignment.

## 5.5 Conclusion

The twisting and bending behavior of nanowires subject to a directional deposition process at varying orientations relative to the nanowire facets have been explored. Nanowires aligned with  $P_2$  flux (and shell growth) along the  $\langle 1\bar{1}0 \rangle$  direction exhibited nearly 2 times more bending compared to those oriented in the  $\langle 11\bar{2} \rangle$  direction. Additionally, intermediate orientations—between  $\langle 1\bar{1}0 \rangle$  and  $\langle 11\bar{2} \rangle$  directions—exhibit twisting toward the  $\langle 11\bar{2} \rangle$  direction, which is shown to result from elastic strain energy minimization. A practical analytical electron tomography method is demonstrated, which allows for detailed examination of nanowire cross-sections, revealing local variations in diameter, shell area, and shell distribution. This technique can reconstruct nanowire cross-sections with only two scan directions utilizing known features from the nanowire geometry. This approach allows for practical imaging of bent nanowires. These findings demonstrate the importance of considering crystallographic orientation during bent nanowire synthesis, due to the significant impacts on bending and twisting.

## Supporting Information

Supporting information is provided in appendix.

## References

- (1) Hilse, M.; Takagaki, Y.; Herfort, J.; Ramsteiner, M.; Herrmann, C.; Breuer, S.; Geelhaar, L.; Riechert, H. Ferromagnet-Semiconductor Nanowire Coaxial Heterostructures Grown by Molecular-Beam Epitaxy. *Appl Phys Lett* 2009, 95 (13). <https://doi.org/10.1063/1.3240405>.
- (2) Lewis, R. B.; Corfdir, P.; Küpers, H.; Flissikowski, T.; Brandt, O.; Geelhaar, L. Nanowires Bending over Backward from Strain Partitioning in Asymmetric Core-Shell Heterostructures. *Nano Lett* 2018, 18 (4), 2343–2350. <https://doi.org/10.1021/acs.nanolett.7b05221>.
- (3) McDermott, S.; Lewis, R. B. Bending of GaAs–InP Core–Shell Nanowires by Asymmetric Shell Deposition: Implications for Sensors. *ACS Appl Nano Mater* 2021. <https://doi.org/10.1021/acsanm.1c01636>.
- (4) Al-Humaidi, M.; Feigl, L.; Jakob, J.; Schroth, P.; Alhassan, A.; Davtyan, A.; Herranz, J.; Anjum, T.; Novikov, D.; Francoual, S.; Geelhaar, L.; Baumbach, T.; Pietsch, U. In Situ X-Ray Analysis of Misfit Strain and Curvature of Bent Polytypic GaAs-In<sub>x</sub>Ga<sub>1-x</sub>As Core-Shell Nanowires. *Nanotechnology* 2022, 33 (1). <https://doi.org/10.1088/1361-6528/ac29d8>.
- (5) Al Humaidi, M.; Jakob, J.; Al Hassan, A.; Davtyan, A.; Schroth, P.; Feigl, L.; Herranz, J.; Novikov, D.; Geelhaar, L.; Baumbach, T.; Pietsch, U. Exploiting Flux Shadowing for Strain and Bending Engineering in Core-Shell Nanowires. *Nanoscale* 2022, 15 (5), 2254–2261. <https://doi.org/10.1039/d2nr03279a>.
- (6) Bisht, A.; Kalina, M.; Suadiye, E.; Richter, G.; Rabkin, E. Nanoscale Bimetallic Strip: Atomistic Bending Mechanisms of AuPd Bimetallic Nanowhiskers. *Acta Mater* 2023, 243. <https://doi.org/10.1016/j.actamat.2022.118504>.
- (7) Kryvyi, S.; Kret, S.; Domagala, J.; Wojnar, P. Reconstruction of Three-Dimensional Strain Field in an Asymmetrical Curved Core-Shell Hetero-Nanowire. *Nanotechnology* 2023. <https://doi.org/10.1088/1361-6528/acebf6>.
- (8) van Treeck, D.; Lähnemann, J.; Gao, G.; Garrido, S. F.; Brandt, O.; Geelhaar, L. Sequential Directional Deposition of One-Sided (In,Ga)N Shells on GaN Nanowires by Molecular Beam Epitaxy. *APL Mater* 2023, 11 (9). <https://doi.org/10.1063/5.0168786>.
- (9) McDermott, S.; Smith, T. R.; LaPierre, R. R.; Lewis, R. B. Phosphorus-Controlled Nanoepitaxy of Asymmetric GaAs-InP Core-Shell Bent Nanowires: Implications

- for Bottom-Up Nanowire Transistors and Sensors. *ACS Appl Nano Mater* 2024, 7 (1), 1257–1264. <https://doi.org/10.1021/acsnm.3c05235>.
- (10) Al Hassan, A.; AlHumaidi, M.; Kalt, J.; Schneider, R.; Müller, E.; Anjum, T.; Khadiev, A.; Novikov, D. V.; Pietsch, U.; Baumbach, T. Bending and Reverse Bending during the Fabrication of Novel GaAs/(In,Ga)As/GaAs Core-Shell Nanowires Monitored by in Situ x-Ray Diffraction. *Nanotechnology* 2024, 35 (29). <https://doi.org/10.1088/1361-6528/ad3fc1>.
- (11) Krogstrup, P.; Ziino, N. L. B.; Chang, W.; Albrecht, S. M.; Madsen, M. H.; Johnson, E.; Nygård, J.; Marcus, C. M.; Jespersen, T. S. Epitaxy of Semiconductor-Superconductor Nanowires. *Nat Mater* 2015, 14 (4), 400–406. <https://doi.org/10.1038/nmat4176>.
- (12) Bjergfelt, M.; Carrad, D. J.; Kanne, T.; Aagesen, M.; Fiordaliso, E. M.; Johnson, E. Superconducting Vanadium / Indium-Arsenide Hybrid Nanowires. *Nanotechnology* 2019, 30 (29), 294005. <https://doi.org/10.1088/1361-6528/ab15fc>.
- (13) Xu, Y.; Li, L.; Zang, Y.; Hu, J.; Li, Z.; Chen, H.; Zhang, G.; Xia, C.; Cho, J. Forward Bending of Silicon Nanowires Induced by Strain Distribution in Asymmetric Growth. *Mater Lett* 2021, 297, 129929. <https://doi.org/10.1016/j.matlet.2021.129929>.
- (14) Khan, S. A.; Martí-Sánchez, S.; Olsteins, D.; Lampadaris, C.; Carrad, D. J.; Liu, Y.; Quiñones, J.; Chiara Spadaro, M.; Sand Jespersen, T.; Krogstrup, P.; Arbiol, J. Epitaxially Driven Phase Selectivity of Sn in Hybrid Quantum Nanowires. *ACS Nano* 2023, 17 (12), 11794–11804. <https://doi.org/10.1021/acsnano.3c02733>.
- (15) Greenberg, Y.; Kelrich, A.; Cohen, S.; Kar-Narayan, S.; Ritter, D.; Calahorra, Y. Strain-Mediated Bending of InP Nanowires through the Growth of an Asymmetric InAs Shell. *Nanomaterials* 2019, 9 (9), 1–11. <https://doi.org/10.3390/nano9091327>.
- (16) Wulff, G. XXV. Zur Frage Der Geschwindigkeit Des Wachstums Und Der Auflösung Der Krystallflächen. *Z Kristallogr Cryst Mater* 1901, 34 (1), 449–530.
- (17) Ma, C.; Moore, D.; Li, J.; Wang, Z. L. Nanobelts, Nanocombs, and Nanowindmills of Wurtzite ZnS. *Advanced Materials* 2003, 15 (3), 228–231. <https://doi.org/10.1002/adma.200390052>.
- (18) Krishnamachari, U.; Borgstrom, M.; Ohlsson, B. J.; Panev, N.; Samuelson, L.; Seifert, W.; Larsson, M. W.; Wallenberg, L. R. Defect-Free InP Nanowires Grown in [001] Direction on InP (001). *Appl Phys Lett* 2004, 85 (11), 2077–2079. <https://doi.org/10.1063/1.1784548>.

- (19) Yao, X.; Zhang, X.; Sun, Q.; Wei, D.; Chen, P.; Zou, J. Anomalous Photoelectrical Properties through Strain Engineering Based on a Single Bent InAsSb Nanowire. *ACS Appl Mater Interfaces* 2021, 13 (4), 5691–5698. <https://doi.org/10.1021/acsami.0c16028>.
- (20) Salimitari, P.; Behroudj, A.; Strehle, S. Aligned Deposition of Bottom-up Grown Nanowires by Two-Directional Pressure-Controlled Contact Printing. *Nanotechnology* 2022, 33 (23). <https://doi.org/10.1088/1361-6528/ac56f8>.
- (21) Keplinger, M.; Kriegner, D.; Stangl, J.; Mårtensson, T.; Mandl, B.; Wintersberger, E.; Bauer, G. Core-Shell Nanowires: From the Ensemble to Single-Wire Characterization. *Nucl Instrum Methods Phys Res B* 2010, 268 (3–4), 316–319. <https://doi.org/10.1016/j.nimb.2009.09.043>.
- (22) Gagliano, L.; Albani, M.; Verheijen, M. A.; Bakkers, E. P. A. M.; Miglio, L. Twofold Origin of Strain-Induced Bending in Core-Shell Nanowires: The GaP/InGaP Case. *Nanotechnology* 2018, 29 (31). <https://doi.org/10.1088/1361-6528/aac417>.
- (23) Meng, A. C.; Wang, Y.; Braun, M. R.; Lentz, J. Z.; Peng, S.; Cheng, H.; Marshall, A. F.; Cai, W.; McIntyre, P. C. Bending and Precipitate Formation Mechanisms in Epitaxial Ge-Core/GeSn-Shell Nanowires. *Nanoscale* 2021, 13 (41), 17547–17555. <https://doi.org/10.1039/d1nr04220c>.
- (24) Hadjimichael, Y.; Merdon, C.; Liero, M.; Farrell, P. An Energy-Based Finite-Strain Model for 3D Heterostructured Materials and Its Validation by Curvature Analysis. *Int J Numer Methods Eng* 2024. <https://doi.org/10.1002/nme.7508>.
- (25) Hetzl, M.; Winnerl, J.; Francaviglia, L.; Kraut, M.; Döblinger, M.; Matich, S.; FontcubertaMorrall, A.; Stutzmann, M. Surface Passivation and Self-Regulated Shell Growth in Selective Area-Grown GaN-(Al,Ga)N Core-Shell Nanowires. *Nanoscale* 2017, 9 (21), 7179–7188. <https://doi.org/10.1039/c7nr00802c>.
- (26) Wallentin, J.; Jacobsson, D.; Osterhoff, M.; Borgström, M. T.; Salditt, T. Bending and Twisting Lattice Tilt in Strained Core-Shell Nanowires Revealed by Nanofocused X-Ray Diffraction. *Nano Lett* 2017, 17 (7), 4143–4150. <https://doi.org/10.1021/acs.nanolett.7b00918>.
- (27) Teo, B. K.; Sun, X. H.; Hung, T. F.; Meng, X. M.; Wong, N. B.; Lee, S. T. Precision-Cut Crystalline Silicon Nanodots and Nanorods from Nanowires and Direct Visualization of Cross Sections and Growth Orientations of Silicon Nanowires. *Nano Lett* 2003, 3 (12), 1735–1737. <https://doi.org/10.1021/nl034603v>.

- (28) Fakhr, A.; Haddara, Y. M.; LaPierre, R. R. Dependence of InGaP Nanowire Morphology and Structure on Molecular Beam Epitaxy Growth Conditions. *Nanotechnology* 2010, 21 (16). <https://doi.org/10.1088/0957-4484/21/16/165601>.
- (29) Lenrick, F.; Ek, M.; Jacobsson, D.; Borgström, M. T.; Wallenberg, L. R. FIB Plan and Side View Cross-Sectional TEM Sample Preparation of Nanostructures. *Microscopy and Microanalysis* 2014, 20 (1), 133–140. <https://doi.org/10.1017/S1431927613013780>.
- (30) Rossi, M.; van Schijndel, T. A. J.; Lueb, P.; Badawy, G.; Jung, J.; Peeters, W. H. J.; Koelling, S.; Moutanabbir, O.; Verheijen, M. A.; Bakkers, E. Stemless InSb Nanowire Networks and Nanoflakes Grown on InP. *Nanotechnology* 2024. <https://doi.org/10.1088/1361-6528/ad61ef>.
- (31) Perea, D. E.; Allen, J. E.; May, S. J.; Wessels, B. W.; Seidman, D. N.; Lauhon, L. J. Three-Dimensional Nanoscale Composition Mapping of Semiconductor Nanowires. *Nano Lett* 2006, 6 (2), 181–185. <https://doi.org/10.1021/nl051602p>.
- (32) Blumtritt, H.; Isheim, D.; Senz, S.; Seidman, D. N.; Moutanabbir, O. Preparation of Nanowire Specimens for Laser-Assisted Atom Probe Tomography. *Nanotechnology* 2014, 25 (43). <https://doi.org/10.1088/0957-4484/25/43/435704>.
- (33) Gault, B.; Chiaramonti, A.; Cojocaru-Miréidin, O.; Stender, P.; Dubosq, R.; Freysoldt, C.; Makineni, S. K.; Li, T.; Moody, M.; Cairney, J. M. Atom Probe Tomography. *Nature Reviews Methods Primers*. Springer Nature December 1, 2021. <https://doi.org/10.1038/s43586-021-00047-w>.
- (34) Verheijen, M. A.; Algra, R. E.; Borgström, M. T.; Immink, G.; Sourty, E.; Van Enckevort, W. J. P.; Vlieg, E.; Bakkers, E. P. A. M. Three-Dimensional Morphology of GaP-GaAs Nanowires Revealed by Transmission Electron Microscopy Tomography. *Nano Lett* 2007, 7 (10), 3051–3055. <https://doi.org/10.1021/nl071541q>.
- (35) Wu, J.; Padalkar, S.; Xie, S.; Hemesath, E. R.; Cheng, J.; Liu, G.; Yan, A.; Connell, J. G.; Nakazawa, E.; Zhang, X.; Lauhon, L. J.; Dravid, V. P. Electron Tomography of Au-Catalyzed Semiconductor Nanowires. *Journal of Physical Chemistry C* 2013, 117 (2), 1059–1063. <https://doi.org/10.1021/jp310816f>.
- (36) Haberfehlner, G.; Orthacker, A.; Albu, M.; Li, J.; Kothleitner, G. Nanoscale Voxel Spectroscopy by Simultaneous EELS and EDS Tomography. *Nanoscale* 2014, 6 (23), 14563–14569. <https://doi.org/10.1039/c4nr04553j>.
- (37) Baba, N.; Hata, S.; Saito, H.; Kaneko, K. Three-Dimensional Electron Tomography and Recent Expansion of Its Applications in Materials Science. *Microscopy* 2023, 72 (2), 111–134. <https://doi.org/10.1093/jmicro/dfac071>.

- (38) Collins, S. M.; Fernandez-Garcia, S.; Calvino, J. J.; Midgley, P. A. Sub-Nanometer Surface Chemistry and Orbital Hybridization in Lanthanum-Doped Ceria Nano-Catalysts Revealed by 3D Electron Microscopy. *Sci Rep* 2017, 7 (1). <https://doi.org/10.1038/s41598-017-05671-9>.
- (39) Wang, Y. C.; Slater, T. J. A.; Leteba, G. M.; Roseman, A. M.; Race, C. P.; Young, N. P.; Kirkland, A. I.; Lang, C. I.; Haigh, S. J. Imaging Three-Dimensional Elemental Inhomogeneity in Pt-Ni Nanoparticles Using Spectroscopic Single Particle Reconstruction. *Nano Lett* 2019, 19 (2), 732–738. <https://doi.org/10.1021/acs.nanolett.8b03768>.
- (40) Rueda-Fonseca, P.; Robin, E.; Bellet-Amalric, E.; Lopez-Haro, M.; Den Hertog, M.; Genuist, Y.; André, R.; Artioli, A.; Tatarenko, S.; Ferrand, D.; Cibert, J. Quantitative Reconstructions of 3D Chemical Nanostructures in Nanowires. *Nano Lett* 2016, 16 (3), 1637–1642. <https://doi.org/10.1021/acs.nanolett.5b04489>.
- (41) Sistani, M.; Luong, M. A.; Den Hertog, M. I.; Robin, E.; Spies, M.; Fernandez, B.; Yao, J.; Bertagnolli, E.; Lugstein, A. Monolithic Axial and Radial Metal-Semiconductor Nanowire Heterostructures. *Nano Lett* 2018, 18 (12), 7692–7697. <https://doi.org/10.1021/acs.nanolett.8b03366>.
- (42) El Hajraoui, K.; Luong, M. A.; Robin, E.; Brunbauer, F.; Zeiner, C.; Lugstein, A.; Gentile, P.; Rouvière, J. L.; Den Hertog, M. In Situ Transmission Electron Microscopy Analysis of Aluminum-Germanium Nanowire Solid-State Reaction. *Nano Lett* 2019, 19 (5), 2897–2904. <https://doi.org/10.1021/acs.nanolett.8b05171>.
- (43) El Hajraoui, K.; Robin, E.; Zeiner, C.; Lugstein, A.; Kodjikian, S.; Rouvière, J. L.; Den Hertog, M. In Situ Transmission Electron Microscopy Analysis of Copper-Germanium Nanowire Solid-State Reaction. *Nano Lett* 2019, 19 (12), 8365–8371. <https://doi.org/10.1021/acs.nanolett.9b01797>.
- (44) Davtyan, A.; Kriegner, D.; Holý, V.; AlHassan, A.; Lewis, R. B.; McDermott, S.; Geelhaar, L.; Bahrami, D.; Anjum, T.; Ren, Z.; Richter, C.; Novikov, D.; Müller, J.; Butz, B.; Pietsch, U. X-Ray Diffraction Reveals the Amount of Strain and Homogeneity of Extremely Bent Single Nanowires. *J Appl Crystallogr* 2020, 53 (11), 1310–1320. <https://doi.org/10.1107/S1600576720011516>.
- (45) Ramdani, M. R.; Harmand, J. C.; Glas, F.; Patriarche, G.; Travers, L. Arsenic Pathways in Self-Catalyzed Growth of GaAs Nanowires. *Cryst Growth Des* 2013, 13 (1), 91–96. <https://doi.org/10.1021/cg301167g>.
- (46) Küpers, H.; Lewis, R. B.; Geelhaar, L. Predictive Model for the Temporal Evolution of the Shape of GaAs Nanowires. *J Cryst Growth* 2020, 531. <https://doi.org/10.1016/j.jcrysgro.2019.125320>.

## Chapter 6

### Conclusions and Future Work

#### 6.1 Conclusions

Throughout my graduate studies, I worked to unravel the complexities of directional nanoepitaxy in the vapor-solid shell growth of nanowire core-shell heterostructures. This endeavor was both an academic pursuit to comprehend the physics behind the technique and an effort to develop a method for fabricating nanowire sensor devices. This thesis lays the groundwork of methodology for producing bent nanowires, exploring directional lattice-mismatched nanoepitaxy as a mechanism for inducing bending in nanowires and discussing the potential applications of this phenomenon for device fabrication.

It was shown that the directional nanoepitaxy of asymmetric shells on nanowires is a non-trivial process resulting in unavoidable variations along the nanowire. However, through these growth parameters, directional nanoepitaxy and the resulting bending are controllable. Various parameters such as core diameter, lattice mismatch, incident flux angle, and shell thickness are modeled to elucidate their individual impacts on bending. Experiments reveal a significant difference in bending for different side facet orientations and show that twisting occurs due to strain energy minimization during shell growth, leading to energetically favorable shell distributions which cause bending in specific crystallographic directions. The effects of some of these parameters are time-dependent due to the changing geometry of the nanowire and flux contact angle as the nanowire

bends. The concepts of under-, critical, and over-deposition are explained with evolution modeling showing the theoretical maximum curvature possible and expected bending of nanowire heterostructures. Moreover, evolution modeling of shell deposition shows shadowing effects can be utilized to connect pairs of nanowires with less bending than would otherwise be necessary.

One key finding is the discovery of two distinct growth modes for InP shells grown around GaAs cores: diffusion-limited and phosphorus-controlled. In the diffusion-limited mode, the shell distribution is determined by the indium flux on a nanowire's side facets, whereas in the phosphorus-controlled mode, the shell thickness on a side facet is linearly proportional to the phosphorus flux received relative to other facets. This makes the phosphorus-controlled mode highly controllable allowing for the production of nano-arches by connecting pairs of nanowire. These nanowire pairs fuse together when connected this way and show a favorable out-of-plane geometry for sensor applications. It is noteworthy that InP has been shown to be a promising material for sensor applications.

This thesis presents directional nanoepitaxy as a growth technique for advancing the design and manufacturing of nanowire-based sensor devices. Phosphorus-controlled shell growth provides massively parallel and precise control over nanowire morphology and bending, and through controlling growth parameters nanowires can be manipulated forming nanowire-to-nanowire connections above the substrate. These connected pairs can act as a transducer for a field effect transistor (FET)-based sensor, however this

remains to be realized as a complete process is needed to make this potential transducer into a device.

## 6.2 Road Ahead

To develop GaAs–InP core–shell nano-arches into sensor devices, three key factors must be addressed: electrical isolation of the nanowire bases from short circuits through the substrate, doping of both the substrate and nanowires, and functionalizing the surfaces of the nanowires. Existing processes have already been developed for CMOS devices and sensors can be utilized to address these factors, and the current challenge is to integrate these techniques together.

Electrical isolation is essential to separate the nanowire bases from the substrate. Without this isolation, the nano-arches will not function as a channel or transducer for the device since the path of least resistance would be through the substrate, rendering the nanowires ineffective. Trenching is an efficient method for electrical isolation in CMOS devices,<sup>1</sup> and it could be adapted for use on an implanted wafer or a silicon-on-insulator wafer. By trenching areas around the base pre-growth, electrical isolation can be achieved, enabling the construction of a nanowire FET device.

To create an effective device, the doping of both the substrate and nanowires must be optimized. A highly doped substrate ensures effective metal–substrate contacts.<sup>2</sup> For the III-V nanowire, doping techniques have been established.<sup>3,4</sup> Nanowire FET-based sensors exhibit enhanced sensitivity with light doping compared to high concentrations,<sup>5</sup> and if low doping or no doping is optimal, doping the nano-arch device should be feasible,

though further investigation and experimentation are necessary to determine the ideal doping concentrations.

Ongoing research continues to advance nanowire functionalization, and InP nanostructures have been successfully functionalized for various biological species.<sup>6,7</sup> These established methodologies for functionalization could be applicable to these nanoarches. Moreover, the creation of a mass-produced nanowire FET device will spur further functionalization research by lowering costs and expanding access to template devices for study.

The road ahead for creating a sensor device involves combining these well-established fabrication techniques, and the realization of such a sensor-based device appears to be within clear reach.

## References

- (1) Nandakumar, M.; Chatterjee, A.; Sridhar, S.; Joyner, K.; Rodder, M.; Chen, I.-C. Shallow Trench Isolation for Advanced ULSI CMOS Technologies. International Electron Devices Meeting Technical Digest 1998. <https://doi.org/10.1109/IEDM.1998.746297>.
- (2) Chang Y K Fang, C. Y.; Sze, S. M. Solid-State Electronirs SPECIFIC CONTACT RESISTANCE OF METAL-SEMICONDUCTOR BARRIERS; Pergamon Press, 1971; Vol. 14.
- (3) Hijazi, H.; Monier, G.; Gil, E.; Trassoudaine, A.; Bougerol, C.; Leroux, C.; Castellucci, D.; Robert-Goumet, C.; Hoggan, P. E.; André, Y.; Isik Goktas, N.; Lapierre, R. R.; Dubrovskii, V. G. Si Doping of Vapor-Liquid-Solid Gaas Nanowires: N-Type or p-Type? Nano Lett 2019, 19 (7), 4498–4504. <https://doi.org/10.1021/acs.nanolett.9b01308>.
- (4) Dubrovskii, V. G.; Hijazi, H.; Goktas, N. I.; Lapierre, R. R. Be, Te, and Si Doping of GaAs Nanowires: Theory and Experiment. Journal of Physical Chemistry C 2020, 124 (31), 17299–17307. <https://doi.org/10.1021/acs.jpcc.0c04061>.
- (5) Li, J.; Zhang, Y.; To, S.; You, L.; Sun, Y. Effect of Nanowire Number, Diameter, and Doping Density on Nano-FET Biosensor Sensitivity. ACS Nano 2011, 5 (8), 6661–6668. <https://doi.org/10.1021/nn202182p>.

- (6) Sato, T.; Mizohata, A.; Hashizume, T. Electrochemical Functionalization of InP Porous Nanostructures with a GOD Membrane for Amperometric Glucose Sensors. *J Electrochem Soc* 2010, 157 (2), H165. <https://doi.org/10.1149/1.3264634>.
- (7) Janissen, R.; Sahoo, P. K.; Santos, C. A.; Da Silva, A. M.; Von Zuben, A. A. G.; Souto, D. E. P.; Costa, A. D. T.; Celedon, P.; Zanchin, N. I. T.; Almeida, D. B.; Oliveira, D. S.; Kubota, L. T.; Cesar, C. L.; Souza, A. P. D.; Cotta, M. A. InP Nanowire Biosensor with Tailored Biofunctionalization: Ultrasensitive and Highly Selective Disease Biomarker Detection. *Nano Lett* 2017, 17 (10), 5938–5949. <https://doi.org/10.1021/acs.nanolett.7b01803>.

## Chapter 7 Appendix

### **Supporting Information: X-ray diffraction reveals the amount of strain and homogeneity of extremely bent single nanowires**

Prior to NW measurements the X-ray wavefront was characterized by 2D Ptychography at forward direction. To this aim the available setup at ID01 using Siemens star and PyNX software for phase retrieval reconstructions was used. The detector to Siemens star distance was set to 1547 mm in order to capture the fine speckles originating from the interaction of coherent X-rays within the structure of Siemens star. For successful and better convergence as usual (from our experience) the Siemens star was mounted not at the focus but downstream by around  $86 \mu\text{m}$ . Figure 3(a) represents the reconstruction of the Siemens star, amplitude and phase image, and indicates the trust region by black cycle. Figure 3(b) represents the reconstructed wavefront at the position of the Siemens star, and figure s1(c) at the focus. As it can be seen the Intensity modulations present in the profile of the incoming X-ray beam focused by KB mirrors at 9KeV. The line profiles of the wavefront are presented in figure s1(d) where we observe the beam with FWHM of  $480 \times 230 \text{ nm}^2$  (HxV). The phase retrieval algorithm uses the sequence of algorithms and probe activation following to: 20DM, probe=1, 100DM, 100AP, 100ML, nprobe=3, 100DM, 100AP, 100ML using 393 frames and with the pixel size (resolution) of 14.7 nm

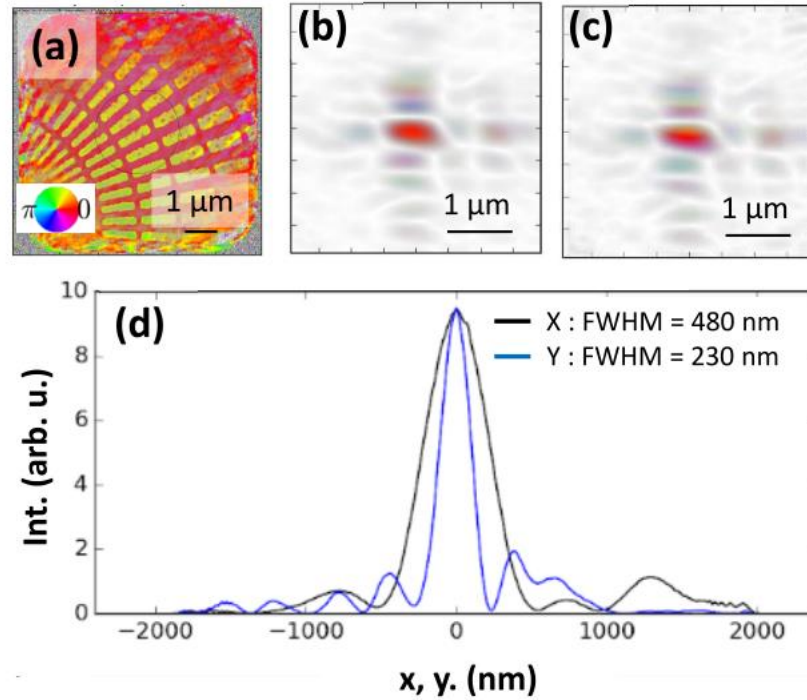


**Figure S1** Beam profile/wavefront characterization from ID01 beamline. (a) Reconstructed amplitude and phase image of Siemens star. (b,c) Reconstructed amplitude and phase image of beam profile out of focus and in focus positions. (d) Line profiles of the X-ray beam at focus along the horizontal and vertical directions.

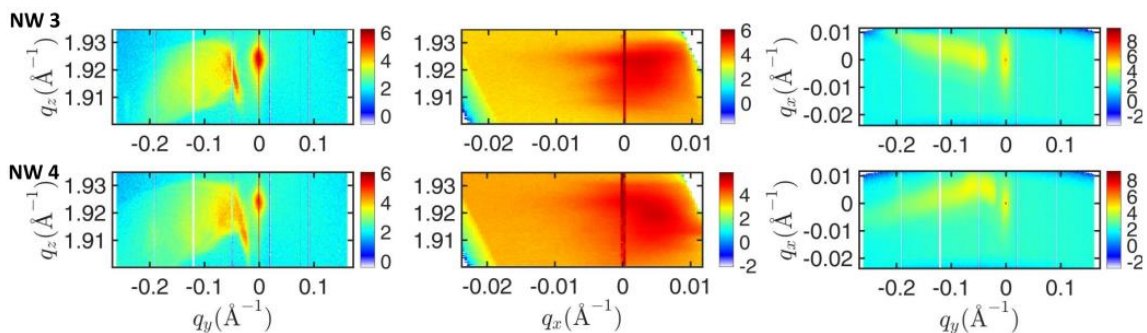


**Figure S2** Projections of the 3D RSMs measured from the basis of NW3 and NW4 of sample 2. The NW signal left of the substrates CTR starts from  $q_y \sim -0.03 \text{ \AA}^{-1}$  and extends to lower  $q_y$  values. The offset of the NW signal from the CTR even for the bottom part of the NW means that these NWs are already nucleating with a slight tilt with respect to the substrate (111) surface.

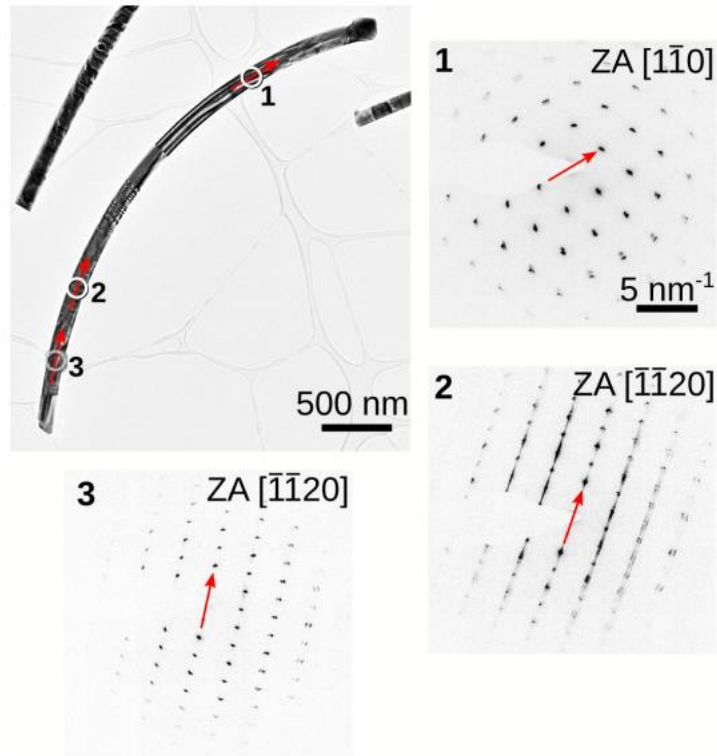


**Figure S3** Three transmission electron diffraction patterns recorded from a NW of sample 2. The location from which the diffraction patterns were recorded are marked in the overview image shown on the top right. The local wire axis is found to correspond with the  $[111]_{\text{ZB}}$  or  $[0001]_{\text{WZ}}$  in the wire axis.

## Supporting Information: Phosphorus-Controlled Nanoepitaxy

### of Asymmetric GaAs–InP Core–Shell Bent Nanowires:

### Implications for Bottom-Up Nanowire Transistors and Sensors

This supporting information provides details about the nanowire core growth as well as the EDS analysis of nanowire cross-sections. First, we describe the substrate preparation and GaAs nanowire core growth, and provide scanning electron microscopy (SEM) core images. Next, spectral information of a nanowire cross-section from energy dispersive

spectroscopy (EDS) is presented. The quantitative EDS analysis used to determine nanowire shell thicknesses is explained. Lastly, we provide additional transmission electron microscopy (TEM) images of nanowire microtome cross-section to provide context for nanowire-to-nanowire variation.

### **Substrate Preparation**

Si(111) substrates were covered by 30 nm of SiO<sub>2</sub> deposited by plasma-assisted chemical vapor deposition. The oxide layer was patterned by electron beam lithography (EBL) using a Raith EBPG 5000+ EBL system, followed by reactive ion etching. The pattern consisted of arrays of either individual or pairs of holes, spaced in a close-packed pattern separated by 5 or 10 μm in 100 x 100 μm fields. Hole pairs were spaced by 0.2, 0.6, 1.2, and 1.8 μm. Substrates were dipped in a solution of Fujifilm Buffered Oxide Etchant (10:1 NH<sub>4</sub>F:HF with Fujifilm surfactant) diluted with 9 parts water, for 28 seconds immediately before being loaded into the molecular beam epitaxy (MBE) growth system.

### **GaAs Core Growth**

The GaAs nanowire cores were grown at 630 °C with a predeposition of 250 s of Ga to form the droplets for self-catalyzation. The predeposition was followed by the GaAs core growth, with both steps using a Ga flux corresponding to a planar growth rate of 0.125 μm. There were two recipes used for the core growths: A a constant V:III ratio of 2 for 80 min, and B an initial V:III ratio of 2 for 20 min, followed by a ratio of 4 for 40 min. Core recipe A was used for the samples with shells grown at 210 °C and 295 °C, and recipe B for the two highest temperature shell growths (380 °C and 440 °C). At the

end of both core growth recipes, the Ga droplet was consumed by stopping the Ga flux while maintaining the As<sub>2</sub> flux for 20 minutes at 630 °C.

Figure S1 shows scanning electron micrographs (SEM) of GaAs cores. The nanowires in Fig. S1(a) correspond to recipe A—the cores used for shell growth at 210 °C and 295 °C. These cores exhibit inverse tapering (diameter at tip larger than at base). The cores are 3.7 μm long and have a diameter of ~100 nm at the base and ~150 nm near the tip. Figure S1b shows a nanowire core grown at the conditions like for recipe B, however, the step with V/III ratio of 4 was 60 min instead of the 40 min. This nanowire exhibits a length of 6.6 μm and a tapered diameter from 150 nm to 110 nm. TEM measurements on dispersed core-shell nanowires with cores grown under recipe B) (40 min at V/III of 4) were found to also exhibit similar tapering and a core length of ~4.7 μm.

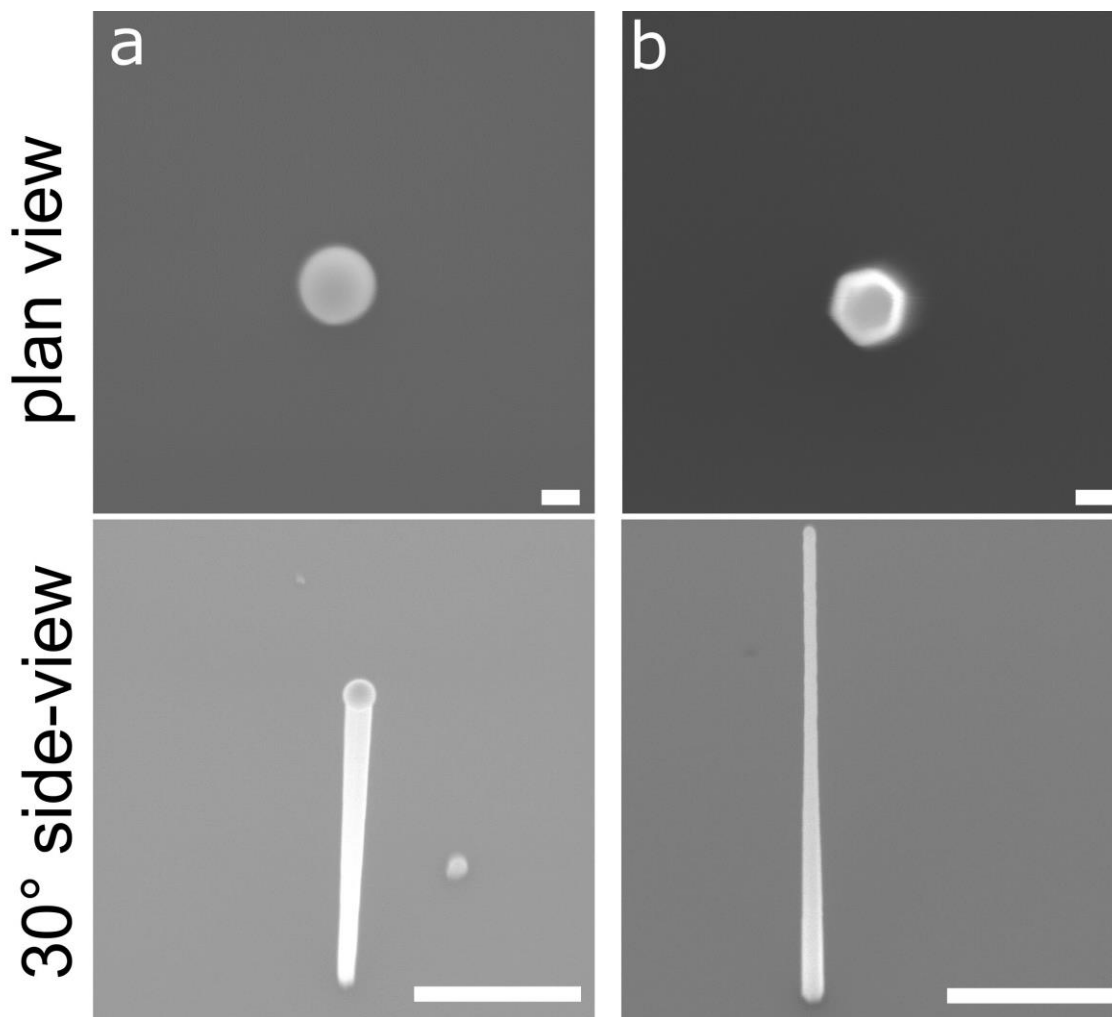


**Figure S1.** SEM images of GaAs nanowire cores. (a) GaAs nanowire core grown under recipe A. (b) GaAs nanowire core grown under a recipe similar to recipe B (however, the step with V/III of 4 was 60 min instead of 40 min). Scale bars are 100 nm for the upper row and 1  $\mu\text{m}$  for the lower row.

### Energy Dispersive X-ray Spectra

The EDS spectra were acquired with TEM in a Talos F200X instrument. The Talos 200X is outfitted with four in-column silicon drift detectors. The electron beam was accelerated to 200 kV. The scanning TEM (STEM) spatial resolution was 0.16 nm and the EDS spatial resolution was 1 nm. The EDS spectrum (Figure S2a) was fit in Thermo Fisher

Scientific's Velox software (Figure S2b).

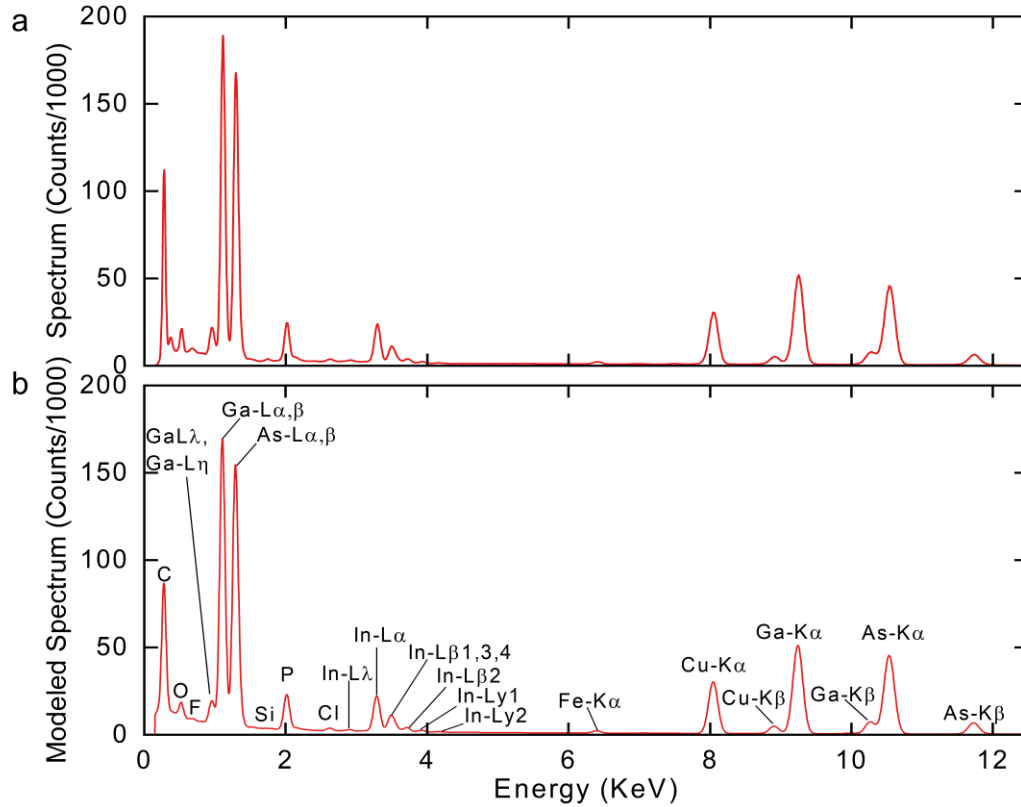


**Figure S2.** EDS spectra of a nanowire cross-section with shell grown at 210 °C. (a) The unmodified spectrum acquired in the Talos F200X. (b) A spectrum modeled with Velox to fit (a). Peaks are labeled with their corresponding emission.

The spectrum contains the elements of the III-V nanowire: In, Ga, P, and As peaks. There is a high number of counts of O and C from the Spurr's epoxy resin encasing the nanowire and from coating the grids in C to reduce charging during imaging. The other element with substantial counts is Cu arising from the Formvar-coated Cu TEM grids used. The Si presence is suspected to be from contamination from the substrate during microtomy. The presence of F and Cl are due to Spurr's epoxy. Lastly, Fe is present as a background element in the microscope.

### EDS Shell Thickness Quantification

For EDS mapping, the characteristic emissions used are from the Ga K-shell and the In L-shell. The net intensity (integrated intensity with background removal and peak separation) of these emissions was used for figures and quantification. The thickness of the shell can be measured directly from the EDS map, and line scans along the side facets can reveal variation along the side facets. The intensity profile of the line scan is related to the thickness of the nanowire's microtome cross-section. This can be derived from the  $\zeta$ -factor method for quantitative EDS using Equation S1.<sup>1,2</sup>

$$\zeta_m dI(x, y) = \rho_m T(x, y) C_m D_e dx dy \quad \text{Eq. (S1)}$$

$\zeta_m$  is a factor given to a material  $m$  and TEM system,  $I(x)$  is the intensity of the characteristic X-rays along the line scan for material  $m$ ,  $\rho_m$  is the density of the shell,  $T(x, y)$  is the depth of material along the line scan,  $C_m$  is the concentration of indium, and  $D_e$  is the dose from the electron beam. This assumes that material composition is constant in the InP shell—as expected—and that the microtome cut depth to be constant—no wedging or other thickness variation of the nanowire core was observed. Thus, all variables remain constant over the EDS map where the shell is present, yielding Equation S2.

$$dI(x, y) = A(x, y) dx dy \quad \text{Eq. (S2)}$$

For  $I_n$  in the shell,  $A(x, y)$  is nominally a 2D step function of the intensity of the L-shell characteristic emissions. The value is zero if the point  $(x, y)$  is off the shell, or it is equal to the step maximum intensity ( $A_{max}$ ) from Eq. (S1) if the point is on the shell,

$$A(x, y) = \begin{cases} \frac{\rho_{In} T(x, y) C_{In} D_e}{\zeta_{In}} & (x, y) = \textit{on shell} \\ 0 & (x, y) = \textit{off shell} \end{cases} \quad \text{Eq. (S3)}$$

Thus, for any line scan intensity along the nanowires side facet (seen in the inset of Figure S3b) with scan width  $W_{scan}$  along the scan length  $l$

$$I(l) = \int_{-W_{scan}/2}^{W_{scan}/2} A(w, l) dw \quad \text{Eq. (S4)}$$

If the shell side facet is fully enclosed by the line scan width, the intensity is proportional to the shell thickness  $T_{shell}(l)$  by the constant  $A_{max}$ , according to Equation S5.

$$I(l) = A_{max} T_{shell}(l) \quad \text{Eq. (S5)}$$

This step function approximation neglects the convolution of the STEM probe as well as other uncertainties resulting from inelastic interactions that result in a gaussian profile.

Thus, we fit the profile with a step function where the full width half maximum (FWHM) is taken to be the width of the step function and shell thickness ( $T_{shell}$ ). In this way, the mean shell thickness ( $\bar{T}_{shell}$ ) for an entire side facet is taken from a line scan shown in Figure S3(a).

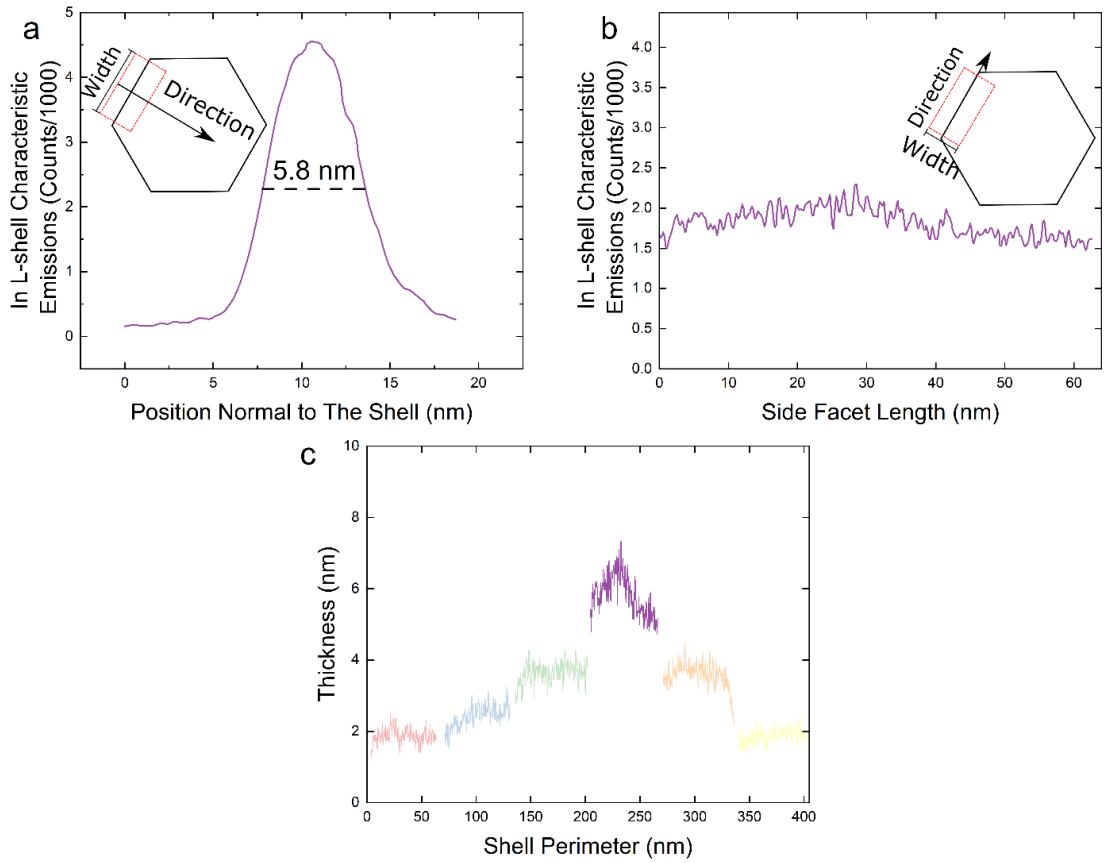


**Figure S3.** Shell thickness determination from EDS data. (a) A line scan normal to a side facet with a width that encompasses the side facet illustrated in the inset. The intensity profile is gaussian and the FWHM (5.8 nm) is taken to be the mean shell thickness  $\bar{T}_{shell}$  for the side facet. (b) A line scan along the same side facet with scan width fully enclosing the shell as illustrated in the inset. The intensity profile along the side facet is plotted. (c) The shell thickness plotted around the six nanowire side facets. The purple data corresponds to the side facet in (a) and (b).

Comparing the mean facet thickness to the mean intensity along the side facet (Figure S3b) allows for the determination of the constant  $A_{max}$

$$A_{max} = \frac{\bar{I}}{\bar{T}_{shell}} \quad \text{Eq. (S6)}$$

where  $\bar{I}$  is the mean intensity along the side facet. Using  $A_{max}$ , the shell thickness plots around the nanowire circumference (Figure S3c) were produced. For consistency and to minimize uncertainty,  $A_{max}$  was determined from the thickest shell facet of the nanowire and then used for all scans.

Relative weighting is effective for comparing side facets. However, it is noted that the nanowire cross-section grown at 210 °C shows significant bulging/mounding of the shell as seen in Figure 3a-b in the main text. Also, different intensities around the nanowire shell are observed in the EDS map, resulting in differences in intensity of the line scans and corresponding thicknesses which differ from those determined using high-angle annular dark-field or EDS mapping. This discrepancy is expected to result from variations along the nanowire axis due to the rough shell. We note that no variations in the core intensity are observed, only the shell grown at 210 °C.

## **P<sub>2</sub> Impingement and Growth Rate**

The growth rate for the side facets of the nanowires grown at 380 °C are taken from the mean value of the measured side facets, given by Equation S7

$$\frac{\partial g_f}{\partial t} = \frac{\bar{T}}{\tau} \quad \text{Eq. (S7)}$$

where  $\frac{\partial g_f}{\partial t}$  is the growth rate,  $\bar{T}$  is the measured thickness, and  $\tau$  is the shell deposition duration. From the six side facets from the nanowire in Figure 3f in the main text, this results in growth rates  $0.16 \pm 0.03 \mu\text{m/h}$  for facet 4,  $0.10 \pm 0.02 \mu\text{m/h}$  for facets 3 and 5,  $0.05 \pm 0.01 \mu\text{m/h}$  for facets 1 and 6, and  $0.07 \pm 0.01 \mu\text{m/h}$  for side facet 2.

The scattered flux is assumed to be equivalent on all the sidewall facets—confirmed by the symmetric shell for the shadowed nanowire in Figure 4(b-c) in the main text. We assume that the adatom incorporation diffusion length varies linearly with group V flux<sup>3-5</sup>. Thus, the following equation results:

$$\frac{\partial g_s}{\partial t} = C F_{P,s} = C \begin{cases} F_{P,direct} \langle \hat{b}_p \cdot -\hat{n} \rangle + F_{P,scattered} & 0 < \langle \hat{b}_p \cdot -\hat{n} \rangle \\ F_{P,scattered} & 0 \geq \langle \hat{b}_p \cdot -\hat{n} \rangle \end{cases} \quad \text{Eq. (S8)}$$

where  $F_{P,direct}$  is the flux from the direct P<sub>2</sub> beam and  $F_{P,scattered}$  is the P flux scattered from the substrate.  $\langle \hat{b}_p \cdot -\hat{n} \rangle$  is the geometric factor for the projected direct beam on a given facet,  $\hat{b}_p$  is the normalized vector in the direct P<sub>2</sub> beam direction and  $\hat{n}$  is the vector normal to the side facet.  $C$  is the constant relating P<sub>2</sub> flux to growth.

According to the facet numbering convention used in Figure 3e of the main text, facet 4 experiences the direct incident P<sub>2</sub> beam, with the normal of facets 3 and 5 having a projected angle of 60° from the direct P<sub>2</sub> flux. Therefore, the geometric factor  $\langle \hat{b}_p \cdot -\hat{n} \rangle$  (and thus the growth resulting from the direct P<sub>2</sub> flux) is expected to differ by a factor of  $\cos(60^\circ) = 0.5$  between facet 4 and facets 3 and 5. From the measured growth rates, the extracted growth resulting from direct P<sub>2</sub> impingement on facets 3 and 5 is found to be  $45 \pm 21\%$  and  $43 \pm 20\%$  of the direct growth on facet 4, respectively, in agreement with the prediction based on the nanowire geometry.

### **Supplemental Nanowire Cross-Sections**

High-angle annular dark-field (HAADF) TEM images and EDS maps of additional nanowire cross sections are shown in Figure S4. The nanowire geometry is relatively consistent between pairs from the same growth run (same shell temperature). The lower shell growth temperature of 210 °C yields rough shell surfaces with mounds on some side facets. The side facet that receives the most In flux appears comparatively smooth for all cross-sections and exhibits the thickest shell, while the other facets are considerably rougher.

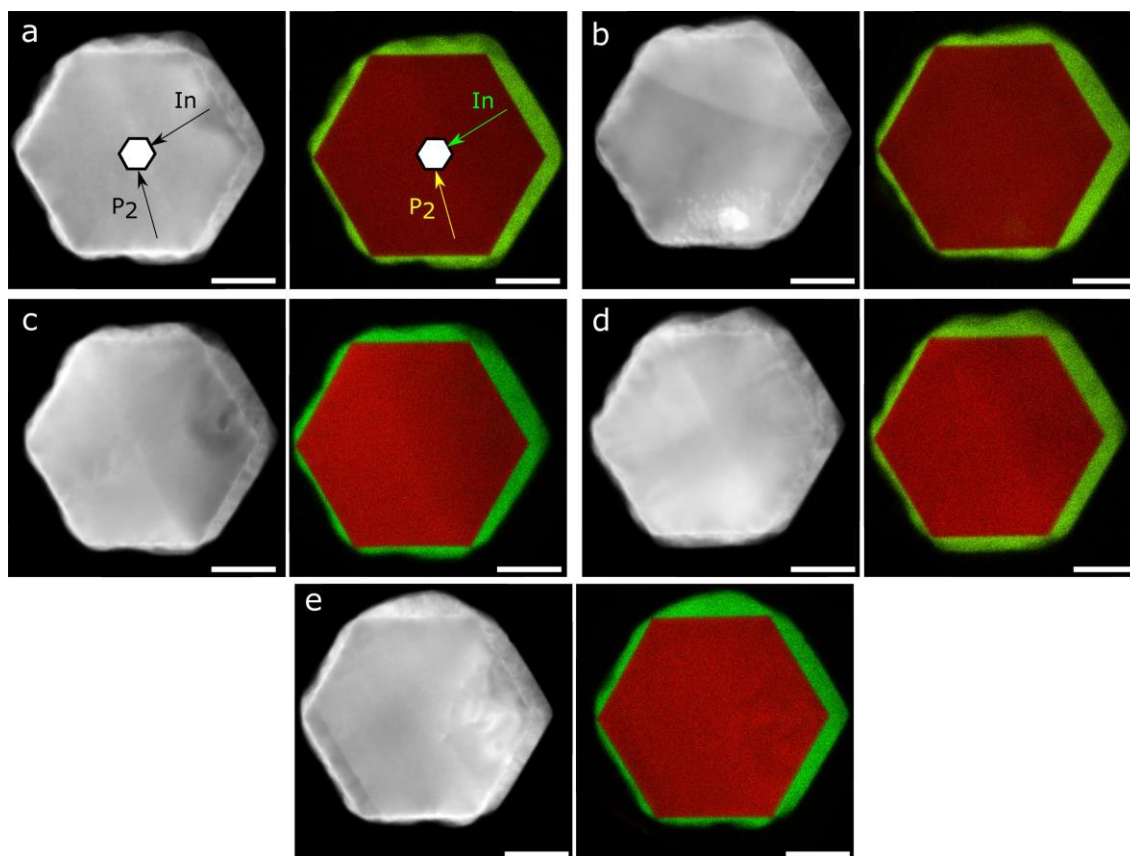


**Figure S4(a–e).** HAADF TEM and EDS maps of nanowire microtome cross-sections for nanowires with shells grown at 210 °C. The arrows and labels in (a) indicate the flux directions of P<sub>2</sub> and In for all panels. All scale bars are 50 nm.

Figure S5 presents a HAADF TEM micrograph and EDS map for an additional shadowed nanowire with shell grown at 380 °C. As for the nanowires grown at this temperature and shown in the main text, this nanowire exhibits smooth shell surfaces, showing a distributed shell based on the relative amount of P<sub>2</sub> flux received.

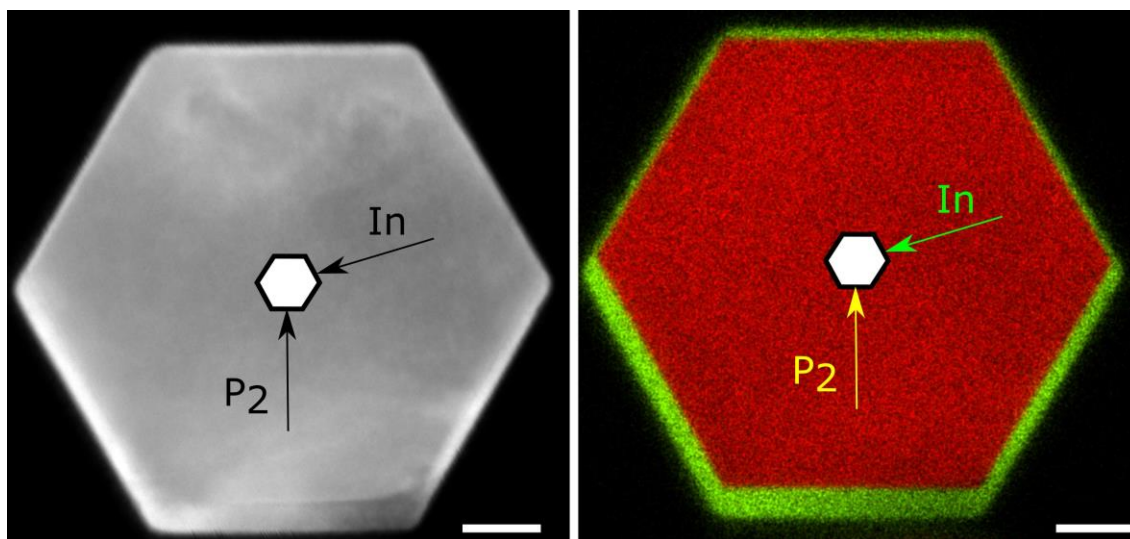


**Figure S5.** Nanowire microtome cross-section HAADF and EDS map for a nanowire with shell grown at 380 °C. The arrows and labels indicate the flux directions of P<sub>2</sub> and In. Scale bars are 20 nm.

## References

- (1) Watanabe, M.; Williams, D. B. The Quantitative Analysis of Thin Specimens: A Review of Progress from the Cliff-Lorimer to the New Z-factor Methods. *Journal of microscopy (Oxford)* 2006, 221 (2), 89–109. <https://doi.org/10.1111/j.1365-2818.2006.01549.x>.
- (2) Watanabe, M.; Horita, Z.; Nemoto, M. Absorption Correction and Thickness Determination Using the  $\zeta$  Factor in Quantitative X-Ray Microanalysis; 1996; Vol. 65. [https://doi.org/10.1016/S0304-3991\(96\)00070-8](https://doi.org/10.1016/S0304-3991(96)00070-8).
- (3) Nishinaga, T.; Shen, X. Q.; Kishimoto, D. Surface Diffusion Length of Cation Incorporation Studied by Microprobe-RHEED/SEM MBE. *J Cryst Growth* 1996, 163 (1–2), 60–66. [https://doi.org/10.1016/0022-0248\(95\)01050-5](https://doi.org/10.1016/0022-0248(95)01050-5).

- (4) Yamashiki, A.; Nishinaga, T. Arsenic Pressure Dependence of Incorporation Diffusion Length on (0 0 1) and (1 1 0) Surfaces and Inter-Surface Diffusion in MBE of GaAs. *J Cryst Growth* 1999, 198, 1125–1129.  
[https://doi.org/10.1016/S0022-0248\(98\)01135-X](https://doi.org/10.1016/S0022-0248(98)01135-X).
- (5) Ogura, T.; Nishinaga, T. Efficiency Difference in Ga Adatom Incorporation in MBE Growth of GaAs with As<sub>2</sub> and As<sub>4</sub> Molecular Beams. *J Cryst Growth* 2000, 211, 416–420. [https://doi.org/10.1016/S0022-0248\(99\)00804-0](https://doi.org/10.1016/S0022-0248(99)00804-0).

## **Supporting Information: Electron Microscopy Study of Core–Shell Nanowire Bending and Twisting**

This supplementary information outlines the analytical tomography techniques that were used to reconstruct cross-sections from energy dispersive spectroscopy (EDS) lines scans taken across a nanowire. As shown in Figure S1, the procedure involves three separate postprocessing steps: core profile reconstruction, shell profile reconstruction, and combining these profiles to create a 2D cross-section reconstruction. An EDS line scan provides spatial and compositional data along the line scan by detecting the intensity of characteristic x-rays from the material. Characteristic x-rays from the K-shell for Gallium and the L-shell for Indium are used in the analysis. The net EDS profiles (background corrected) seen in Figure S1a are generated with Velox software from Thermo Fisher Scientific.

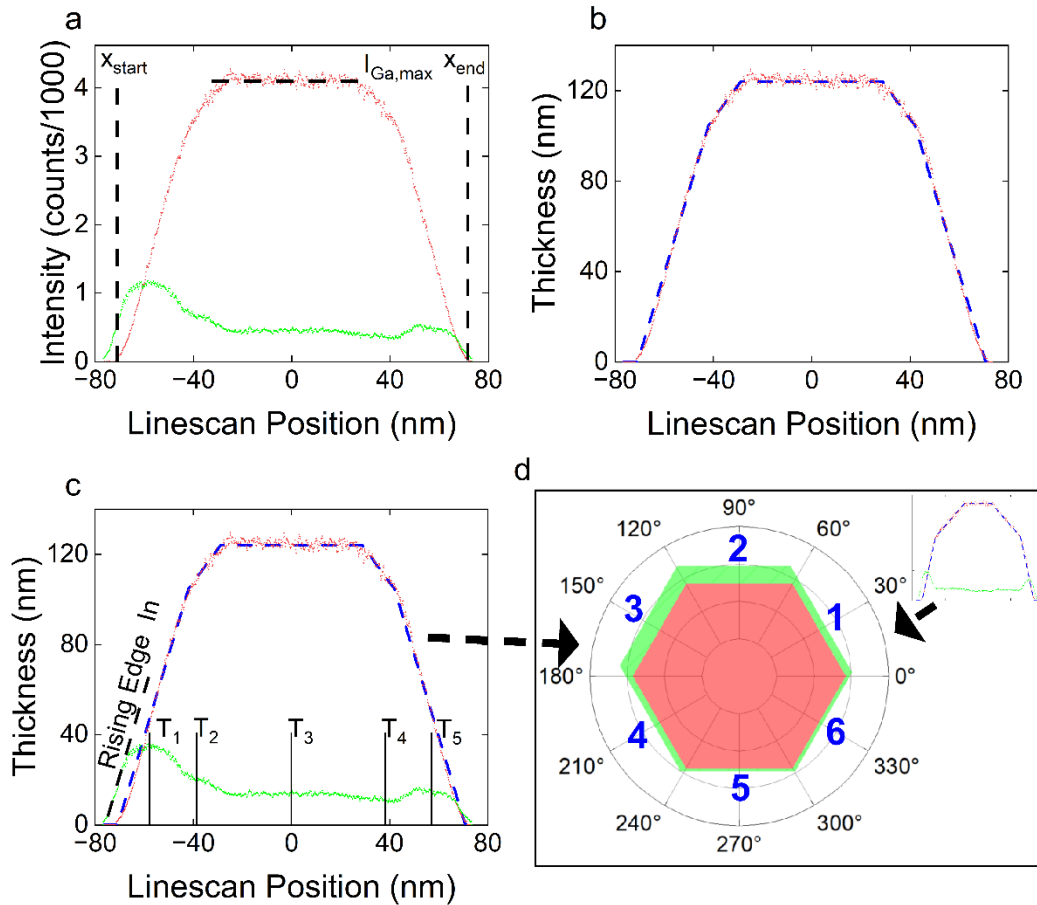


**Figure S1.** Analytical tomographic reconstruction of EDS data from the 3<sup>rd</sup> measurement region (from the nanowire base) in Fig. 3a of the main text. (a) Intensity profiles for Ga (red) and In (green). The max Ga intensity is labelled along with the start and end positions of the GaAs core. (b) Reconstructed core profile (blue dashed line) and the overlaid intensity profile (red points) scaled proportional to thickness. (c) Core and shell thickness profiles, where the rising-edge of the InP shell is marked with a dashed line and T<sub>1-5</sub> correspond to center points between thickness inflection points of the shell (related to the shell's hexagonal geometry). (d) Extracted core-shell cross section showing the GaAs core (red area) and the InP shell (green area). The inset shows the thickness profiles extracted from the same section for the second tilted scan. The purpose of the inset and black arrows are to illustrate that two scans are used to reconstruct the 2D cross-section. The side facets in (d) are labelled 1 to 6. The radial lines in all panels are spaced by 25 nm.

Several parameters influence the EDS intensity, including the characteristic x-rays measured. However, for a thin specimen of uniform composition, the signal intensity

should be directly proportional to thickness (See  $\zeta$ -factor method)<sup>1,2</sup>. Using this relationship, the intensity data can be correlated with the spatial data obtained from a line scan, provided the underlying geometry is known. For the core cross-section, hexagonal width profiles are used to match Ga EDS profiles, considering the core's angular orientation and major radius as parameters. All profiles and hexagonal reconstructions are centered about the origin. Equation S1,  $T_{core}(x, R, \theta)$ , is the generated thickness profile of the core along the scan axis ( $x$ ), created from function  $y_{Hex}(x, R, \theta)$ —a hexagon perimeter in Cartesian coordinates plotted along the scan direction ( $x$ ) with two other parameters: major radius ( $R$ ) and hexagon angular orientation ( $\theta$ ). Angular orientation is relative to the scan direction and is defined as zero for a line scan in the  $\langle 11\bar{2} \rangle$  direction.  $y_{Hex}(x, R, \theta)$ , can be made into a thickness profile by taking the difference in perimeter values along  $x$ :

$$T_{core}(x, R, \theta) = y \in \mathbb{R}^{\geq} [y_{Hex}(x, R, \theta)] - y \in \mathbb{R}^{\leq} [y_{Hex}(x, R, \theta)]. \quad (S1)$$

We align the thickness profile with the EDS intensity profile by adjusting the radius and orientation ( $\theta$ ) so that the distance between the start and end points of the intensity profile, defined by a scan intensity of 0.5% of the maximum intensity (see Figure S1a), corresponds to the start and end of the core. The length of the core measured from the EDS line scan ( $L_{scan}$ ) is,

$$L_{scan} = x_{end} - x_{start}. \quad (S2)$$

To align the thickness profile, it is projected on the  $x$  axis (scan axis), and if it is equivalent to,

$$L_{scan} = proj_x[T_{core}(x, R, \theta)], \quad (S3)$$

then,

$$T_{core,fit}(x, \theta) = T_{core}(x, R, \theta) \quad (S4)$$

$T_{core,fit}(x, \theta)$  is the adjusted thickness profile fit to the EDS line scan length (independent from radius).

The intensity profile  $I_{Ga}(x)$  is related to the thickness of the nanowire cross-section by overlaying  $T_{core,fit}(x, \theta)$  and the scaled intensity profiles, so the maximum intensity ( $I_{Ga,max}$ ) is equivalent to the maximum thickness of the generated profile  $T_{core,max}(\theta)$  (as seen in Figure S1b). In doing so, the orientation of the nanowire  $\theta$  and the thickness profile can be fit to the EDS data.  $I_{Ga,max}$ , found by averaging a 6-nanometer length around  $x = 0$ .

$$T_{Ga}(x, \theta) = \frac{T_{core,max}(\theta)}{I_{Ga,max}} I_{Ga}(x) \quad (S5)$$

The  $\theta$  parameter is determined by finding the coefficient of determination between the generated thickness profile and the scaled EDS line scan numerically for different angles  $\theta$ .

$$R^2(\theta) = 1 - \frac{\sqrt{\sum(T_{Ga}(x, \theta) - T_{core,fit}(x, \theta))^2}}{\sum(T_{Ga}(x, \theta) - \bar{T}_{Ga}(\theta))^2} \quad (S6)$$

The orientation  $\theta$  with the highest coefficient of determination was chosen as the thickness profile of the nanowire,  $T_{Ga}(x)$ .

Assuming the cross-section crystallographic facets are consistent with those observed in McDermott et al.,<sup>3</sup> the core and shell both have facets terminated on  $\{1\bar{1}0\}$  planes, like the core. Therefore, the slope of the rising edge of the core and shell thickness profiles will be equivalent. The following relationship can be defined for the rising edge,

$$\frac{\partial}{\partial x} T_{Ga,riseEdge}(x) = \frac{\partial}{\partial x} T_{In,riseEdge}(x) \quad (S7)$$

First, to solve the relationship between L-shell intensity and shell thickness the slope of the rising edge of the shell intensity profile ( $\frac{\partial}{\partial x} I_{In,riseEdge}$ ) is found by performing linear regression on the rising edge of the shell EDS data,

$$\left[ \begin{array}{c} y_{int} \\ \frac{\partial}{\partial x} I_{In,riseEdge} \end{array} \right] = ([x]^T [x])^{-1} [x]^T [I_{In}(x)] \quad (S8)$$

The slope of the rising edge for the core thickness profile is fit the same way. For both fits, the first and last nanometer are excluded from the rising edge as the spot size of the

STEM probe is approximately 1 nm, and this would remove distortions at the start and the end of the scan.

The shell profile correlates with thickness through a factor  $\alpha$  determined by relating the slopes from the intensity of the shell to the thickness of the core,

$$\frac{\partial}{\partial x} T_{Ga, riseEdge} = \alpha \frac{\partial}{\partial x} I_{In, riseEdge} \quad (S9)$$

Substituting Eq. S7 into S9 gives,

$$\frac{\partial}{\partial x} T_{In, riseEdge} = \alpha \frac{\partial}{\partial x} I_{In, riseEdge} \quad (S10)$$

where  $\alpha$  is a factor that can scale the intensity profile to give a shell thickness profile along the scan length (figure S1c),

$$T_{In}(x) = \alpha I_{In} \quad (S11)$$

A model of the asymmetric shell is constructed from the shell thickness profile with three main assumptions: 1) the shell grows around the nanowire core, 2) the compositions of the GaAs and InP shell are pure, and 3) the  $\{1\bar{1}0\}$  terminating facets intersect where they connect to enclose the shell. This gives the following equations relating side facet thickness to the shell thickness profile for the five regions as indicated in figure S1c,

$$F_4 = \left( T_1 - \frac{F_3}{\sin(30^\circ - \theta)} \right) \cdot \sin(30^\circ + \theta) \quad (\text{S12})$$

$$F_2 = \left( T_2 - \frac{F_4}{\sin(30^\circ + \theta)} \right) \cdot \cos(\theta) \quad (\text{S13})$$

$$F_5 = \left( T_3 - \frac{F_2}{\cos(\theta)} \right) \cdot \cos(\theta) \quad (\text{S14})$$

$$F_1 = \left( T_4 - \frac{F_5}{\cos(\theta)} \right) \cdot \sin(30^\circ + \theta) \quad (\text{S15})$$

$$F_6 = \left( T_5 - \frac{F_1}{\sin(30^\circ + \theta)} \right) \cdot \sin(30^\circ - \theta) \quad (\text{S16})$$

$T_1$ - $T_5$  are five thicknesses along  $T_{In}(x)$  corresponding to inflection points based on the shell faceting marked in Figure S1c.  $F_1$ - $F_6$  are the thicknesses of the side facets along the  $\langle 1\bar{1}0 \rangle$  direction, and the numbering corresponds to the facet numbering seen in Figure S1d. However, these equations are self-referential, and with six side facets, the solution is undefined—resulting in multiple, unbounded solutions in the direction of the line scan. To address this, it is necessary to project this unbounded thickness profile onto a second thickness profile to generate a bounded two-dimensional cross-section (illustrated in Figure S1d). In this work, the unbounded shell thickness profiles are projected onto their counterpart shell profile obtained from a second EDS scan at the same location but at a different angle at  $23 \pm 4^\circ$ , theta. The best-fit solution satisfying Eq. S12-16—determined by the projection with the highest coefficient of determination—corresponds to the two-dimensional shell cross-section of the nanowire. This analytical

tomography method enables the creation of two-dimensional shell reconstructions from only two scans.

### References

- (1) Watanabe, M.; Williams, D. B. The Quantitative Analysis of Thin Specimens: A Review of Progress from the Cliff-Lorimer to the New Z-factor Methods. *Journal of microscopy (Oxford)* 2006, 221 (2), 89–109. <https://doi.org/10.1111/j.1365-2818.2006.01549.x>.
- (2) Watanabe, M.; Horita, Z.; Nemoto, M. Absorption Correction and Thickness Determination Using the  $\zeta$  Factor in Quantitative X-Ray Microanalysis; 1996; Vol. 65. [https://doi.org/10.1016/S0304-3991\(96\)00070-8](https://doi.org/10.1016/S0304-3991(96)00070-8).
- (3) McDermott, S.; Smith, T. R.; LaPierre, R. R.; Lewis, R. B. Phosphorus-Controlled Nanoepitaxy of Asymmetric GaAs-InP Core-Shell Bent Nanowires: Implications for Bottom-Up Nanowire Transistors and Sensors. *ACS Appl Nano Mater* 2024, 7 (1), 1257–1264. <https://doi.org/10.1021/acsanm.3c05235>.